universität wien

MASTERARBEIT | MASTER'S THESIS

Titel | Title

Time-dependent study of light-induced hapticity changes in [RuCpBz]+ using theoretical techniques

verfasst von | submitted by

Vera Brieskorn BSc

angestrebter akademischer Grad | in partial fulfilment of the requirements for the degree of

Master of Science (MSc)

Wien | Vienna, 2024

Studienkennzahl lt. Studienblatt | Degree programme code as it appears on the student record sheet:	UA 066 862
Studienrichtung lt. Studienblatt | Degree programme as it appears on the student record sheet:	Masterstudium Chemie
Betreut von | Supervisor:	Univ.-Prof. Dr. Dr. h.c. Leticia Gonzalez Herrero

Abstract

Die vorliegende Arbeit wurde mit dem Ziel verfasst, Haptizitätsänderungen im potentiell katalytisch relevanten metallorganischen Übergangsmetallkomplex $[RuCpBz]^+$, zur besseren Übersichtlichkeit als *Ruwich* bezeichnet, durch eine eindeutige Definition der Haptizität zu detektieren, und darüber hinaus eventuelle Muster im Vollzug solcher Änderungen zu erkennen. Hierbei ist das Interesse in den Ruwich Komplex und die Fluktuation der Bz Haptizität, welche im angeregten Zustand zu beobachten ist, darin begründet, dass dieses Molekül katalytische Anwendungen aufweist, da durch eine kontrollierte Verringerung des Bz Bindungsmodusses neue Liganden an das Rutheniumatom koordinieren können, wodurch die Reaktivität des gesamten Komplexes modifiziert werden kann.

Um im ersten Schritt eine konkretere Definition des Begriffes Haptizität zu etablieren, welche lediglich auf Atompositionen basiert, da letztere in jedem Fall mit einem Experiment in Verbindung bringbar sind, war es ein Anliegen nicht ausschließlich Distanzen zwischen Atomen mit einzubeziehen, sondern die Position des koordinierenden Rutheniumatoms bezüglich des Bz Liganden zu verwenden, um eine Verfälschung des Haptizitätswerts durch Variation im Ligand-Ruthenium Abstand zu vermeiden. Auf Grundlage dieser Positionen von Ruthenium relativ zum Bz Liganden, welche mathematisch durch Projektion von atomverbindenden Vektoren erhalten werden können, wurde ein Ansatz etabliert, welcher die Projektionen für jede denkbare Ruwich Struktur eindeutig mit einem Haptizitätswert verknüpft. Der entwickelte Ansatz, welcher auf einer einfachen mathematischen Funktion basiert, wurde mit weiteren Geometriedeskriptoren verknüpft, welche zusätzliche Einblicke in Änderungen der Ruwichstruktur, unter anderem im Hinblick auf das Öffnen einer neuen Bindungsstelle, gewähren.

Die so entwickelten Geometrieparameter, $\dot{\alpha}$ für Haptizität, δ für Metall-Ligand Distanzen und κ, ein winkelbasiertes Maß, die Anordnung von Bz, Ruthenium, und Cp beschreibend, wurden in zahlreichen quantenchemischen Rechnungen am Ruwich System auf die Probe gestellt. Zu diesem Zweck wurden, nachdem eine adäquate Elektronenstrukturmethode gefunden war, punktuelle Rechnungen für einzelne Ruwichkonfigurationen von Relevanz, sowie dynamische Rechnungen, welche Haptizitätsänderungen in einem zeitabhängigen Rahmen beleuchten, durchgeführt. Da die Haptizitätsänderungsprozesse in Ruwich durch ein Versetzen des Komplexes in den angeregten Zustand induziert werden, war es von Nöten in allen Rechnungen elektronisch angeregte Zustände zu inkludieren, was vor allem in den Dynamiksimulationen den Einsatz von nichtadiabatischen Methoden zur Beschreibung von Kopplungen zwischen elektronischen Zuständen mit energetischer Nähe erforderte. Als solche Methoden wurden ab initio Vervielfältigung (*ab initio multiple spawning* - AIMS) und ab initio Vervielfältigung mit informiert stochastischen Selektionsprozessen (*ab initio multiple spawning with informed stochastic selections* - AIMSWISS) eingesetzt, und deren Resultate mit den Ergebnissen adiabatischer Simulationen im angeregten Zustand verglichen, um das Wirkungsausmaß von nichtadiabatischen Interaktionen auf Haptizitätsänderungen zu evaluieren.

Um ein abschließendes Wort bezüglich der in dieser Thesis ins Auge gefassten Ziele sowie erreichten Resultate zu äußern, lässt sich sagen, dass eine Haptizitätsdefinition entwickelt wurde, welche es erlaubt Haptizitätsänderungen im statischen und im dynamischen Fall aus lediglich den Atomkoordinaten zu extrahieren ohne distanzbasierte Annahmen einbeziehen zu müssen.

Abstract

The work in this thesis was carried out with the aim of detecting light-induced hapticity changes in the transition metal complex $[RuCpBz]^+$, referred to as Ruwich, based on a rigorous hapticity definition. To this end, a hapticity definition that only relies on atom distances, and is therefore connectable to an experiment, was developed. The Ruwich complex is known to undergo changes in hapticity after light excitation due to a destabilization of the Ru-Bz bond in the electronic excited state. This hapticity fluctuation could be exploited catalytically by developing a catalyst where light-induced changes in the binding mode lead to the coordination of a new ligand. By controlling the coordination in a complex such as Ruwich one could switch between different reactivities of the complex and open up several reaction pathways.

As a first step, we dedicated our efforts to the development of a new hapticity definition that does not only rely on Ru-C atom distances but instead takes into account the position of Ru below the Bz ring. We projected the Ru position onto a basis of three bisection vectors representing the Bz hexagon to obtain position-based information on Ru with respect to the Bz ligand. Based on this approach, we developed a procedure that unambiguously yields one Bz hapticity value for each Ruwich structure. Alongside the hapticity parameter, other geometry descriptors were established for Ruwich. These descriptors yield additional information on the Ru-Bz distance and the angle formed by Ru and the Bz and Cp ligands. When taking all parameters together, detailed information is obtained on the structure of Ruwich with a focus on the geometrical relation of Ru and Bz.

The geometry parameters developed for Ruwich, $\dot{\alpha}$ for hapticity, δ for metal-ligand distances, and κ for the Cp-Ru-Bz angle, were tested in static and time-dependent quantum mechanical calculations. In all calculations, excited states were included as the hapticity changes in Ruwich are known to be caused by photo-excitation. In this work, we only considered singlet excitations and did not investigate the influence of triplet states, which would have added another layer of complexity. The static calculations included scans between different Ruwich minimum structures and Ruwich structures of different hapticity. Time-dependent dynamics simulations were carried out using adiabatic simulation techniques and the nonadiabatic methods ab initio multiple spawning (AIMS) and ab initio multiple spawning with informed stochastic selections (AIMSWISS). In this way, we could obtain an estimate of the importance of nonadiabatic effects on the hapticity changes in Ruwich. As the Ruwich complex has many energetically close electronic states the computationally demanding AIMS approach could only be applied in a short time interval. We therefore saw the opportunity to test the AIMSWISS approach, which applies an additional approximation to AIMS, on the Ruwich complex and obtained a simulation covering a longer time frame.

In the course of this thesis, we established a hapticity definition that is able to capture hapticity changes in static and dynamic settings. Including only simple relations between atom distances, this definition is straightforward and can easily be extended to account for other cyclic ligands than Bz in the form of different polygons.

Abbreviations

Ruwich [RuCpBz]$^+$

Bz benzene

Cp cyclopentadienyl

COT cycloocatetraene

TDSE time-dependent Schroedinger equation

TISE time-independent Schroedinger equation

BH Born-Huang

DFT density functional theory

TDDFT time-dependent DFT

ALDA adiabatic local density approximation

LR-TDDFT linear-response TDDFT

PES potential energy surface

LIIC linear interpolation in internal coordinates

BO Born-Oppenheimer

TBF trajectory basis function

vMCG variational multi-configuration gaussian

FMS full multiple spawning

AIMS ab initio multiple spawning

DBOC diagonal Born-Oppenheimer corrections

SPA0 saddle point approximation

IFGA independent first generation approximation

AIMSWISS ab initio multiple spawning with informed stochastic selections

FC Franck-Condon

AIMD ab initio molecular dynamics

Contents

The motto of such a molecule, if it spoke French, might well be *Plus que je change, plus que je suis la même chose*.

- F. A. Cotton[1]

Plus que je change, plus que je suis la même chose.

- Gossip Girl[2]

1 Introduction

1.1 Application of organometallic complexes in photo-catalysis

Molecules formed out of a central transition metal atom coordinated to organic ligands, so-called organometallic complexes, are often investigated as promising candidates for homogenous catalytic reactions.[3][4][5] Organometallic complexes show a vast variety in the tuning of binding preferences, as the ligand composition can be changed to alter the electronic and steric character of the metal centre. Tuning the metal centre's binding preferences allows one to change the character of the catalyzed reaction because substrate coordination and conversion are modified. Hereby, the electronic and steric properties of the catalyst can often be adjusted separately, allowing for additional tuning flexibility. Commonly employed ligands that exemplify the separate tunability include N-heterocyclic carbenes[6][7] and pincer ligands[8]. Among other types of ligands, these are successfully applied in the catalysis of alkene metathesis and C-C, as well as C-hetero atom cross-coupling reactions.

Apart from the exhaustive tailoring possibilities, organometallic complexes furthermore provide easily accessible photo-excitation pathways. These convenient photochemical properties are obtained due to the mixing of metal and ligand orbitals which changes the character of the otherwise pure d-orbitals in the metal. This change in character makes the energetically easily accessible d-transitions in organometallic complexes gain a substantial amount of intensity. The excited organometallic molecule either allows for direct exploitation when designing photo-catalytic reaction cycles or can be employed to excite smaller organic molecules controllably. After excitation, organic substrates often follow synthetic routes unparalleled in ground state chemistry and sometimes even gain access to opposing reactivities[9]. These significant changes take place because excited molecules can undergo significant structural changes while the shape of occupied orbitals can also show large variations[10]. The general tuning flexibility of ground-state organometallic complexes, combined with their beneficial photo-chemical properties, offers a vast area of reactive pathways to explore, that opened the field of photo-catalysis.

Alongside the experimental processes involved in the discovery and improvement of photo-catalytic reactions[11], accompanying computational studies can provide supplementary insight into the underlying mechanisms.[12][13] Computational approaches can deliver more in-depth information on processes at an atomic scale while being connected to real-life experiments via measurable observables. To state an example of a computational approach clarifying photo-catalytic processes, one should name the simulation of nuclear dynamics on several electronic excitation levels. Such a simulation can give an idea of the movement and characteristic properties of a potential catalyst after exposure to a light source.

Despite the advantages computational approaches provide, one should note that organometallic complexes are often complicated candidates in the simulation of excited state dynamics as they usually have energetically close low-lying excited states. This manifold of photo-accessible electronic states causes the need to include a high number of states in a photo-dynamics simulation. Therefore, the computational cost increases when dealing with organometallic complexes, which might evoke the need for further approximations. Nevertheless, the information obtained from a computational study, which is often cru-

cial for improving photocatalytic cycles[14], justifies the effort of carrying out excited-state nuclear dynamics simulations on these systems.

1.2 Complexes containing flexibly coordinating cyclic π ligands

A common class of ligands in organometallic chemistry consists of cyclic π systems coordinating to the central metal atom via donation of π electrons. Due to the transition metal's specific need for electrons, a cyclic π ligand might not contribute all available π electrons to the metal-ligand interaction.[15] The concept of *hapticity* was introduced during the 1960's[16] to account for the different bonding modes a cyclic π ligand can adopt. By stating the hapticity of a complex, one refers to the number of coordinative bonds formed between the metal and a particular ligand. The concept of *hapticity* additionally provides a nomenclature, used until this day, to describe the differences in coordination numbers.[15] To state a common example, a cyclopentadienyl ligand with all five carbon atoms coordinated to the central metal atom is termed η^5, where the Greek letter η is the symbol of hapticity. At a later point, the meaning and role of the term *hapticity* will be discussed in more detail.

It was already known when the term hapticity was originally coined that changes in hapticity can be undergone by a molecule over time. On the one hand, the hapticity of a ligand can change as a result of a chemical reaction where the electronic need of the central metal atom changes. In addition, the entering of a new ligand or the leaving of a ligand can reduce or increase the hapticity of another, flexibly coordinating ligand.[17] On the other hand, hapticity changes can be caused by a fluctuation where the overall hapticity value remains constant while variation occurs in the ligand positions, that are coordinated to the metal.[18][19]

To state an example of hapticity change induced by ligand fluctuation the slip distortion[20] shall be mentioned. Slip distortions are likely to occur when a metal complex exceeds the 18 e^- rule and the additional electron occupies an anti-bonding orbital leading to a destabilization of the metal-ligand bond. The ligand then reduces its hapticity either by bending or by laterally 'slipping' away from the central metal atom. Slip distortions are also relevant when an 18 e^- metal complex is excited because the excitation likely targets an anti-bonding orbital producing a binding mode comparable to 19 e^- complexes.

A different type of hapticity change already known to Cotton[18] consists of a ligand rearrangement where the start and end structures do not show different connectivities or differences in energy. These changes typically occur with symmetric ligands that offer the possibility for several equivalent coordination geometries. This type of hapticity change was referred to by Cotton as fluxonial behavior and in later days known as haptotropic rearrangement[21]. Several examples show that fluctuations in hapticity for an organometallic complex either take place in the ground state due to thermal activation or in the excited state where the process is photo-activated.[22][23]

One experimental technique to observe fluxonial behavior is to study peak broadening in NMR spectra recorded at different temperatures. Reducing the thermal energy slows down the hapticity rearrangement process, which becomes visible in the NMR spectrum as peaks become separated when the temperature is decreased. This separation occurs because the corresponding nuclei are no longer part of the same chemical environment when the rearrangement process slows down. However, when following the NMR approach to

detect fluxonial behavior, one often encounters difficulties in determining the mechanism of the rearrangement. A typical example of a rearrangement process study using NMR is presented in references [15] and [24] where a η^1 coordinated Cp ligand changes the C position coordinated to the metal atom. Here, five equivalent coordination positions are available to the metal. The H nuclei connected to the Cp C atoms show equivalent NMR signals at room temperature. When lowering the temperature, these NMR peaks first get broadened and then fully separate. As the metal atom migrates with reduced speed from C atom to C atom, the change in the chemical environment of the H nuclei becomes measurable at an NMR time scale. In the presented case, the discovery of fluxonial behavior was relatively easy compared to the later required effort to find the mechanism underlying the process.[25]

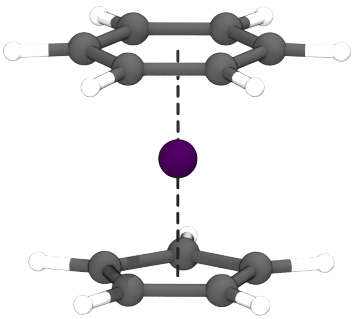

[RuCpBz]$^+$
referred to as Ruwich

Figure 1: The sandwich complex [RuCpBz]$^+$ referred to as Ruwich throughout this thesis. Coordinative bonding between the Bz, and Cp cyclic π ligands and the Ru atom is indicated by dashed lines.

Although experimental and computational studies on haptotropic rearrangements exist for organometallic complexes, as presented above, investigating the time-dependent hapticity change is not often the centre of interest. The assumption that fluxonial behavior might not alter the reactivity of a complex and the difficulty in determining the rearrangement mechanisms could be held responsible for this circumstance. To familiarize the reader with the computational study of light-induced hapticity change carried out in this thesis the investigated molecule, [RuCpBz]$^+$, shall be introduced. [RuCpBz]$^+$, an organometallic sandwich complex, shall from now on be referred to as *Ruwich*, a term used because Ru as the central transition metal atom is sandwiched between a Cp and a Bz ligand. An overview of the ground state structure of Ruwich is provided in figure 1.

The Ru-Bz bonds in Ruwich are substantially weakened when the molecule is electronically excited because a molecular orbital anti-bonding towards Ru and Bz becomes occupied.[26][27] An excitation of Ruwich thus causes a binding mode similar to complexes with 19 electrons where slip distortions result in a lowering of hapticity. With the Ru-Bz bond destabilized, another suitable ligand can substitute Bz, allowing Ruwich to undergo a variety of photoinduced replacement reactions, as presented in figure 2. Figure 2 shows that the Ruwich complex can controllably undergo replacement reactions and

therefore has huge potential for application in organometallic photocatalysis.

Figure 2 pictures the hapticity reduction in Ruwich from η^6 to η^4 to happen because the Bz ring is bent. In addition, this picture suggests that the hapticity is only reduced when a new ligand is coordinated to Ru. However, a bend in the ring structure simultaneous to a new ligand entering is only one possible mechanism for lowering the hapticity. Another possibility is the aforementioned slip distortion that has a less obvious effect on the Bz ring structure. Furthermore, hapticity changes can be caused by an excitation and do not necessarily require the coordination of a new ligand. The photo-induced haptotropic rearrangements of Ruwich will be studied to distinguish between the more conventional picture of hapticity change occurring because of a ring bend, and hapticity change caused by a slip distortion.

Regarding the mechanistic investigation of light-induced haptotropic rearrangements, as occurring in Ruwich, computational studies are a useful tool as they allow for the observation of atomic movement. However, to learn more about hapticity rearrangement mechanisms in Ruwich, one must be able to extract the appropriate information from the performed simulations. Defining and detecting hapticity changes in Ruwich is complicated by the circumstance that first of all, no general definition of the term *hapticity* is provided, and secondly, no strategy to unambiguously determine hapticity values is available. Up until this point, computational studies have usually relied upon bond distances for detecting hapticity, which requires the application of a threshold. As bond distance thresholds are often difficult to base on a rationale, it would prove useful to find a proper definition that applies to a variety of systems.

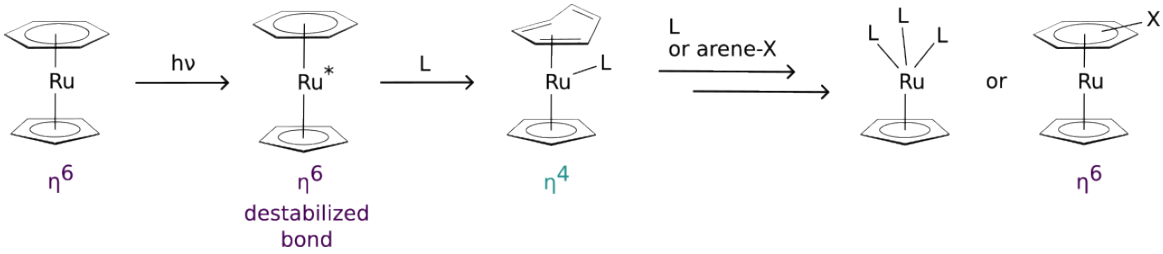

Figure 2: A photoactivated replacement reaction undergone by the Ruwich complex. The Ru-Bz bond is first destabilized, leading to an η^4 coordination and entering of a new ligand. Bz is then fully replaced with a different arena (arene-X) or another suitable ligand in solution (L). This figure is adapted from reference [28].

Apart from the investigation of Ruwich, obtaining a better understanding of light-induced hapticity changes could prove useful for catalytic applications. A possible application would be an organometallic complex that controllably opens a new coordination site because one ligand reduces its hapticity when the complex is irradiated with light. Furthermore, a simulation-based study of fluxonial behavior is beneficial on a conceptual level due to the need to properly define a measure for hapticity. Owed to these benefits, this thesis focuses on the simulation, and definition-based detection, of hapticity changes in the Ruwich complex. Hereby, the ultimate goal lies in providing a more time-dependent picture of the concept behind *hapticity* applicable to a vast variety of sandwich compounds.

1.3 In search of criteria defining hapticity

The original definition of the term *hapticity* established by Cotton in 1968 is held rather vague with the objective to, as Cotton states, *avoid implications and, hence, subjective judgments about bonding details*[16]. He states that hapticity *simply gives a topological description*[16]. Cotton derived the prefix *hapto* used to denote the hapticity of a ligand from the greek ἁπτειν, the present active infinitive form of ἁπτο, which translates as *to fasten, denoting contact or combination*[16]. Cotton first chose the letter *h* as a symbol for *hapto* and later replaced it with the Greek letter η. This letter was chosen, although η functions as a vowel in most ancient Greek dialects and not as a consonant resembling the sound of the Latin letter *h* used today.

As stated above, it was already known in the days when Cotton presented his concept, that certain molecules undergo changes in hapticity. Due to the vagueness of defining *hapticity* it can, especially in situations of frequent hapticity changes, be difficult and ambiguous to assign an η value to a molecular geometry of question. In existing studies of hapticity change, the η value is usually determined based on the distances between the central metal atom and the potentially coordinating atoms in the ligand. The required structural data is usually taken from X-ray structures or computational results.

Most computational studies on haptotropic rearrangements consist of static calculations including e.g. scans in search for stationary points between two structures of different hapticity. In these studies, the geometric criteria used to assign an η value to a particular structure rarely go beyond the evaluation of metal-ligand atom distances. As an example of employing atom distance measures, the works by Doetz[29], Ketrat[30], and Gridnev[31] can be mentioned. In the latter study by Gridnev on rearrangement processes in a cycloocatetraene (COT) osmium complex, an additional geometric criterion is employed. This criterion involves the tub angle of COT describing whether the ligand is in a tub configuration (ground state) or in a planar position (excited state). Although a high tub angle indicates a η_4 coordination this finding cannot be attributed to one single conformation of the complex, as the Os atom can coordinate to the tub-shaped COT from different sides. Using the tub angle as an additional geometric measure does thus not establish a unique connection between hapticity and molecular structure.

Another geometric criterion going beyond the use of atom distances is employed in computational studies on the indenyl ligand. This ligand, a junction of a five- and a six-membered ring, can flexibly adapt to the metal atom's electronic needs by providing a number of C atoms for coordination ranging from two to a maximum of nine. The indenyl ligand therefore shows different hapticity values depending on the electronic need of the central metal atom. In a study of Zr sandwich complexes with two indenyl ligands, Bradley[32] and Veiros[33] used angles between ring centroids and planes defined by individual rings to find a connection between changes in hapticity and overall complex geometry. Bradley et. al. used an angle defined by the indenyl five-ring centroid, the six-ring centroid, and the Zr atom to quantitatively determine the likelihood of opening a new coordination site. A similar measure will at a later point be discussed for Ruwich.

In combination with geometric criteria to determine the hapticity of a cyclic ligand, computational studies often apply criteria based on electronic structure quantities. These only theoretically accessible quantities give information on the bond character or the bond population between the metal and ligand atoms. An example of this approach can be found

in the works of Gloriozov et. al.[34, 35, 36] In these studies, an energy decomposition approach for the interaction energy between two fragments of the complex is used alongside atom distances. The decomposition approach relies on splitting the complex into two fragments, defined as the metal and the ligand under consideration, to quantify the metal-ligand interaction.[36] In their 2019 study, Gloriozov et al. focus on the haptotropic rearrangement of a $[RuCp]^+$ moiety coordinated to a polycyclic aromatic ligand that is composed of a varying number of Bz units. Hereby, the energy decomposition analysis is carried out between the $[RuCp]^+$ fragment and the polycyclic unit. Another approach by Gloriozov et. al., applied in the study of tricarbonylchromium complexes with an amino-substituted diphenyl ligand analyses the electron density distribution at certain parts of the complex to clarify whether the N atom assists in the rearrangement process.[35] The advantage of this approach over the fragment-based approach lies in the metric being based on the electron density. This quantity is in principle experimentally accessible whereas properties obtained from artificial fragments cannot be connected to an experiment.

Concerning already existing measures for hapticity in computational studies, it can be stated that the geometric criteria applied often consist of simple atom distances, or, if more complicated, involve rather arbitrary quantities that can only apply to the structure they were created for. Moreover, the geometric criteria often rely on the ligand ring remaining planar or varying between two well-defined extrema. This constraint facilitates the application of geometric criteria of any sort, allowing them to rely on angles formed between ligand planes. Relating different planes to each other is a handy approach as the orientation of several atom groups can be assessed within one criterion. However, such a criterion can only be applied if the required planes are not deformed during the studied process. In available computational studies, the ring geometry undergoes so little variation because no electronic excitations and thus occupations of antibonding orbitals are considered. Instead, ground state rearrangements are analyzed, which are only rarely caused by significant changes in ligand conformation. The almost inevitably occurring ring distortions must be accounted for to study hapticity changes caused by photo-excitation. However, with the conformation of the ring ligand showing fluctuation and the ring structure giving up its planarity, identifying a geometric criterion is far more complicated. For the Ruwich complex, the identification of a universally valid geometry-based hapticity criterion is challenging due to the strong deformations of the Bz ligand after photo-excitation.

1.4 Goals of this thesis

Motivated by the aforementioned lack of a rigorous definition of hapticity, this thesis focussed on two main goals. Firstly, a new definition of hapticity was developed that is equally valid in static and dynamic applications. Hereby, special care was taken to establish a geometry-based criterion connected to an experimentally accessible observable. As a second goal, we wanted to test the hapticity definition on the Ruwich complex in different scenarios ranging from the static picture to adiabatic and nonadiabatic dynamics. In this way, a universally applicable hapticity definition was obtained that can be transferred to other sandwich complexes composed of various cyclic π ligands.

2 Theoretical background

In this chapter, the theoretical background required to understand the computational methods applied in this thesis shall be discussed. Aspects of the presented theory especially relevant for the application at hand, the excited state dynamics of the Ruwich complex, will be discussed with particular emphasis.

2.1 Basic concepts of quantum chemistry

A main goal of theoretical chemistry lies in approximating the solution to the molecular time-dependent Schroedinger equation. To this end, approaches with varying accuracy depending on the chemical system of interest are available and still subject to development. Hereby, one can search to approximate a solution of the time-dependent Schroedinger equation (TDSE)

$$\hat{H}(\boldsymbol{r},\boldsymbol{R})\Psi(\boldsymbol{r},\boldsymbol{R},t) = i\frac{\partial}{\partial t}\Psi(\boldsymbol{r},\boldsymbol{R},t)\ , \tag{1}$$

where $\hat{H}(\boldsymbol{r},\boldsymbol{R})$ is the Hamiltonian operator containing the kinetic energy and the potential guiding the movement of the system of interest. Equation (1) is expressed in atomic units as this unit system shall be used throughout this thesis. In chemical applications, a molecular system is often studied by determining the molecular wave function $\Psi(\boldsymbol{r},\boldsymbol{R},t)$ via a set of nuclear coordinates $\boldsymbol{R}$ and electronic coordinates $\boldsymbol{r}$. The Hamiltonian

$$\begin{aligned}\hat{H}(\boldsymbol{r},\boldsymbol{R}) &= \hat{T}_n(\boldsymbol{R}) + \hat{T}_e(\boldsymbol{r}) + \hat{V}_{nn}(\boldsymbol{R}) + \hat{V}_{ee}(\boldsymbol{r}) + \hat{V}_{ne}(\boldsymbol{r},\boldsymbol{R}) \\ &= -\sum_I^{N_n}\frac{1}{2M_I}\nabla_I^2 - \sum_i^{N_e}\frac{1}{2}\nabla_i^2 + \sum_{I<J}\frac{Z_I Z_J}{|\boldsymbol{R}_I-\boldsymbol{R}_J|} + \sum_{i<j}\frac{1}{|\boldsymbol{r}_i-\boldsymbol{r}_j|} - \sum_{I,i}\frac{Z_I}{|\boldsymbol{R}_I-\boldsymbol{r}_i|}\end{aligned} \tag{2}$$

contains kinetic ($\hat{T}_n$ and $\hat{T}_e$) contributions and potential contributions arising from the interaction between the N_n nuclei (V_{nn}), the N_e electrons (V_{ee}), and the nuclei and electrons (V_{ne}). One often groups the electronic terms into an electronic Hamiltonian, defined as

$$\hat{H}_{el}(\boldsymbol{r},\boldsymbol{R}) = -\sum_i^{N_e}\frac{1}{2}\nabla_i^2 + \sum_{I<J}\frac{Z_I Z_J}{|\boldsymbol{R}_I-\boldsymbol{R}_J|} + \sum_{i<j}\frac{1}{|\boldsymbol{r}_i-\boldsymbol{r}_j|} - \sum_{I,i}\frac{Z_I}{|\boldsymbol{R}_I-\boldsymbol{r}_i|}\ , \tag{3}$$

where V_{nn} enters only as a constant. Using $\hat{H}_{el}$ for a fixed set of nuclear coordinates yields the time-independent Schroedinger equation (TISE)

$$\hat{H}_{el}(\boldsymbol{r},\boldsymbol{R})\Phi_\nu(\boldsymbol{r};\boldsymbol{R}) = E_{el}^\nu(\boldsymbol{R})\Phi_\nu(\boldsymbol{r};\boldsymbol{R})\ . \tag{4}$$

The TISE is an eigenvalue equation with the electronic wave functions Φ_ν as eigenfunctions. The index ν describes the electronic state the system is in where $\nu = 0$ denotes the ground state of the molecule. The electronic energies E_{el}^ν are the eigenvalues of the corresponding Φ_ν. Both, the eigenfunctions Φ_ν and the eigenvalues E_{el}^ν show parametrical but no explicit dependence on the nuclear coordinates $\boldsymbol{R}$. The eigenfunctions form an infinite dimensional orthonormal basis that can be used to express the molecular wave function $\Psi(\boldsymbol{r},\boldsymbol{R},t)$ once the electronic eigenfunctions are known for every nuclear configuration $\boldsymbol{R}$.

An expansion of Ψ in the basis of Φ_ν gives rise to the Born-Huang (BH) representation, which shall be discussed in chapter 2.5. Splitting the Hamiltonian $\hat{H}$ and the molecular wave function Ψ into a nuclear part and an electron-dependent part gave birth to two major fields in quantum chemistry. The first, electronic structure theory, aims at finding approximate methods for solving the TISE, while the field of nuclear dynamics deals with the propagation of nuclear coordinates in time. Dividing the complicated challenge of solving the TDSE into two smaller problems shaped the classic understanding of chemistry at an atomistic level and facilitated the specialization into separate research branches. But this splitting of the problem easily leads to the downside of seeing the two fields as too far apart although they are highly coupled.

In the following section, electronic structure theory approaches to solving the TISE and dynamics approaches to propagating the nuclear coordinates shall be discussed. The discussion will be governed by the aim of simulating the excited state dynamics of the Ruwich complex.

2.2 Density functional theory (DFT)

In the following, density functional theory (DFT), a different way of expressing the TISE presented in equation (4) that leads to efficient approximations, shall be discussed. To this day, no analytical or numerical solution to the TISE for any system containing more than one electron is known, but different approaches have been developed to approximate a solution. Among these methods, DFT is a prominent candidate because the method relies on the electron density ρ as the central descriptor of the system. Hereby, usage of the high-dimensional and experimentally inaccessible electronic wave function Φ is omitted. Note that in the following, n will be used to signify the number of electrons N_{el} for reasons of clarity.

2.2.1 Proof of concept: The Hohenberg-Kohn theorems

While the electronic wave function $\Phi(\boldsymbol{r};\boldsymbol{R})$ contains all information about a system of n electrons, the fact that Φ consists of 3n spatial variables means that this object is extremely complex. Concerning this fact the idea of using a different approach that involves fewer variables seems preferable. Hereby, one possible strategy consists of integrating over the absolute value squared of the wave function which yields the electron density ρ

$$\rho(\boldsymbol{r}) = n \int \cdots \int |\Phi(\boldsymbol{r}_1, \boldsymbol{r}_2, \ldots, \boldsymbol{r}_n)|^2 d\boldsymbol{r}_2, \ldots, d\boldsymbol{r}_n \; . \tag{5}$$

ρ represents the probability of finding one electron in a defined volume $d\boldsymbol{r}$ while the remaining n-1 electrons occupy any other volume element in space. One advantage of the electron density lies in its dependence on only 3 spatial variables. Therefore, ρ is expressed in the physical space and can more easily be imagined than a property in a 3n dimensional space.[37] Furthermore, the electron density is in principle a measurable quantity. Despite these advantages, assuring that ρ contains the same amount of information as the electronic wave function Φ is an inevitable step before relying on ρ for solving the TISE.

Usually, when approximating the exact wave function of a particular system the Hamiltonian is defined first by using the number of electrons and the position and charge of the

nuclei as parameters determining the physics of the system. The obtained Hamiltonian is then applied to a certain set of trial wave functions. Having this procedure in mind, it would prove to be very convenient if the electron density contained the information needed to set up the Hamiltonian, namely the number of electrons as well as the position and charge of the nuclei. With a deeper regard to the definition of the electron density presented in equation (5) one can deduce that the required information is indeed included. The number of electrons can be obtained by integrating the electron density over the entire space

$$\int_{-\infty}^{\infty} \rho(\boldsymbol{r})\, d\boldsymbol{r} = n. \tag{6}$$

The position of the nuclei is also implied in the electron density as ρ rises to a maximum at the position of an atom core due to attractive potentials. The charge of the nuclei can be obtained by examining the gradient of the electron density in the region of such a maximum. The finding that the electron density contains all necessary ingredients to set up the system's Hamiltonian is referred to as the Bright Wilson observation. Even though the information needed to set up the Hamiltonian can be taken from the electron density, it remains questionable whether ρ shows a unique mapping to the system's Hamiltonian and the ground state wave function. As can be imagined, if the electron density yielded several differing descriptions of the very same system one would arrive at a conceptual problem.[37]

Facing the uncertainty of whether a unique mapping exists between the ground state electron density ρ_0 and the ground state wave function Φ_0 the Hohenberg-Kohn theorems published in 1964[38] come to rescue. The first Hohenberg-Kohn theorem, *The Proof of Existence*, proves that two different Hamiltonians $\hat{H}$ and $\hat{H}'$ differing in their external potential V_{ext} and V'_{ext} term by more than a constant cannot lead to the same electron density. The proof is initiated by assuming one ground state electron density ρ_0 to belong to the two differing Hamiltonians and their differing wave functions Φ_0 and Φ'_0

$$V_{ext} \Rightarrow \hat{H} \Rightarrow \Phi_0 \Rightarrow \rho_0 \Leftarrow \Phi'_0 \Leftarrow \hat{H}' \Leftarrow V'_{ext}\ . \tag{7}$$

Here it should be noted that two different wave functions might mathematically well lead to the same electron density due to the square integration over an absolute value (see equation (5)). The proof proceeds by comparing the energy obtained when applying the Hamiltonian $\hat{H}$ to Φ'_0 and the counterpart energy from applying $\hat{H}'$ to Φ_0. $\langle\Phi'_0|\hat{H}|\Phi'_0\rangle$ must yield an energy higher than E_0 as Φ_0 is the ground state wave function for $\hat{H}$. Equivalently, the energy arising from $\hat{H}'$ and Φ_0 must be higher than E'_0. When comparing both energies the proof arrives at a contradiction. From this contradiction, one can deduce that the mapping presented in equation (7) must be erroneous showing that instead, a one-to-one mapping between the external potential and the ground state electron density ρ_0 must exist. As the external potential guides the Hamiltonian and consequently the wave function and ground state energy, the ground state electron density can be used to determine the system's Hamiltonian without ambiguity

$$\rho_0 \Rightarrow n, Z_N, \boldsymbol{R}_N \Rightarrow \hat{H} \Rightarrow \Phi_0 \Rightarrow E^0_{el}\ . \tag{8}$$

When mathematically phrasing the discovered one-to-one connection, it can be said that the ground state energy is a unique functional of the ground state electron density. This statement immediately suggests that the individual contributions to the ground state energy must also be functionals of the ground state electron density

$$E_0[\rho_0] = T[\rho_0] + E_{ee}[\rho_0] + E_{ne}[\rho_0] \ . \tag{9}$$

The different contributions to the ground state electron density functional can be split into system-dependent and system-independent parts. Hereby, the kinetic energy, as well as the potential caused by the electron-electron repulsion, are system-independent. The potential due to attractions between electrons and nuclei, which is in many applications the only contribution to V_{ext} is system-dependent. The system-independent terms can be condensed in one functional to obtain the Hohenberg-Kohn functional

$$F_{HK}[\rho_0] = T[\rho_0] + E_{ee}[\rho_0]. \tag{10}$$

If an explicit form of the Hohenberg-Kohn functional F_{HK} was known one would be able to solve the TISE exactly for every ground state system. But as no exact expression of $F_{HK}[\rho_0]$ is available until today, approximations must be developed. This task originated an enormous field of research that is until today of great importance.

In summary, it can be stated that the first Hohenberg-Kohn theorem proves the existence of a unique link between the Hamiltonian of a system and its ground state electron density. However, the first theorem does not provide any instructions on how the ground state electron density can be found. The second Hohenberg-Kohn[38] theorem consists of a form of the variational principle adapted to the DFT formalism. The theorem provides a conceptual basis for finding the ground state electron density by stating the following: As the electron density functional delivers the lowest energy if and only if the ground state electron density is used, the energy obtained for any other electron density will be higher. As a consequence, varying the electron density until a minimum in energy is found must lead to the exact ground state electron density. With this approach, the second Hohenberg-Kohn theorem provides a strategy to find the ground state electron density, that was before proven to represent a complete source of information to describe the respective ground state system. However, emphasis should be placed on the variational principle having to face more problems than e.g. in the Hartree-Fock approach. Difficulties arise as in any chemical application, approximations have to be applied to the density functional. Consequently, DFT does not employ the exact form of the Hamiltonian contrary to Hartree-Fock. Therefore, the variational principle ceases to be valid in approximated DFT, which leads to the circumstance that energies lower than the exact energy can be obtained.[37]

2.2.2 Developping a strategy: The Kohn-Sham approach

Although proofs were presented, in the form of the Hohenberg-Kohn theorems, that the electron density can be used to obtain the ground state properties of a system, no method on how to determine the ground state electron density is available. This important question is attended to by the Kohn-Sham approach.[39] The goal of this approach is to obtain the ground state electron density of any given system by setting up a reference system of the same electron density whose properties can be determined more easily. To do so, the

reference system is defined as a system of n particles that perform exchange processes like fermions but do not have any charge. This reference system is described as the determinant of n one-electron wave functions ϕ_i referred to as the Kohn-Sham orbitals. The obtained determinant is then multiplied by a normalization factor yielding the wave function of the reference system

$$\theta_s(\boldsymbol{r}) = \frac{1}{\sqrt{n!}} \det \begin{vmatrix} \phi_1(\boldsymbol{r}_1) & \phi_2(\boldsymbol{r}_1) & \cdots & \phi_n(\boldsymbol{r}_1) \\ \phi_1(\boldsymbol{r}_2) & \phi_2(\boldsymbol{r}_2) & \cdots & \phi_n(\boldsymbol{r}_2) \\ \vdots & \vdots & \ddots & \vdots \\ \phi_1(\boldsymbol{r}_n) & \phi_2(\boldsymbol{r}_n) & \cdots & \phi_n(\boldsymbol{r}_n) \end{vmatrix} . \tag{11}$$

Equation (11) is the exact wave function of a system of uncharged fermions and thus an exact expression for the reference system. When the Kohn-Sham operator $\hat{f}^{KS}$ is applied to one of the Kohn-Sham orbitals the corresponding energy ϵ_i can be obtained by solving the one electron eigenvalue equation

$$\hat{f}^{KS}\phi_i = \epsilon_i \phi_i \, . \tag{12}$$

Every particle of the reference system is handled individually by considering its interaction with all other particles. To this end, the Kohn-Sham operator

$$\hat{f}^{KS} = -\frac{1}{2}\nabla^2 + V_s(\boldsymbol{r}) \tag{13}$$

consists of a potential V_s and a term describing the contribution from the kinetic energy. The potential V_s is chosen in a way that the resulting electron density of the non-interacting reference system ρ_s equals the electron density of the real interacting system ρ. This requirement can be achieved when specifying the contributing terms of the potential belonging to the interacting system. The contributions can be obtained by dividing the energy of the real system into a kinetic energy term $T_s[\rho(\boldsymbol{r})]$ containing the kinetic energy of the reference system, the Coulomb contribution $J[\rho(\boldsymbol{r})]$, a potential energy term $E_{ne}[\rho(\boldsymbol{r})]$ containing the repulsive energy between the electrons and the nuclei, and an $E_{xc}[\rho(\boldsymbol{r})]$ term that contains the unknown, non-classical contributions to the total energy

$$E[\rho(\boldsymbol{r})] = T_s[\rho(\boldsymbol{r})] + J[\rho(\boldsymbol{r})] + E_{ne}[\rho(\boldsymbol{r})] + E_{xc}[\rho(\boldsymbol{r})] \, . \tag{14}$$

The kinetic energy of the reference system can partially describe the kinetic energy of the real system but a remaining term $T_c[\rho(\boldsymbol{r})]$ must be added to the $T_s[\rho(\boldsymbol{r})]$ term to describe the excess in kinetic energy due to the charge interactions in the real system. The $T_c[\rho(\boldsymbol{r})]$ functional is included in the $E_{xc}[\rho(\boldsymbol{r})]$ term as its explicit form is also unknown. Thus, $E_{xc}[\rho(\boldsymbol{r})]$ contains all contributions whose explicit forms are unknown:

$$\begin{aligned} E_{xc}[\rho(\boldsymbol{r})] &= (T[\rho(\boldsymbol{r})] - T_s[\rho(\boldsymbol{r})]) + (E_{ee}[\rho(\boldsymbol{r})] - J[\rho(\boldsymbol{r})]) \\ &= T_c[\rho(\boldsymbol{r})] + (E_{ee}[\rho(\boldsymbol{r})] - J[\rho(\boldsymbol{r})]) \, . \end{aligned} \tag{15}$$

The advantage of expressing the kinetic energy as presented in equation (14) lies in the fact that the kinetic energy of the reference system can be easily obtained by

$$T_s = -\frac{1}{2}\sum_i^n < \phi_i|\nabla^2|\phi_i > . \tag{16}$$

In this way, the kinetic energy of the reference system is determined exactly, which represents an improved treatment of the kinetic energy compared to earlier applications of DFT. DFT approaches older than the Kohn-Sham approach often yielded very poor descriptions of molecular systems due to their high neglect of kinetic energy description.

Now, as the terms contributing to the total energy of the interacting system are specified as far as they are known, the Kohn-Sham orbitals ϕ_i can be obtained by solving the n one particle equations (12). With the Kohn-Sham orbitals, one can then compute the electron density of the reference system according to

$$\rho_s(\boldsymbol{r}) = \sum_i^n |\phi_i(\boldsymbol{r})|^2 . \tag{17}$$

By definition, $\rho_s(\boldsymbol{r})$ is equal to the ground state electron density of the real system. Thus, the ground state energy or any other property of the real system can be obtained from $\rho_s(\boldsymbol{r})$ by expressing equation (14) in terms of the Kohn-Sham orbitals

$$E[\rho(\boldsymbol{r})] = -\frac{1}{2}\sum_i^n < \phi_i|\nabla^2|\phi_i > +\frac{1}{2}\sum_i^n\sum_j^n \iint |\phi_i(\boldsymbol{r}_1)|^2 \frac{1}{\boldsymbol{r}_{12}} |\phi_j(\boldsymbol{r}_2)|^2 d\boldsymbol{r}_1 d\boldsymbol{r}_2 - \sum_i^n \int \sum_I^N \frac{Z_I}{\boldsymbol{r}_{1I}} |\phi_i(\boldsymbol{r}_1)|^2 d\boldsymbol{r}_1 + E_{xc}[\rho(\boldsymbol{r})] . \tag{18}$$

By expressing the total energy as presented in equation (18) the Kohn-Sham orbitals can now be varied according to the variational principle to obtain the ground state electron density. In summary, it can be stated that the Kohn-Sham approach describes a manner of accessing the ground state electron density of any given system by using a reference system of the same ground state electron density. Emphasis should be laid on the fact that the only approximation used in this method is based on the fact that no expression for the non classical $E_{xc}[\rho]$ functional is known. The Kohn-Sham orbitals used as trial functions do not lead to an approximation as they describe the reference system in an exact manner.[37]

2.3 Time-dependent DFT (TDDFT)

As we highlighted in the discussion of DFT, the use of this method is by its foundation limited to obtaining the ground state electron density and the corresponding ground state energy of the system. To extend DFT to excited states, one first needs to prove a unique connection between excited state electron densities and energies. As a way of extending the DFT approach to the treatment of excited states the time-dependent DFT (TDDFT) approach was developed. The formal foundations of TDDFT consist of two parts structurally very similar to the two Hohenberg-Kohn theorems for ground state DFT. In summary, an extension of the first Hohenberg-Kohn theorem to excited states is given by the Runge-Gross theorem[40], and the validation of the variational principle is achieved by relying on an action integral. A strategy to solve the excited-state formalism is provided by the derivation of the time-dependent Kohn-Sham equations.

2.3.1 Formal foundations

In analogy to the *proof of existence* in the Hohenberg-Kohn theorems, the Runge-Gross theorem[40] states that a unique mapping exists between the time-dependent electron density and a time-dependent external potential. Hereby, a difference to the ground state formalism is that the external potential is uniquely determined only up to a time-dependent function which leads to a time-dependent phase factor in the corresponding wave function. A proof by contradiction is carried out similar to the time-independent analogon to prove the unique mapping between the time-dependent electron density and the time-dependent external potential. The proof by contradiction proceeds in two steps and requires the external potential to be Taylor expandable around an initial time t_0. Furthermore, the proof makes use of the continuity equation relating the time-dependent electron density $\rho(\boldsymbol{r}, t)$ to the scalar current density $j(\boldsymbol{r}, t)$ via

$$\frac{\partial}{\partial t}\rho(\boldsymbol{r}, t) = -\nabla \cdot j(\boldsymbol{r}, t) \; . \tag{19}$$

In the first step of the proof, two potentials $v(\boldsymbol{r}, t)$ and $v'(\boldsymbol{r}, t)$, that are assumed to differ by a function that is not only time-dependent but does also depend on spatial coordinates, are constructed. The two differing potentials are shown to always lead to two different current densities $j(\boldsymbol{r}, t)$ and $j'(\boldsymbol{r}, t)$ at a time step infinitesimally later than t_0 even if one starts from two identical current densities at $t = t_0$. In the second step of the proof, a contradiction is used to show that two different current densities must always be caused by two different time-dependent electron densities $\rho(\boldsymbol{r}, t)$ and $\rho'(\boldsymbol{r}, t)$. To provoke the core contradiction, one uses the continuity equation to relate the time-dependent electron densities $\rho(\boldsymbol{r}, t)$ and $\rho'(\boldsymbol{r}, t)$ to the two external potentials $v(\boldsymbol{r}, t)$ and $v'(\boldsymbol{r}, t)$ that differ by a spatially variant function. By subsequently assuming that the potentials vanish identically the resulting equation yields a contradiction. This contradiction shows that one must start from two differing external potentials to obtain two different time-dependent electron densities.[41] With this one-to-one mapping being established, the external potential v and the time-dependent wave function are proven to be uniquely determined by the time-dependent electron density up to a function only varying in time

$$\rho(\boldsymbol{r}, t) \Rightarrow v[\rho](\boldsymbol{r}, t) + C(t) \Rightarrow \Psi[\rho](\boldsymbol{r}, t)e^{-i\alpha(t)} \; . \tag{20}$$

After assuring the one-to-one mapping presented in equation (20), the variational principle is shown to be valid.[40] The validity of the variational principle can be shown when expressing the wave function as the stationary point of an action integral. This action integral is equally a functional of the time-dependent electron density as it is the case for the wave function. When disposing of this information, the exact time-dependent electron density can be found by searching for the electron density that yields a stationary point for the action integral according to

$$\frac{\delta A[\rho]}{\delta \rho(\boldsymbol{r}, t)} = 0 \tag{21}$$

where A signifies the action integral.[41]

After the existence of a one-to-one mapping between the time-dependent electron density and the external potential as well as the validity of the variational principle has been

assured, it remains to define a practical approach to obtain the exact time-dependent electron density. In order to do so, the time-dependent Kohn-Sham approach was derived. This approach relies on the van Leeuwen theorem[42] which provides the link between the interacting system of interest and a fictitious non-interacting system, analogous to the time-independent Kohn-Sham approach. The van Leeuwen theorem states that the time-dependent electron density of an interacting system is uniquely reproduced by a non-interacting system with a different external potential but the same exact density. The exact time-dependent density of the non-interacting reference system is expressed as the sum over single-particle wave functions. By making use of the action integral and splitting the contributions to the action integral functional into known and unknown parts one arrives at a formulation similar to the Kohn-Sham approach in ground state DFT. In this formulation, again, no approximation would be necessary if an explicit expression of all contributing functionals was known.

In addition to the approximations required because no explicit form of the density functional is known, approximations targeting the time-dependence of the density functional were introduced to TDDFT. One approximation introduced in TDDFT is the adiabatic local density approximation (ALDA), which consists of neglecting the dependence of a current density on all previous time steps by only accounting for its dependence on the instantaneous time. Thus, when employing the ALDA, the history of how a certain electron density has developed over time is neglected. Thanks to the ALDA the same approximations to the unknown density functional as in ground state DFT can be utilized in TDDFT, an aspect highly facilitating practical usage of the TDDFT approach. However, these benefits come at the cost of incorrectly including only time-local contributions to a current density while furthermore using functional approximations that were designed to treat a system in its ground state.[41]

2.3.2 Linear-response TDDFT (LR-TDDFT)

As, so far, no strategy to determine excitation energies from the TDDFT framework has been provided, the linear-response TDDFT (LR-TDDFT) approach developed to tackle this problem shall be discussed. In the LR-TDDFT approach the system is not explicitly treated as time-dependent. Instead, a small perturbation is applied by exhibiting an initial system in its ground state to a sufficiently weak external potential. The response of the system to the applied potential is then expressed as a Taylor series and truncated after the first order. Accounting only for the linear response to the perturbation is justified as for most systems, only the linear response is of relevant magnitude. The core measure in the expression of the system's response to the perturbation is the density-density response function $\chi(\boldsymbol{r}, \boldsymbol{r}', t, t')$. When Fourier transformed into the frequency domain, χ possesses poles at the exact excitation energies of the system due to the $E^{\nu}_{el} - E^{0}_{el}$ term in the denominator being subtracted from the frequency.[43] When a basis of single-excitations between Kohn-Sham orbitals is used to express the density-density response function χ, one arrives at the pseudo-eigenvalue equation

$$\begin{bmatrix} \boldsymbol{A} & \boldsymbol{B} \\ \boldsymbol{B}^* & \boldsymbol{A}^* \end{bmatrix} \begin{bmatrix} \boldsymbol{X} \\ \boldsymbol{Y} \end{bmatrix} = \omega \begin{bmatrix} \boldsymbol{1} & \boldsymbol{0} \\ \boldsymbol{0} & -\boldsymbol{1} \end{bmatrix} \begin{bmatrix} \boldsymbol{X} \\ \boldsymbol{Y} \end{bmatrix} . \tag{22}$$

In this equation, ω and $-\omega$ correspond to the excitation and de-excitation energies while

one element of the $\boldsymbol{A}$ matrix describes the response of the density due to a change induced by excitation. One element of the $\boldsymbol{B}$ matrix describes the response of the electron density to a change induced by a de-excitation process while $\boldsymbol{X}$ and $\boldsymbol{Y}$ correspond to the excitation- and de-excitation amplitudes, respectively.[44] Regarding equation (22), emphasis should be laid on the fact that all matrices depend on ω. As long as this frequency dependence is retained, all multi-electron excitation processes can be described via the basis of single excitations due to the non-linear character of equation (22). When neglecting the frequency dependence of the matrices in equation (22), one arrives at the adiabatic approximation and the considered response becomes limited to single-electron excitation processes.[43] Therefore, the LR-TDDFT approach within the adiabatic approximation is not directly transferrable to excitation processes involving multiple electrons. Thanks to the neglect of all frequency dependence, the usage of ground state DFT functionals is also made possible for LR-TDDFT, which simplifies the application of this approach in excited state computations for molecules.

When applying further approximations to equation (22) consisting of neglecting the couplings to de-excitation processes, one arrives at the equation

$$\boldsymbol{AX} = \omega \boldsymbol{X} \tag{23}$$

which is a real eigenvalue equation and therefore easier to solve with existing numerical methods. The approach presented in equation (23), termed the Tamm-Dancoff approximation[45], is justified as long as the excitations in the molecule are well described by one single-electron process. For excitations showing this character the energetic contributions mostly come from diagonal elements of the $\boldsymbol{A}$ matrix in equation (22) while the off-diagonal $\boldsymbol{A}$, and the $\boldsymbol{B}$ elements have only negligible effect. Therefore, considering only the $\boldsymbol{A}$ matrix is valid for molecular excitations of the described character. Any practical implementation of LR-TDDFT employed today makes use of the adiabatic and the Tamm-Dancoff approximation, which highlights their indispensable role in extending the DFT approach to excited states.

2.4 Exploring the potential energy surfaces with geodesic interpolation

After the extensive discussion on the DFT and TDDFT methods, used to obtain static ground and excited state properties for chemical systems, an approach to explore different regions of the potential energy surface (PES) for given structures of a molecule shall be discussed. Before carrying out nuclear dynamics simulations on Ruwich that are of high computational cost, the potential regions connecting the predetermined S_1 minimum and the ground state were explored by carrying out static scans. A common strategy to perform a scan between two known molecular structures is the linear interpolation in internal coordinates (LIIC) approach. However, to perform an LIIC, molecular coordinates need to be expressed in internal coordinates to obtain a coordinate system where the movement of different atoms is as uncoupled as possible. Establishing a system of internal coordinates is not straightforward for a transition metal sandwich complex like Ruwich. The difficulty arises because the Ruwich structure contains a six-membered and a five-membered ring as well as the central Ru atom which is coordinated to eleven other atoms over relatively high distances. These two aspects render the determination of a well-chosen internal coordin-

ate system via any available algorithm complicated – if not unfeasible. Consequently, an approach differing from the LIIC in the choice of coordinate system was followed in this thesis.

The geodesic interpolation approach[46] employed provides an efficient and versatile coordinate representation that can be used to carry out interpolations between two Ruwich structures. The algorithm, aiming to find the mean energy pathway between any two structures, relies on expressing the shortest pathway on a PES as a geodesic curve. A geodesic curve can be thought of as the equivalent to a straight line in curved space. While a straight line is the shortest connection between two points on a plane, a geodesic curve is the shortest path between two points on a more complex surface. In any more complex space, the shortest distance between two points depends on the definition of measures for length and curvature. Usually, not only one but several options exist for the definition of these measures, referred to as the metric of the space. For the applied interpolation method to successfully find a geodesic curve that represents the desired pathway, properly choosing the metric is crucial. With a proper choice of metric that is never changed throughout the interpolation, the geodesic path is defined to equal the mean energy pathway between two points on a PES. With a consistently applied metric, one furthermore obtains interpolated structures that do not depend on the coordinate system chosen to carry out the interpolation. This aspect is highly beneficial as it allows for the method to carry out coordinate transformations in a highly specialized representation while yielding structures in universal xyz coordinates.

Regarding the high requirements for choosing the metric applied in the geodesic interpolation, it is crucial to realize that a rigorous definition of a mean energy pathway allows for only one possible choice of metric that yields a geodesic curve representing this mean energy pathway. Such a definition of a mean energy pathway was provided by Fukui et al.[47, 48] and leads to the metric defining a length element as

$$ds^2 = \left[\mathfrak{g}^{kl}\frac{\partial U}{\partial q^k}\frac{\partial U}{\partial q^l}\right]\mathfrak{g}_{ij}dq^i dq^j \tag{24}$$

where $\mathfrak{g}_{ij}$ signifies a local Euclidean metric, $\mathfrak{g}^{kl}$ its inverse and $\boldsymbol{q}$ are local coordinates. The definition of the metric presented in equation (24) shows that the derivative of the potential energy U with respect to changes in local coordinates is embedded into the length element. The metric is thus closely related to the shape of the PES. To clarify the appearance of a local Euclidean metric in equation (24) it should be mentioned that any complex space can be locally approximated around any point as a Euclidean space. This idea becomes more straightforward when imagining an ellipsoid like the earth whose surface, although corresponding to a curved space, can in close proximity to any given point be approximated by a plane. This concept is similar to locally approximating a one-dimensional curve by the straight tangent at a local point of the curve. The circumstance that a locally valid Euclidean space exists for every point in a complex space justifies the usage of a local Euclidean metric in equation (24). In addition, the advantageous circumstance that the metric and the resulting geodesic curve are independent of the choice of coordinate system allows for the application of a well-tailored Euclidean space. The local Euclidean space can always be re-determined throughout the interpolation when the boundaries of its validity are surpassed.

Although the choice to apply a metric that determines the geodesic curve to be the mean energy pathway has substantial advantages, the difficulty of needing to know the entire PES for the determination of a length element (see eq. (24)) arises. To circumvent this problem, the local coordinates $\boldsymbol{q}$ are chosen to contain local information on the PES, such that the PES resulting from the coordinate set $\boldsymbol{q}$ is nearly flat. It suffices to use atom-pairwise coordinates, expressed in terms of simple two-body potentials, e.g. the Lennard-Jones or the Morse potential, to let the local coordinates contain information on the PES. These two-body potentials contain most of the interactions necessary to ensure the physically meaningful movement of individual atoms in a given molecular structure. By approximating the unknown PES via locally valid coordinate sets containing two-body potential functions, the metric in equation (24) can be employed to yield the geodesic curve defined to represent the mean energy pathway between two molecular conformations.

The algorithmic procedure underlying the geodesic interpolation proceeds by first defining a user-determined number of images that divide the path between two molecular conformations A and B into several connected sub-paths. As a combination of subsequent geodesic curves is also a geodesic curve, just as a combination of several straight lines again yields a straight line, this approach does not alter the resulting mean energy pathway. The division into sub-paths is necessary as using a Euclidean metric and the approximation of the PES via two-body potential-based coordinate functions relies on considering a local environment around a given point of the complex space. The images can initially be located at any point between structures A and B avoiding the need for a uniform distribution provided by the user.

The length of the geodesic path between two images is approximated by using an upper and a lower bound to estimate an interval. The upper bound is obtained by considering that the geodesic curve is known to be shorter than any other path connecting the two images and following the curved surface. Consequently, considering the straight connection between two images in Cartesian coordinate space which corresponds to a curved path in the space of the interpolation metric, represents an upper bound to the geodesic path length. The space of all possible configurations, which contains the curved surface the geodesic lies on as a subspace, is considered to obtain an estimate of the lower bound. In this configuration space, a straight line connecting the two images can be determined. The fact that this straight path is shorter than the geodesic path indicates that the lower bound cannot lie on the defined curved surface. To clarify this statement, the curved PES the two images lie on can be imagined as the surface of the earth. When constructing a straight path between two points on the surface of the earth the corresponding length is always shorter than the length of any curved path following the earth's surface. However, from the perspective of a human being deemed to follow the earth's surface, the straight path, although shorter, is unfeasible. Similarly, a straight path connecting two points on a curved PES is unfeasible to be followed by the corresponding molecule.

Approximating the length of the geodesic path by relying on the interval determined via the upper and lower bound discussed above always leads to an overestimation. This circumstance can be seen as beneficial when combined with a path length optimization algorithm. Paths obtained during the optimization procedure are ensured to get closer to the geodesic path as their length is minimized. As soon as a minimum path length is reached, the respective path is known to correspond to the geodesic path. During the optimization procedure the total geodesic curve between A and B is obtained by individually minimiz-

ing the length of each sub-path by changing the set of coordinates an image corresponds to. This procedure is repeated several times until all of the images remain fixed. By combining all sub-paths, the total geodesic curve is obtained. Thanks to the independence of the resulting interpolation path on the coordinate representation this approach easily provides a set of interpolated structures in cartesian coordinates. When applying the geodesic interpolation to Ruwich, interpolated structures between the pre-determined ground state and S_1 minimum structures were obtained. The interpolated structures were further analyzed by carrying out LR-TDDFT calculations and examining the change of excitation character. Therefore, the geodesic interpolation approach allowed for a pre-investigation of the PES region around minimized structures, yielding a first estimate of the Ruwich excited state dynamics.

2.5 Nuclear dynamics on more than one electronic state: spawning approaches

The energies and gradients for the electronic state the molecule is occupying need to be considered to explore the dynamical behavior of a molecular system. In cases where the electronic structure undergoes only small variations for changes in nuclear coordinates and couplings of different electronic states are sufficiently small the approximation to neglect all couplings between the occupied state and all other electronic states due to nuclear motion is valid. The requirements for this Born-Oppenheimer (BO) approximation are most likely fulfilled when the molecular system evolves on an electronic state energetically well separated from other electronic states. For a molecular system following this tendency, carrying out adiabatic dynamics, an approach only considering one electronic PES, is well justified. However, including the interaction between electronic states becomes especially crucial when examining systems with several electronic states close in energy as is often the case for transition metal complexes. To this end, nuclear dynamics methods have been developed that employ the nonadiabatic approach which includes the treatment of interactions between nuclear amplitudes evolving on different electronic states. It is inevitable to consider the BH representation[49] to get an understanding of nonadiabatic dynamics methods. When expressed in the BH representation, the complete molecular wave function $\Psi(\boldsymbol{r}, \boldsymbol{R}, t)$ is expanded in the basis of its electronic eigenstates $\Phi_\nu(\boldsymbol{r}; \boldsymbol{R})$

$$\Psi(\boldsymbol{r}, \boldsymbol{R}, t) = \sum_{\nu}^{\infty} \Phi_\nu(\boldsymbol{r}; \boldsymbol{R}) X_\nu(\boldsymbol{R}, t) \tag{25}$$

where ν denotes a particular electronic state and $X_\nu(\boldsymbol{R}; t)$ represents the corresponding expansion coefficient referred to as the nuclear amplitude. When carrying out adiabatic dynamics, only one electronic eigenstate Φ_ν is considered and the molecular wave function is reduced to

$$\Psi(\boldsymbol{r}, \boldsymbol{R}, t) \approx \Phi_\nu(\boldsymbol{r}; \boldsymbol{R}) X_\nu(\boldsymbol{R}, t) \ . \tag{26}$$

In the limit of setting ν to one particular number the exact BH representation boils down to the BO approximation[50]. The BO approximation is valid as long as the electronic structure undergoes only small variations for changes in nuclear coordinates and couplings of different electronic states are sufficiently small.

In the course of this thesis both molecular dynamics approaches, the adiabatic and the nonadiabatic approach were employed. The utilization of both methods allows us to evaluate the effect of neglecting nonadiabatic effects. Hereby, the role of population transfer between electronic states in the excited state dynamics of Ruwich and the potential influence of these effects on the flexibility to undergo hapticity changes can be examined.

In the BH picture, the electronic structure information required to propagate the nuclear amplitudes is obtained from methods such as DFT and LR-TDDFT as discussed in the previous chapter. To obtain the nuclear amplitudes X_ν and their time evolution another field of computational quantum chemistry methods must be entered, namely that of nonadiabatic molecular dynamics. This section will focus on different approaches to determine the time evolution of the nuclear amplitudes on more than one electronic state in a similar way as the previous section is directed to obtaining the electronic eigenstates.

2.5.1 Expressing the molecular wave function in a basis of frozen Gaussians

It is priorly necessary to find a representation of the molecular wave function Ψ rendering the propagation as efficient as possible to arrive at a feasible method for propagating the nuclear amplitudes X_ν. A common approach lies in representing the nuclear amplitudes X_ν via a flexible grid of Gaussian functions with grid points corresponding to the directly time-dependent central positions and momenta.[51] Having time-dependent grid points allows for a relocation of the grid whenever necessary, avoiding the need to predetermine representative points in phase space. Using the grid of flexible Gaussians, the nuclear amplitude of a particular state ν is expressed as

$$X_\nu(\boldsymbol{R},t) = \sum_k^{N_{TBFs}^\nu} C_k^{(\nu)}(t)\chi_k^{(\nu)}(\boldsymbol{R};\bar{\boldsymbol{R}}_k^{(\nu)}(t),\bar{\boldsymbol{P}}_k^{(\nu)}(t),\boldsymbol{\alpha}_k^{(\nu)},\bar{\gamma}_k^{(\nu)}(t)) \tag{27}$$

where k denotes a particular TBF among the N_{TBFs}^ν many TBFs evolving on state ν. $\gamma_k^{(\nu)}$ is time-dependent phase factors while $\alpha_k^{(\nu)}$ corresponds to the time-independent width of the TBF k on state ν while $\bar{R}_k^{(\nu)}$ and $\bar{P}_k^{(\nu)}$ are the time-dependent central position and momentum of TBF k. Going further down the expansion hierarchy, each of the multidimensional TBFs $\chi_k^{(\nu)}$ is expressed as a $3N_n$ dimensional product of one-dimensional Gaussians, where N_n denotes the number of nuclei

$$\chi_k^{(\nu)}(\boldsymbol{R};\bar{\boldsymbol{R}}_k^{(\nu)}(t),\bar{\boldsymbol{P}}_k^{(\nu)}(t),\alpha_k^{(\nu)}(t),\bar{\gamma}_k^{(\nu)}(t)) = e^{i\bar{\gamma}_k^{(\nu)}(t)}\prod_\rho^{3N_n}\chi_{k\rho}^{(\nu)}(R_\rho;\bar{R}_{k\rho}^{(\nu)}(t),\bar{P}_{k\rho}^{(\nu)}(t),\alpha_{k\rho}^{(\nu)}(t))\ . \tag{28}$$

To arrive at the end of the expansion, each one-dimensional Gaussian $\chi_{k\rho}^{(\nu)}$ has the explicit form

$$\chi_{k\rho}^{(\nu)}(R_\rho; \bar{R}_{k\rho}^{(\nu)}(t), \bar{P}_{k\rho}^{(\nu)}(t), \alpha_{k\rho}^{(\nu)}(t)) = \left(\frac{2\alpha_{k\rho}^{(\nu)}}{\pi}\right)^{\frac{1}{4}} \exp\left(-\alpha_{k\rho}^{(\nu)}(R_\rho - \bar{R}_{k\rho}^{(\nu)})^2 + i\bar{P}_{k\rho}^{(\nu)}(R_\rho - \bar{R}_{k\rho}^{(\nu)})\right) . \tag{29}$$

Having established the basis of the molecular wave function $\Psi(r, R, t)$ to be used in the nonadiabatic molecular dynamics, it remains to insert this expression of $\Psi(r, R, t)$ into the TDSE presented in equation (1). When inserting the nuclear amplitudes expressed in terms of the flexible Gaussian grid into the BH one obtains

$$\Psi(\boldsymbol{r}, \boldsymbol{R}, t) = \sum_{\nu}^{\infty} \sum_{k}^{N_{TBFs}^{\nu}} C_k^{(\nu)}(t)\chi_k^{(\nu)}(\boldsymbol{R}; \bar{\boldsymbol{R}}_k^{(\nu)}(t), \bar{\boldsymbol{P}}_k^{(\nu)}(t), \boldsymbol{\alpha}_k^{(\nu)}(t), \bar{\gamma}_k^{(\nu)}(t))\Phi_\nu(\boldsymbol{r}; \boldsymbol{R}) . \tag{30}$$

Expressing the TDSE by using this form of the total molecular wave function yields

$$\begin{aligned} &\hat{H}(\boldsymbol{r}, \boldsymbol{R}) \sum_{\nu}^{\infty} \sum_{k}^{N_{TBFs}^{\nu}} C_k^{(\nu)}(t)\chi_k^{(\nu)}(\boldsymbol{R}; \bar{\boldsymbol{R}}_k^{(\nu)}(t), \bar{\boldsymbol{P}}_k^{(\nu)}(t), \boldsymbol{\alpha}_k^{(\nu)}(t), \bar{\gamma}_k^{(\nu)}(t))\Phi_\nu(\boldsymbol{r}; \boldsymbol{R}) \\ &= i\hbar \frac{\partial}{\partial t} \sum_{\nu}^{\infty} \sum_{k}^{N_{TBFs}^{\nu}} C_k^{(\nu)}(t)\chi_k^{(\nu)}(\boldsymbol{R}; \bar{\boldsymbol{R}}_k^{(\nu)}(t), \bar{\boldsymbol{P}}_k^{(\nu)}(t), \boldsymbol{\alpha}_k^{(\nu)}(t), \bar{\gamma}_k^{(\nu)}(t))\Phi_\nu(\boldsymbol{r}; \boldsymbol{R}) . \end{aligned} \tag{31}$$

By left multiplying the expression in equation (31) with $[\Phi_\mu(r; R)\chi_{k'}^{(\mu)}(R; \bar{R}_{k'}^{(\mu)}(t), \bar{P}_{k'}^{(\mu)}(t), \alpha_{k'}^{(\mu)}(t), \gamma_{k'}^{(\mu)}(t))]^*$ and integrating over the whole electronic and nuclear coordinate space one obtains

$$\boldsymbol{H}\boldsymbol{C} = i\hbar\left(\boldsymbol{S}\frac{d\boldsymbol{C}}{dt} + \dot{\boldsymbol{S}}\boldsymbol{C}\right) , \tag{32}$$

where $\boldsymbol{H}$ denotes the Hamiltonian matrix, and $\boldsymbol{S}$ and $\boldsymbol{C}$ stand for the overlap and coefficient matrix of the wave function Ψ. $\dot{\boldsymbol{S}}$ signifies the partial time derivative matrix of the overlap matrix $\boldsymbol{S}$ where the time derivative between two TBFs is obtained according to

$$(\dot{\boldsymbol{S}})_{kk'}^{\mu\nu} = \langle\chi_k^{(\mu)}|\frac{\partial}{\partial t}\chi_{k'}^{(\nu)}\rangle_{\boldsymbol{R}}\delta_{\mu\nu} . \tag{33}$$

Equation (32) can be solved after a term for the time evolution of the coefficient matrix $\frac{d\boldsymbol{C}}{dt}$ by carrying out the following transformations

$$\begin{aligned} \boldsymbol{H}\boldsymbol{C} - i\hbar\dot{\boldsymbol{S}}\boldsymbol{C} &= i\hbar\boldsymbol{S}\frac{d\boldsymbol{C}}{dt} \\ i\hbar\frac{d\boldsymbol{C}}{dt} &= \boldsymbol{S}^{-1}\boldsymbol{H}\boldsymbol{C} - i\hbar\boldsymbol{S}^{-1}\dot{\boldsymbol{S}}\boldsymbol{C} \\ \frac{d\boldsymbol{C}}{dt} &= -i\boldsymbol{S}^{-1}\boldsymbol{H}\boldsymbol{C} - \boldsymbol{S}^{-1}\dot{\boldsymbol{S}}\boldsymbol{C} \\ &= -i\boldsymbol{S}^{-1}\left(\boldsymbol{H}\boldsymbol{C} - i\dot{\boldsymbol{S}}\boldsymbol{C}\right) \\ &= -i\boldsymbol{S}^{-1}\left((\boldsymbol{H} - i\dot{\boldsymbol{S}})\boldsymbol{C}\right) \end{aligned} \tag{34}$$

yielding the equation of motion

$$\frac{d\boldsymbol{C}}{dt} = -i\boldsymbol{S}^{-1}\left((\boldsymbol{H} - i\dot{\boldsymbol{S}})\boldsymbol{C}\right) \ . \tag{35}$$

Equation (35), being the TDSE expressed in terms of the flexible TBF grid, represents the common expression for the time change of the coefficient matrix. As equation (35) treats all states as coupled, no approximation has been made to obtain this expression of the TDSE that remains numerically solvable as long as a limited number of electronic states is considered. The coefficient matrix $\boldsymbol{C}$ needs to be propagated in time to arrive at a numerical solution. To this end, a choice of propagation algorithm representing the movement of a nuclear wave function is required. Hereby, the options lie in either employing an algorithm that aims to accurately represent the movement of a wave function or choosing a classical propagation algorithm not including this characteristic behavior. While both approaches lead to the exact solution, the former requires a far smaller number of TBFs than the latter approach as the character of a wave function is preserved. In the variational multi-configuration gaussian (vMCG) method[52] the algorithm includes wave function behavior while all couplings between Gaussians on all states are considered. From this propagation technique, it follows that vMCG requires less TBFs but consequently the propagation algorithm becomes enormously complicated. A differing propagation approach is chosen in the FMS method[53], where the TBFs are propagated classically by using standard equations of motion to obtain the mean positions and momenta as well as the phase of each one-dimensional Gaussian separately. While a much higher number of TBFs is required in the FMS approach than in vMCG, the advantage lies in the simplicity of the propagation algorithm facilitating the implementation of FMS.

2.5.2 From FMS to the AIMS approach

Although an extensive basis set is required in FMS, one starts the dynamics with a certain minimal set, whose number and individual complex amplitudes are chosen to represent a suitable initial condition. The initial set is extended throughout the dynamics by spawning new TBFs whenever necessary. Hereby, each initial TBF, serving as the parent of its branch β, can spawn a in theory unlimited number of so-called child TBFs. In an FMS simulation, the number of branches is thus equal to the number of initial TBFs. The newly created TBFs on other electronic states ensures that all interaction between nuclear population is described but only taken into account when playing a significant role in the dynamics. To achieve this, the FMS propagation algorithm contains a spawning algorithm handling the

apparition of new TBFs. It is required to focus on the coefficient evolution on one state μ that can be expressed as

$$\frac{d\boldsymbol{C}^{\mu}}{dt} = -i(\boldsymbol{S}^{-1})_{\mu\mu}\left((\boldsymbol{H}_{\mu\mu} - i\dot{\boldsymbol{S}}_{\mu\mu})\boldsymbol{C}^{\mu} + \sum_{\nu\neq\mu}^{\infty}\boldsymbol{H}_{\mu\nu}\boldsymbol{C}^{\nu}\right) \tag{36}$$

to discuss the functionality of the spawning algorithm. Equation (36) describes the evolution of the coefficient $\boldsymbol{C}^{\mu}$ on one electronic state μ where now the term $\sum_{\nu\neq\mu}^{\infty}\boldsymbol{H}_{\mu\nu}\boldsymbol{C}^{\nu}$ contains the coupling to all other states ν. From expressing the equation of motion with respect to one state two distinct forms of couplings, the intrastate ($\mu = \nu$) and interstate ($\mu \neq \nu$) interactions arise. The number of these intrastate and interstate couplings grows over time and the dimensionality of the $\boldsymbol{H}$ matrix increases as more TBFs are created within the spawning algorithm whenever an existing TBF enters a region of strong interstate coupling. To obtain an explicit form of the intrastate and interstate couplings it is necessary to focus on one element $(\boldsymbol{H})^{\mu,\nu}_{k\beta,k'\beta'}$ of the Hamiltonian matrix, describing the coupling between a TBF k of branch β on state μ and a second TBF k' of branch β' on state ν

$$(\boldsymbol{H})^{\mu,\nu}_{k\beta,k'\beta'} = \left\langle \Phi_{\mu}\chi^{(\mu)}_{k\beta}|\hat{H}|\chi^{(\nu)}_{k'\beta'}\Phi_{\nu}\right\rangle_{\boldsymbol{r},\boldsymbol{R}} . \tag{37}$$

With the contributions to the Hamiltonian presented in equation (2) one obtains

$$\begin{aligned}(\boldsymbol{H})^{\mu,\nu}_{k\beta,k'\beta'} =& \langle\chi^{(\mu)}_{k\beta}|\hat{T}_n|\chi^{(\nu)}_{k'\beta'}\rangle_{\boldsymbol{R}}\,\delta_{\mu\nu} + \langle\chi^{(\mu)}_{k\beta}|E^{el}_{\nu}|\chi^{(\nu)}_{k'\beta'}\rangle_{\boldsymbol{R}}\,\delta_{\mu\nu} \\ &- \sum_{\rho}^{3N_n}\frac{1}{M_\rho}\langle\chi^{(\mu)}_{k\beta}|\langle\Phi_{\mu}|\frac{\partial}{\partial R_\rho}|\Phi_{\nu}\rangle_{\boldsymbol{r}}\frac{\partial}{\partial R_\rho}|\chi^{(\nu)}_{k'\beta'}\rangle_{\boldsymbol{R}} \\ &- \sum_{\rho}^{3N_n}\frac{1}{2M_\rho}\langle\chi^{(\mu)}_{k\beta}|\langle\Phi_{\mu}|\frac{\partial^2}{\partial R^2_\rho}|\Phi_{\nu}\rangle_{\boldsymbol{r}}|\chi^{(\nu)}_{k'\beta'}\rangle_{\boldsymbol{R}}\end{aligned} \tag{38}$$

where different coupling terms become relevant, depending on whether the two TBFs evolve on the same state ($\mu = \nu$) or on different states ($\mu \neq \nu$). If the TBFs k and k' evolve on the same state the first two terms in equation (38) containing the $\delta_{\mu\nu}$, as well as the diagonal elements of the second order derivative, the diagonal Born-Oppenheimer corrections (DBOC)s, determine the interaction. If the two TBFs evolve on different states, all terms with $\delta_{\mu\nu}$ vanish and the elements of the first order derivative in equation (38) and the off-diagonal elements in the second order derivative guide the interaction. The first-order derivative contains the term

$$\boldsymbol{d}_{\mu\nu}(\boldsymbol{R}) = \langle\Phi_{\mu}|\frac{\partial}{\partial\boldsymbol{R}}|\Phi_{\nu}\rangle_{\boldsymbol{r}} \tag{39}$$

referred to as the nonadiabatic coupling term. This vector, describing the overlap between the electronic wave functions of two different states μ and ν with respect to a change in nuclear coordinates governs the interaction between the two TBFs in states μ and ν. The second-order contributions to intra and inter-state couplings shown in the last summand of equation (38) are usually neglected in FMS methods when evaluating the interaction between TBFs. The interstate couplings are required to guide the spawning algorithm that

lies at the heart of the FMS approach and coined the name the resulting family of dynamics methods. The spawning algorithm ensures sufficient interaction between TBFs on different electronic states. A coupling criterion in the form of an effective nonadiabatic coupling is monitored for each existing TBF with respect to all other electronic states to assess the necessity of spawning a new TBF. The hereby employed effective nonadiabatic coupling $\Lambda_{\mu\nu}^{eff}(\bar{\boldsymbol{R}}_{k\beta}^{(\nu)})$ can either be simply defined as the modulus of the nonadiabatic coupling

$$\Lambda_{\mu\nu}^{eff}(\bar{\boldsymbol{R}}_{k\beta}^{(\nu)}) = |\boldsymbol{d}_{\mu\nu}(\bar{\boldsymbol{R}}_{k\beta}^{(\nu)})| \tag{40}$$

or as the projection onto the classical velocities of the TBF under consideration

$$\Lambda_{\mu\nu}^{eff}(\bar{\boldsymbol{R}}_{k\beta}^{(\nu)}) = \boldsymbol{d}_{\mu\nu}(\bar{\boldsymbol{R}}_{k\beta}^{(\nu)}) \cdot \dot{\bar{\boldsymbol{R}}}_{k\beta}^{(\nu)} \, . \tag{41}$$

As soon as the effective nonadiabatic coupling $\Lambda_{\mu\nu}^{eff}$ exceeds a certain threshold, the spawning algorithm is entered. At this instant, the classical propagation of the TBF that evoked the spawning mode is continued, while the evolution of all other TBFs is paused. This individual propagation started from the time step t_{entry} proceeds until the effective nonadiabatic coupling $\Lambda_{\mu\nu}^{eff}$ reaches a maximum. The nuclear coordinates obtained at this maximum are used to spawn a new TBF that is placed at state μ at a time noted as the spawning time t_{spawn}. After the actual spawning was performed, both TBFs, the parent on state ν and the child on state μ, are back-propagated until the time t_{entry} is reached. The back-propagation is necessary as an immediate propagation at the time t_{spawn} would introduce discontinuities due to the child TBF's instantaneous appearance on the state μ at an instant where its coupling between both TBFs peaks. Back-propagating ensures that the child enters when the effective coupling $\Lambda_{\mu\nu}^{eff}$ is closely just above the considered threshold allowing for the interaction between parent and child to develop smoothly over time. When the parent and the child are both back at t_{entry}, the propagation of all TBFs that existed before t_{entry} and the newly spawned child is continued normally. Now, population transfer can take place between the parent and child TBFs allowing for an accurate description of nuclear amplitude evolving on energetically close electronic states.

If one uses the FMS approach described above – just as it is – to spawn new TBF whenever necessary according to the effective nonadiabatic coupling and computes all intra- and interstate couplings as described, the propagation of the molecular wave function is carried out exactly, although the TBF parameters are propagated classically. However, in treating a molecular system, a high number of TBFs will most likely be spawned during the dynamics leading to a continuous increase in the number of Hamiltonian elements to be computed. This problematic scaling of the FMS method led to the introduction of two approximations that gave birth to the AIMS approach.[54][55] Before discussing these two approximations, it needs to be stated that an important but often not explicitly mentioned approximation lies in the fact that whenever dealing with a molecular system it is impossible to include all electronic eigenstates requiring a limit on the number of states to include. Hereby, it is not straightforward to determine the electronic eigenstates of the system crucial to describe the processes under investigation. Neglecting a state although it would show to become highly populated in the simulation can only lead to results incorrectly picturing the system's dynamics. Choosing the set of electronic states becomes especially relevant when considering a transition metal complex such as Ruwich. The occurrence of d-orbitals in the chemically

relevant energy frame leads to electronic eigenstates prone to be close in energy over a large interval of nuclear coordinates making it complicated to determine the states accessible to the photo-excited system. While a system such as Ruwich requires the inclusion of a high number of electronic eigenstates, this manifold of states also leads to a high number of spawning events, especially as the states are energetically close. This vicious cycle, causing the computational demand of the simulation to explode rapidly, requires for a careful limitation of electronic states to include. Aside from this general approach that would be necessary for any practical application involving molecular systems, the more prominent approximations characterizing AIMS are the saddle point approximation (SPA0) and the independent first generation approximation (IFGA). The SPA0 arises because the calculation of the intra- and interstate couplings arising from the Hamiltonian matrix elements (see eq. (38) causes a major problem in any molecular application. To compute any of the integrals containing electronic structure quantities and integrate over the whole nuclear coordinate space, it is necessary to know the electronic structure quantity of interest at any possible nuclear configuration. This is not possible without using pre-computed PESs which are in most applications inaccessible. Therefore, the SPA0 comes into play for any given integral containing an electronic structure quantity, as the nonadiabatic coupling between two TBFs

$$(\boldsymbol{d})^{\mu\nu}_{k\beta,k'\beta'} = \langle \chi^{(\mu)}_{k\beta} | \langle \Phi_\mu | \frac{\partial}{\partial \boldsymbol{R}} | \Phi_\nu \rangle_{\boldsymbol{r}} | \chi^{(\nu)}_{k'\beta'} \rangle_{\boldsymbol{R}} \, . \tag{42}$$

Now, instead of considering each TBF individually, the centroid position between the two TBFs is defined as

$$\bar{\boldsymbol{R}}^{(\mu\nu)}_{k\beta,k'\beta'} = \frac{\bar{\boldsymbol{R}}^{(\mu)}_{k\beta} + \bar{\boldsymbol{R}}^{(\nu)}_{k'\beta'}}{2} \, . \tag{43}$$

The nonadiabatic coupling element, or any other electronic structure quantity of interest is then expressed as a Taylor series around this centroid position and truncated after the zeroth order, leaving only the term

$$\boldsymbol{d}_{\mu\nu}(\boldsymbol{R}) \approx \boldsymbol{d}_{\mu\nu}(\bar{\boldsymbol{R}}^{(\mu\nu)}_{k\beta,k'\beta'}) \, . \tag{44}$$

Boiling the contribution of any electronic structure element down to the value at the centroid position of the two TBFs only works surprisingly well because the density of a Gaussian function is localized in space due to its inherent symmetry. Thus, the most relevant electronic structure contributions are those at positions close to the mutual centre of the Gaussians. At all other positions, the overlap between the TBFs is so small that corresponding electronic structure quantities become weighted out. The SPA0 allows for carrying out AIMS dynamics on the fly without the need of precomputing PESs in a predefined nuclear coordinate space.

The second approximation applied in AIMS – the IFGA – consists of neglecting any couplings between TBFs that belong to different branches. This approximation, of course reducing the amount of couplings required to compute quite substantially, is especially accurate in molecular excitation processes. This is owed to the fact that an initial wave packet would usually choose to spread out far already in the first steps after the excitation. For TBFs belonging to different branches, this behavior implies that these TBFs move far

away from each other in the first steps of the simulation, making it irrelevant to consider their interactions. Thanks to the IFGA, one can sample every initial TBF separately in a practical approach allowing for the independent simulation of every parent TBF.

2.5.3 Keeping the number of TBFs to a minimum: the AIMSWISS approach

In an AIMS simulation, the number of TBFs and therefore the computational demand can increase quite rapidly. Within this large set of TBFs it can quickly happen that certain TBFs separate far from each other within only a few time steps causing their couplings to become negligeably small. These couplings between well-separated TBFs still bring their contribution to the overall computational effort of the simulation although they do not contribute important information. It would prove beneficial to consider well-separated TBFs and their respective offsprings as separated branches to avoid the computation of these non-insightful couplings. By treating uncoupled TBF branches separately one arrives at an approximation similar to the IFGA with comparable computational benefits. An approach of this kind is provided by stochastic selection AIMS methods[56], where a selection process between two TBFs is initiated as soon as a user-defined threshold defines them as separate. The downside of stochastic selection AIMS methods lies in the usage of a user-determined selection parameter that is assumed to be applicable to every single TBF in the simulation. Finding one suitable parameter for all TBFs is not only a cumbersome task to be left out to the user but might even be impossible in more complicated simulations. Here, the AIMSWISS approach[57] provides a rescue, avoiding the problem of defining a selection threshold. This is achieved by using a decoupling parameter individually determined for every parent-child pair without the requirement of user input. As such, the Schwartz criterion, which approximates the overlap decay time of two Gaussians evolving on different PESs as a Gaussian, is adapted to apply to the AIMS approach. With the Schwartz criterion, a selection rule only relying on input from the two TBFs under consideration is obtained. The criterion employs the idea that two Gaussians with an identical initial distribution in phase space have an overlap decay only depending on the initial nuclear forces that act on the central position of each Gaussian. Using the Schwartz criterion in spawning dynamics allows for the computation of an overlap decay time for a pair of TBFs at the event of their spawning. The so-obtained decay time determines when the two trajectories will be sufficiently uncoupled to carry out a selection process. For the Schwartz criterion to be valid the two Gaussians must show sufficient similarity in their initial conditions. This requirement is fulfilled for a pair of parent-child TBFs as the decay time is computed directly during the spawning process, at the time t_{spawn} when the child TBF is still a close enough portrayal of its parent. In practice, the AIMSWISS algorithm employs the Schwartz criterion to initiate the selection process by proceeding via the following steps. After the parent and child TBF have been propagated from the time t_{entry} until t_{spawn}, their overlap decay time τ_D is calculated according to

$$\tau_D = \frac{1}{4}\left((\bar{\boldsymbol{F}}_k^{\mu}(t_{spawn}) - \bar{\boldsymbol{F}}_{k'}^{\nu}(t_{spawn}))^T \boldsymbol{\alpha}^{-1} (\bar{\boldsymbol{F}}_k^{\mu}(t_{spawn}) - \bar{\boldsymbol{F}}_{k'}^{\nu}(t_{spawn}))\right)^{-\frac{1}{2}} . \tag{45}$$

As can be seen from equation (45), τ_D takes no other input than the nuclear forces at the central position for each TBF. After calculating τ_D the propagation of all TBFs is continued until the selection time t_{SS} equal to $t_{spawn} + \tau_D$ is reached. At the selection time, the overlap

of parent and child is predicted to have decayed to $\exp(-1)$ of its initial maximum at t_{spawn}. To evaluate the prediction, the actual overlap is calculated and a warning is issued to the user if this value exceeds $\exp(-1)$ of the initial overlap. Checking the validity of the approximated overlap decay time τ_D at every selection event provides an automated evaluation of the selection criterion. Then, the population of parent and child branches, computed by taking into account any new TBFs possibly spawned in either branch, are evaluated following the Monte Carlo criterion to determine the branch to be maintained in the simulation while the other branch is discarded. After renormalising the remaining TBFs the dynamics is continued according to the standard AIMS approach.

While the adaptation of the Schwartz criterion ensures that the coupling between parent and child TBF is considered until it becomes negligible, the approach does not account for any children of different branches that potentially become coupled as a result of the simulation. It should thus be highlighted that the selection criterion imposed by AIMSWISS assumes not only that parent and child will become uncoupled but also that their respective offspring separate from the respective other branch. Furthermore, it is important to note that, although AIMSWISS represents an approximation to AIMS the approach should not be seen as a separate theory as the AIMS dynamics can always be recovered from AIMSWISS by setting τ_D to infinity.

In the course of this thesis, both dynamics approaches AIMS and AIMSWISS shall be applied to simulate the excited state dynamics of Ruwich while their results shall be compared in order to examine the ability of AIMSWISS of correctly predicting decoherence times for an organometallic complex. To analyze the results obtained with AIMS and AIMSWISS, it is necessary to compute observables meaningful to the dynamics of Ruwich. Therefore, it shall in the following be clarified how observables and state populations can be obtained from AIMS and from AIMSWISS.

2.5.4 Calculating observables within the multiple spawning framework

From the simulation data obtained throughout this thesis, several nuclear coordinate-based observables were calculated. The so-obtained geometrical measures and their role in describing geometry changes of Ruwich will be discussed with further detail in section 4. To calculate any observable from AIMS or AIMSWISS trajectories it has to be considered that averaging over the individual observables separately calculated for each trajectory does not provide the correct result. This circumstance is justified by the fact that the TBFs in spawning dynamics do not have equally distributed occupations but often show populations differing substantially because interaction processes between TBFs are taken into account. Therefore, it is necessary to evaluate the complex expansion coefficient of each TBF to obtain its population at every time step. Furthermore, as the TBFs do not form an orthonormal basis they are linearly dependent causing their overlaps to be non-zero. Accounting for the overlap of each pair of TBFs present at a time step is required to obtain observables that contain a correct description of how the population is distributed.

When an observable O corresponding to the operator $\hat{O}$ is calculated via

$$O(t) = \frac{\langle \Psi(t)|\hat{O}|\Psi(t)\rangle_{r,R}}{\langle \Psi(t)|\Psi(t)\rangle_{r,R}} \tag{46}$$

one can omit the denominator as the molecular wave function Ψ is normalized. Inserting Ψ expressed in the basis of the TBFs into equation (46) yields

$$O(t) = \sum_{\mu\nu}^{\infty} \left(\sum_{k}^{N_{TBF\mu}(t)} \sum_{k'}^{N_{TBF\nu}(t)} (C_k^{\mu}(t))^* C_{k'}^{\nu}(t) \langle \Phi_m u \chi_k^{(\mu)} | \hat{O} | \chi_{k'}^{\nu} \Phi_n u \rangle_{\boldsymbol{r},\boldsymbol{R}} \right) . \tag{47}$$

When applying the projection operator $\hat{P}^{\lambda} = |\Phi_\lambda\rangle\langle\Phi_\lambda|$ in equation (47) as an example for $\hat{O}$ one obtains the population on state λ

$$P^{\lambda}(t) = \sum_{\mu\nu}^{\infty} \left(\sum_{k}^{N_{TBF\mu}(t)} \sum_{k'}^{N_{TBF\nu}(t)} (C_k^{\mu}(t))^* C_{k'}^{\nu}(t) \langle \Phi_\mu \chi_k^{(\mu)} | \Phi_\lambda \rangle \langle \Phi_\lambda | \chi_{k'}^{(\nu)} \Phi_\nu \rangle_{\boldsymbol{r},\boldsymbol{R}} \right) \tag{48}$$

which boils down to

$$\begin{aligned} P^{\lambda}(t) &= \sum_{k,k'}^{N_{TBF\lambda}(t)} (C_k^{\lambda}(t))^* C_{k'}^{\lambda}(t) \langle \chi_k^{(\lambda)} | \chi_{k'}^{(\lambda)} \rangle_{\boldsymbol{R}} \\ &= \sum_{k,k'}^{N_{TBF\lambda}(t)} (C_k^{\lambda}(t))^* C_{k'}^{\lambda}(t) (\boldsymbol{S})_{kk'}^{\lambda\lambda} . \end{aligned} \tag{49}$$

as the electronic eigenstates Φ form an orthonormal basis. Equation (49) yields the population of each electronic state λ for each time step of the AIMS or AIMSWISS simulation. As the IFGA is applied it suffices to calculate the average of each observable for different branches β at every time step

$$O(t) \approx \frac{1}{N_{ini}} \sum_{\beta}^{N_{ini}} \frac{\langle \Psi^{\beta}(t) | \hat{O} | \Psi^{\beta}(t) \rangle_{\boldsymbol{r},\boldsymbol{R}}}{\langle \Psi^{\beta}(t) | \Psi^{\beta}(t) \rangle_{\boldsymbol{r},\boldsymbol{R}}} \tag{50}$$

where one can use the number of initial TBFs N_{ini} to sum over all β, as the number of initial TBFs determines the number of branches of the simulation.

In this thesis, all AIMS and AIMSWISS observables were obtained by first computing the individual value for each trajectory. Then, the individual values of all trajectories present at a certain time step were multiplied by the absolute value of their corresponding complex expansion coefficient. The so obtained population-weighted properties were summed over to give one total property as seen in equation (49) for the projection operator. It is owed to the weighting by population that discrete properties, such as the hapticity describing the binding number in an organometallic complex, can take in-between values when computed for spawning dynamics simulations.

3 Computational details

3.1 Electronic structure calculations

In all ground state electronic structure calculations we employed the DFT method using the functional ωB97XD[58] with type 3 dispersion corrections[59] and the cc-pVDZ[60] basis set, unless otherwise stated. For the Ru atom, we applied an effective core potential consisting of the LANL2DZ basis set[61][62]. For the excited state calculations, LR-TDDFT was the method of choice, where the number of included excited states was set to 4. The maximum number of Davidson iterations in the LR-TDDFT calculations was increased to 60 to ensure convergence. The TeraChem code[63][64][65] was used to carry out the ground and excited state electronic structure calculations. After each optimization, we performed a frequency calculation to ensure that the optimization algorithm reached a minimum. A Wigner sampling with 1000 geometries was carried out to obtain a set of initial conditions representative of the ground state. We sampled the initial conditions by running 1000 individual samplings in TeraChem, each with a different random number seed. To obtain a UV-Vis spectrum from the Wigner sampled structures, LR-TDDFT calculations, as specified above, were carried out on each sampled initial condition. The individual LR-TDDFT results were processed into one spectrum by applying a Gaussian broadening of 0.05 eV to the excitations grouped in bins of 0.005 eV windows.

VMD[66] was used throughout this thesis for creating the molecular representations used to illustrate structures from static calculations and dynamics simulations.

3.2 Adiabatic excited state dynamics

Both adiabatic dynamics on S_0 and S_1 were carried out using the electronic structure settings as stated above within the TeraChem code.

For the S_0 dynamics, one initial condition from the Wigner sampling was chosen as a starting point. A time step of 0.5 fs, a convergence threshold of $1.0{\cdot}10^{-6}$ Ha, and a two-electron integral threshold of $1.0{\cdot}10^{-14}$ Ha was applied. By setting the number of time steps to 20000, 10 ps of adiabatic ground state dynamics were simulated. For the S_1 adiabatic dynamics, the ground state minimum structure was chosen as initial condition while otherwise, the same settings as in the S_0 dynamics were applied.

To set a threshold for the hapticity parameter $\mathring{\alpha}$ (see section 4.2.4), the fluctuation around a mean hapticity, as extracted from the 10 ps of ground state dynamics, was taken. The mean $\mathring{\alpha}$ value from the S_0 dynamics is at 0.4998 with a standard deviation of 0.0225. By multiplying the standard deviation by three and subtracting the result from the mean hapticity one obtains the threshold of 0.4324 for $\bar{p}_i$. For $\bar{p}_i'$, an upper threshold of 0.5672 was used, such that all projection values within the interval [0.4324:0.5672] were considered as formally 0.5.

3.3 Nonadiabatic excited state dynamics

The nonadiabatic AIMS and AIMSWISS simulations were performed using the FMS90 code interfaced with TeraChem[67] using the same electronic structure settings as specified above. The simulations were started from the same initial condition as chosen for the S_0

dynamics. The dynamics simulations were started from the S_1 state, while including three excited singlet states. The time step was set to 20 atu and the TBF widths (α in eq. (28)) employed for H, C, and Ru were 4.5000, 22.5000, and 51.5926 bohr^{-2}[68], respectively. The coupling threshold one trajectory must exceed for entering the spawning mode was set to 0.0025, while the minimum population required for a trajectory to spawn was set to 0.01. As a coupling criterion, the nonadiabatic coupling vector projected onto the classic velocity (see eq. (41)) was used. The overlap maximum, which prevents trajectories from spawning new trajectories if the basis set becomes too redundant, was set to 0.6. The maximum energy difference under which couplings are still considered was set to 0.04 H. Applying these settings, 214 fs of Ruwich dynamics were covered with AIMS.

In the 5 separate AIMSWISS runs, where each covered 1400 fs, same input specifications as in the AIMS simulation were used. The time step in regions of strong couplings was set to 5 atu while the minimum adaptive time step was 0.001 atu.

As stated above, the AIMS dynamics was carried out for 214 fs, while 1400 fs were covered with AIMSWISS. This difference in simulation length arises because AIMS is more computationally demanding than AIMSWISS. In an AIMS simulation, the couplings between all TBFs spawned throughout the simulation are considered, while AIMSWISS applies a stochastic selection process that limits the number of TBFs (see section 2.5.3). The difference in computational demand can be highlighted when comparing the run time and number of electronic structure calls for AIMS and AIMSWISS. One AIMS run, covering 214 fs, took 24 days while a number of 52659 electronic structure calculations needed to be carried out. In comparison, one of the five AIMSWISS runs covering 1400 fs took on average seven days while requesting an average number of 12376 electronic structure calculations. Due to the high number of electronic structure calls made by AIMS and the high number of trajectories present in the last time steps, it was not feasible to let this simulation run for longer than 214 fs. The results from the AIMS simulation, giving a more accurate picture of the first 214 fs of Ruwich dynamics, shall be used as a reference for the ab initio molecular dynamics (AIMD) simulation on S_1 and the AIMSWISS simulation.

4 A rigorous definition of hapticity

As discussed in section 1.3, Cotton wanted to avoid any implications on the bond nature when coining the term hapticity. He thus developed a scheme only relying on topological features. However, he also gave no instructions on how hapticity should be determined based on the topology of a molecule. This ambiguity in the definition leads to complications when investigating processes where hapticity changes occur rapidly while also the geometry of the molecule changes. This complication is encountered for the excited state dynamics of organometallic complexes such as Ruwich. Therefore, much of the work carried out during this thesis focussed on obtaining a more rigorous definition of a geometry-based criterion, allowing for a determination of hapticity as unambiguously as possible.

This section will first explain the nomenclature of the Ruwich complex to later discuss the geometry descriptors applied in this thesis. Then, three different distance and angle-based parameters employed to describe changes in the geometry of the sandwich complex will be presented. Finally, two different approaches to define hapticity in sandwich complexes will be discussed. The second approach represents a further development of the first, highlighting the limitations of the first approach and the importance of included improvements.

4.1 Nomenclature of the complex

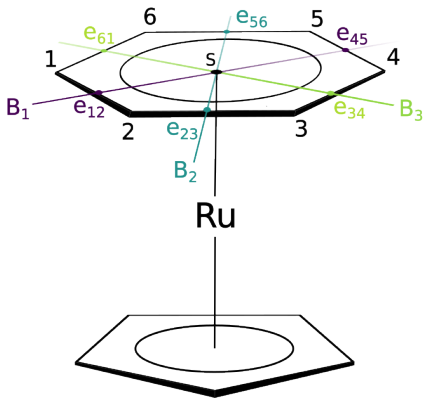

Figure 3: The numbering of C atoms in the Bz ring of Ruwich. The three bisection axes $\boldsymbol{B}_1$, $\boldsymbol{B}_2$, and $\boldsymbol{B}_3$ and the carbon bond midpoints e_{ij}, where i and j signify the number of the C atoms, as well as the Bz centroid S are shown.

Figure 3 provides an overview of the numbering of the six Bz carbon atoms in Ruwich and a depiction of the three bisection axes $\boldsymbol{B}_1$, $\boldsymbol{B}_2$, and $\boldsymbol{B}_3$ that will frequently be used in further analysis. The three bisection axes are constructed by taking the midpoint e_{ij} of two bound C atoms i and j and connecting this point to the midpoint of the opposing C-C bond. By for example connecting the two opposing midpoints e_{12} and e_{45}, the bisection vector $\boldsymbol{B}_1$ originating at e_{12} and pointing towards e_{45} is obtained. In an analogous way, $\boldsymbol{B}_2$ connects e_{23} and e_{56} while $\boldsymbol{B}_3$ is defined via e_{34} and e_{61} (see fig. 3). The three bisection axes are chosen as a frame of reference to describe the different positions of the Ru atom below the

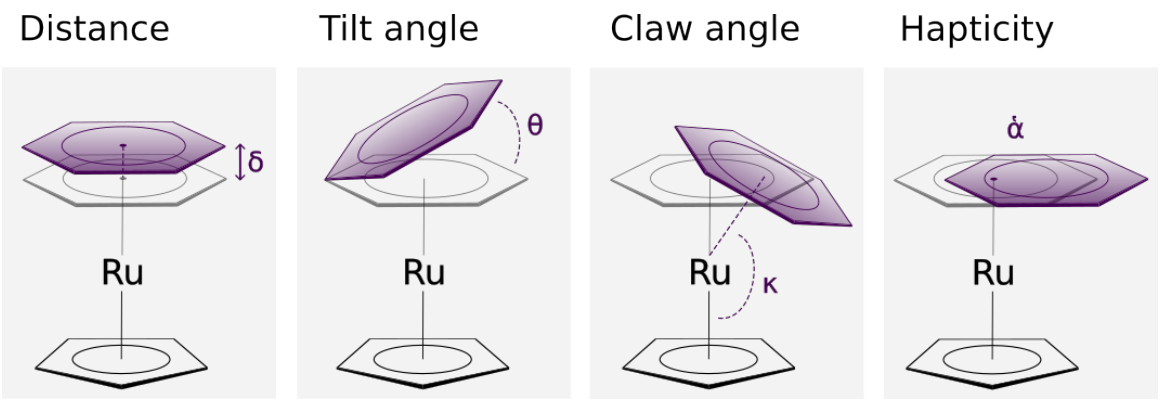

Figure 4: A pictorial explanation of the four parameters for the Ru-Bz distance (δ), the Bz tilt angle (θ), the claw angle (κ), and the Bz hapticity ($\dot{\alpha}$) used to classify geometrical changes of Ruwich. The geometrical change described by the respective parameter is indicated by a violet Bz ring.

Bz ring encountered during the dynamics simulations. The axes are used for computing the tilt angles θ of the Bz ring and to determine the hapticity as shall be highlighted at a later point. As long as the Bz hexagon is a regular hexagon, the three axes $\boldsymbol{B}_1$, $\boldsymbol{B}_2$, and $\boldsymbol{B}_3$ bisect the angle between two lines, each connecting two opposite C atoms. In addition, the three $\boldsymbol{B}_i$ axes meet in the centroid S of the Bz ring. The centroid S was chosen to evaluate the distance between Ru and Bz as shall also be discussed in the course of this chapter.

4.2 The four parameters describing geometric change in sandwich complexes

Figure 4 shows the four parameters used to analyze the geometry change of Ruwich during the excited state dynamics. The distance parameter δ, and the hapticity parameter $\dot{\alpha}$ both describe the position of a point in space relative to its position in the initial structure. The tilt and claw angles describe the angle between axes defined along the Ruwich structure. In the following the calculation, and meaning behind each of the four parameters shall be explained in more detail.

4.2.1 Distance

The distance parameter δ, depicted in the left-most panel of figure 4, describes the distance between the Ru atom and the centroid S of the Bz ring, calculated according to

$$S = \frac{\sum_{i=1}^{\nu} \boldsymbol{R}_i}{\nu} \tag{51}$$

where $\boldsymbol{R}_i$ depicts the coordinates of carbon atom i and ν corresponds to the number of atoms, equal to six for the Bz ring. Then, the distance between Ru and the centroid position S is determined. As a reference, the Ru-S distance of the starting structure is subtracted from the current Ru-S distance giving the δ value at each time step of a dynamics simulation. The δ value shows the change in Ru-Bz distance relative to the distance encountered

in the starting structure. δ can thus be seen as a first estimate and indication of bond weakening between Ru and Bz consequent to the photo-excitation.

4.2.2 Tilt angle

In order to describe the tilt angle of the Bz ring, the angle θ is used as depicted in the third panel in figure 4. θ describes the tilt of the Bz ring compared to the S_0 minimum geometry of the complex by computing the angle between each of the three current $\boldsymbol{B}$ axis and the normal vector of the Bz plane in the S_0 reference. One $\boldsymbol{B}$ axis specific θ_i value is calculated as

$$\theta_i = \arccos \frac{\boldsymbol{B}_i \cdot \boldsymbol{n}_{init}}{\|\boldsymbol{B}_i\| \cdot \|\boldsymbol{n}_{init}\|}, \tag{52}$$

where the normal vector $\boldsymbol{n}_{init}$ is obtained as the cross product of the $\boldsymbol{B}_1$ and $\boldsymbol{B}_2$ axes in the Ruwich ground state structure. A Kabsch alignment[69] between the current and the initial structure is carried out to cancel out any effects of rotation and translation in the calculation of the tilt angle θ. The θ_i values obtained according to equation (52) lie between 90° for a non-tilted Bz ring and 0° in the extreme case where the Bz ligand is perpendicular to its initial position. The three θ_i values are useful for determining which side of the Bz ring bends either upwards or downwards. This information, together with the distance parameter δ, gives a general overview on any changes the Bz ring undergoes during the dynamics.

4.2.3 Claw angle

The claw angle κ depicted in the left-most panel of figure 4 is used to describe the angle between the Bz and the Cp ligand. This angle, taking a value close to 180° for the Ruwich ground state structure, can help to detect whether the complex opens up at one side to potentially accommodate a new ligand. κ, defined with respect to the centroid S of Bz and the Cp ring centroid S_{Cp}, is computed according to

$$\kappa = \arccos \frac{\boldsymbol{RuS} \cdot \boldsymbol{RuS_{Cp}}}{\|\boldsymbol{RuS}\| \cdot \|\boldsymbol{RuS_{Cp}}\|} \,. \tag{53}$$

In equation (53), $\boldsymbol{RuS}$, and $\boldsymbol{RuS_{Cp}}$ signify the vectors connecting Ru to S, and to S_{Cp}, respectively.

For a Ruwich geometry with parallel Bz and Cp rings, the κ angle takes a value of 180° as the two centroids are in line with the Ru atom. The more Ruwich opens for coordination, that is to say, the more the Bz or Cp ring rotates around the Ru atom without altering its distance, the lower the κ angle becomes. This measure was also used in existing studies on geometry changes in organometallic catalysts to account for the possibility of coordination site openings.[32][33]

4.2.4 Hapticity

For the description of the Ru hapticity, three hapticity projection factors $\bar{p}_1$, $\bar{p}_2$, and $\bar{p}_3$ are defined with each corresponding to the respective $\boldsymbol{B}_i$ axis. The three $\boldsymbol{B}_i$ axes are obtained

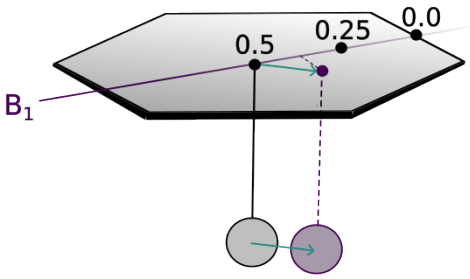

Figure 5: The calculation of the scalar projection value $\bar{p}'_1$ with respect to the bisection axis $\boldsymbol{B}_1$. Numbers are given to indicate positions on the $\boldsymbol{B}_1$ axis that lead to the respective projection values. The violet sphere indicates a potential Ru displacement from the equilibrium position (grey sphere) that leads to a $\bar{p}_1$ value between 0.50 and 0.33. The turquoise arrows highlight the effect of the Ru translation on the scalar projection factor.

as described in section 4.1. The $\boldsymbol{B}_i$ axes were chosen as a frame of reference axes to obtain hapticity parameters as they are thought to represent primary axes of Ru movement during a hapticity change from η^6 to η^4. The scalar projection p'_i

$$p'_i = \hat{\boldsymbol{B}}_i \cdot \boldsymbol{e_{ij}Ru}, \tag{54}$$

between one of the three normalized $\boldsymbol{B}_i$ vectors and the vector $\boldsymbol{e_{ij}Ru}$ connecting the Ru atom and the midpoint e_{ij} (see fig. 3) that defines the origin of $\boldsymbol{B}_i$ is taken to get a measure of the Ru position with respect to the axis $\boldsymbol{B}_i$. This projection p_i, being a measure of the Ru atom position with respect to the $\boldsymbol{B}_i$ axis, is divided by the length of the respective $\boldsymbol{B}$ vector to obtain the normalized projection factor $\bar{p}'_i$. The value of $\bar{p}'_i$ can range between 0.0, when Ru is located below the origin of $\boldsymbol{B}_i$, and 1.0 for a Ru position below the end point of $\boldsymbol{B}_i$. If Ru is located below the centre of the $\boldsymbol{B}_i$ axis, which corresponds to the centroid S as long as the Bz ring is planar and symmetric, the corresponding $\bar{p}'_i$ value lies at 0.5 (see fig. 5). As Ruwich is symmetric, it is assumed that rearrangement processes taking place at different halves of the Bz hexagon are equivalent. This assumption suggests a projection value interval that ranges between 0.0 and 0.5. Therefore, the $\bar{p}_i$ projection values within a [0.0,0.5] interval are obtained via

$$\bar{p}_i = \begin{cases} \bar{p}'_i & \text{for } \bar{p}'_i \leq 0.5 \\ 0.5 - (\bar{p}'_i - 0.5) & \text{for } \bar{p}'_i > 0.5\ . \end{cases} \tag{55}$$

A graphical description of the $\bar{p}'_i$ projection parameter is given in figure 5, where two different positions of Ru below the Bz ring are indicated by using spheres of different colors.

The first approach to define hapticity via the three $\bar{p}_i$ projection values was based on the graphical deliberations presented in figure 5. In a hapticity change from η^6 to η^4 the Ru atom is translated along one of the three $\boldsymbol{B}_i$ axes. Hereby, Ru approaches two C atoms while increasing its distance to the two lying opposite to its direction of movement. As

a hapticity change to η^4 was priorly thought to be most common in the excited state dynamics of Ruwich the hapticity parameters $\bar{p}_i$ were computed with respect to a frame of reference well reflecting the movement that Ru undergoes in this process. Any arbitrary Ru translation that cannot be represented by one $\boldsymbol{B}_i$ axis alone is characterized by the set of three $\bar{p}_i$ values. In figure 5, a turquoise arrow connects an arbitrarily translated Ru atom indicated by a violet sphere to its initial position represented by a grey sphere. The translation causes the $\bar{p}_1$ value to be lowered to a value between 0.5 and 0.25 as indicated by the turquoise arrow depicted on the grey-shaded Bz surface. However, only the $\bar{p}_1$ value alone does not suffice to determine the Ru position as Ru could be located anywhere below the axis perpendicular to $\boldsymbol{B}_1$ and intersecting $\boldsymbol{B}_1$ at the value of $\bar{p}_1$. Consequently, the three projection values need to be combined to give an accurate description of all possible Ruwich structures. To this extent, the projection factors corresponding to ideal versions of the hapticities from one to six presented in table 1 were determined.

Hapticity	$\bar{p}_1$	$\bar{p}_2$	$\bar{p}_3$
η^1	0.00	0.00	0.50
η^2	0.00	0.25	0.25
η^3	0.25	0.25	0.50
η^4	0.25	0.33	0.33
η^5	0.33	0.33	0.50
η^6	0.50	0.50	0.50

Table 1: The resulting η value for possible combinations of the three hapticity projection factors $\bar{p}_1$, $\bar{p}_2$, and $\bar{p}_3$. For each hapticity only one of the six symmetry equivalent projection factor combinations is given.

When first examining the $\bar{p}_i$ combinations in table 1, one can see that only for a η^6 hapticity, all projection values are equal to 0.5. In all other hapticity cases, at least two of the three $\bar{p}_i$ values are lower than 0.5. When two of the three projection factors decrease while the third one remains at 0.50 the Ru atom is translated along one of the axes connecting opposing C atoms. This Ru movement leads to a hapticity of 5 for lower distances covered (indicated by $\bar{p}_i$ values of 0.33 for η^5 in table 1) and to a hapticity of 3 in cases where the Ru movement shows higher extent ($\bar{p}_i$ values of 0.25 for η^3 in table 1). In a case of extreme translation, Ru terminates its movement below one of the C atoms leading to a hapticity of 1 and two $\bar{p}_i$ equal to 0.00. From this deliberation, it can be seen that all odd hapticities are caused by Ru translations along an axis connecting two opposing C atoms. For the even hapticities of 4 and 2, the Ru displacement occurs along one of the $\boldsymbol{B}_i$ axes as already discussed in section 4.1. Due to the displacement along one $\boldsymbol{B}_i$ axis, the corresponding $\bar{p}_i$ value decreases to a higher extent than the other two $\bar{p}_i$ values as indicated by the $\bar{p}_1$ value of 0.25, and the $\bar{p}_2$, $\bar{p}_3$ values of 0.25 for η^4 (see table 1). For η^2, the displacement along one B_i axis is more pronounced, leading to the $\bar{p}_i$ values of 0.00 and 0.25 presented in table 1.

In order to avoid the ambiguity of having to rely on too many thresholds as presented for the different hapticities in table 1 a more flexible definition of hapticity was developed. This approach only focuses on the question of whether a $\bar{p}_i$ value is equal to or below 0.5 and can thereby distinguish between the three hapticities of 6, 4, and 3. Note that this

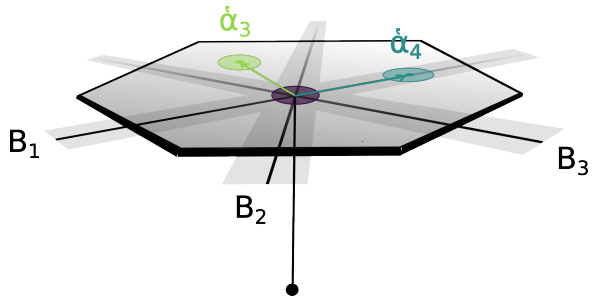

Figure 6: A pictorial explanation of the determination of the ἁ parameter. The grey areas around the $\boldsymbol{B}_i$ axes indicate the threshold-based classification of $\bar{p}_i$ values either within or outside the 0.5 window. The lime circle indicates a possible $\dot{\alpha}_4$ position while the turquoise circle exemplifies a $\dot{\alpha}_3$ position of Ru below the Bz ring.

scheme could in principle be extended to also include hapticities of 2 and 1, by additionally asking if any of the $\bar{p}_i$ values is equal to 0, but as these hapticities were thought to be a rare occurrence the corresponding cases were omitted. Equally, the concept could be extended to being able to distinguish between hapticities of 3 and 5 but a η^5 coordination was thought to not vary from η^6 substantially enough to be detectable in rapid hapticity fluctuation processes. To arrive at a total hapticity value starting from the three projection factors $\bar{p}_1$, $\bar{p}_2$, and $\bar{p}_3$ while distinguishing between the three cases $\dot{\alpha}_6$, $\dot{\alpha}_4$, and $\dot{\alpha}_3$ it suffices to ask whether all, none, or one $\bar{p}_i$ value is equal to 0.5. This distinction can be achieved via

$$\dot{\alpha} = \begin{cases} \dot{\alpha}_6 & \text{for } \bar{p}_i, \bar{p}_j, \bar{p}_k = 0.5 \\ \dot{\alpha}_4 & \text{for } \bar{p}_i, \bar{p}_j, \bar{p}_k < 0.5 \\ \dot{\alpha}_3 & \text{for } \bar{p}_i = 0.5 \wedge \bar{p}_j, \bar{p}_k < 0.5 \end{cases} \tag{56}$$

where the letter ἁ is used to clearly distinguish from the η value introduced by Cotton as the latter is assigned without using an underlying geometry-based definition. ἁ was the letter of choice as the Greek word ἅπτο that the term hapticity is derived from starts with the letter α. The ῾ accent was used in ancient Greek to indicate the 'h' sound is preserved to avoid confusion with any other property abbreviated by α.

A graphical overview is provided in figure 6 to facilitate the understanding of assigning the three hapticity values $\dot{\alpha}_6$, $\dot{\alpha}_4$, and $\dot{\alpha}_3$. From focussing on figure 6, it can be gathered that a hapticity of $\dot{\alpha}_6$ is only possible all projection factors are equal 0.5 as this distribution of $\bar{p}_i$ values naturally arises if Ru is below the centroid. Accounting for the fluctuations of Ru around the centroid that is observable in the ground state due to thermal fluctuations requires considering an interval around 0.5 instead of the fixed value. The exact determination of this interval will be discussed in section 6.1 in connection to the adiabatic ground state dynamics of Ruwich. When considering an interval one arrives at a hapticity of $\dot{\alpha}_6$ whenever all projection values lie within the threshold, as indicated by the violet circle in figure 6. As aforementioned, a conformation leading to the α_4 case can only be realized if the Ru atom is translated along one of the three $\boldsymbol{B}_i$ axes causing all three $\bar{p}_i$ values to drop below 0.5. When again considering a threshold-based interval instead of a sharp number, each conformation showing Ru to be positioned below one of the grey rectangles

surrounding the three $\boldsymbol{B}_i$ axes in figure 6 is classified as $\mathring{\alpha}_4$. The turquoise arrow connecting the centroid with the blue circle signifies a possible Ru translation leading to a $\mathring{\alpha}_4$ geometry where Ru is located below the threshold-defined area indicated by the turquoise circle. In the case of α_3, the Ru translation is carried out along one of the axes connecting two opposing C atoms. When Ru follows one of these axes, its projection factor remains within the interval around 0.5 for exactly one $\boldsymbol{B}_i$ axis while the two other projection factors decrease. The corresponding Ru translation is again indicated in figure 6 by the lime-colored arrow connecting the centroid and the lime sphere which indicates a possible Ru position for a $\mathring{\alpha}_3$ coordination.

If one had chosen the three axes connecting opposing C atoms as a reference frame for hapticity determination instead of the $\boldsymbol{B}_i$ axes, again, three distinguishing cases would arise. Within these cases, the rules for $\mathring{\alpha}_4$ and $\mathring{\alpha}_3$ would be exchanged. It is in principle also possible to detect cases of $\mathring{\alpha}_2$ and $\mathring{\alpha}_1$ using the $\boldsymbol{B}_i$ axes, but as these hapticities are not likely to occur within the example considered, a discussion of the corresponding rules is left aside.

4.3 Summary on the definition of hapticity

In summary, it can be stated that the $\mathring{\alpha}$ criterion applied to distinguish between different hapticities allows for an unambiguous determination of hapticity as a certain combination of projection values will always lead to only one $\mathring{\alpha}$ value. The $\mathring{\alpha}$ criterion conveniently applies only one, uniformly valid threshold that is based on a rationale, namely the Ru fluctuation around the equilibrium position observed in the ground state. The usage of $\mathring{\alpha}$ thus avoids the determination of distance thresholds the six Ru-C distances could be evaluated after, a procedure less straightforward to carry out. A mere distance-based criterion would also cause the complication of whether all distances within the threshold should be considered as bonds, although no information on the Ru orientation towards the Bz ring is taken into account. As a separate measure for the Ru-Bz distance is more easily available in the form of e.g. the δ parameter, having a projection-based hapticity measure independent of distances is additionally beneficial. Throughout this thesis, the $\mathring{\alpha}$ parameter will be determined for all dynamics simulations and investigated with regard to its validity. It will be shown that the parameter correctly distinguishes between different hapticities while, when being deconstructed into the contributing projection factors, still allowing for more detailed quantification of the Ru position below the Bz ring.

In addition to the previously described parameters, δ, θ, κ, and $\mathring{\alpha}$ the six dihedral angles in the Bz ring of Ruwich were examined. The dihedral angles, describing a tilt in the ring structure itself, combined with the information from the four parameters of figure 4 offer the possibility to detect whether a change in hapticity is provoked by a tilt of the ring itself (change in dihedrals) or by a change of the Bz orientation relative to the complex (change of any or a combination of the four parameters). Including the dihedral angles in the description of Ru movements will also serve to determine whether the $\mathring{\alpha}$ parameter still reliably distinguishes between hapticities if Bz is far from its initial planar structure.

Taking all four geometry parameters together will hopefully prove to provide a good overall understanding of the movement undergone by the Bz ligand in Ruwich after photoexcitation. Potentially, the combined information from several parameters will help to discover how a significant change in one geometric parameter influences the remaining

parameters. This insight might help to obtain a generalizable quantification for the flexible movement of a cyclic π ligand in the excited state. Such a quantification scheme could prove helpful for studying and predicting trends in ligand fluctuations that enable reactivities of other ligands, or the opening of a new coordination side. Therefore, a scheme, useful for understanding and tuning catalytic reactions applying sandwich complexes, could be obtained by combining the information yielded by the four geometry parameters.

5 Benchmarking the electronic structure methods to describe the ground and excited electronic states of Ruwich

Before being able to carry out dynamics simulations on Ruwich, finding an electronic structure method capable of describing the complex represents a crucial step. To do so, C-Ru distances and the Bz and Cp bond lengths and dihedral angles obtained from different DFT functionals and basis sets were compared to a Ruwich crystal structure[70]. The nuclear ensemble approach[71] was used to predict the UV-Vis spectrum of Ruwich to assess the capability of LR-TDDFT in describing the excited electronic states of this complex. The so obtained spectrum was compared to the experimental result[72]. In addition, geodesic interpolation scans[46] connecting the ground state minimum to the Franck-Condon (FC) S_1 minimum as well as linear scans over Ruwich structures of hapticity values from two to six were performed. These two types of scans were carried out to explore the regions surrounding the S_0 and S_1 minima via static calculations to obtain a first understanding of the Ruwich dynamics. The hapticity scans also served to investigate the response of the Ruwich electronic structure to static changes of hapticity.

5.1 Geometry optimization of the S_0 and S_1 states

By carrying out geometry optimizations on a Ruwich guess structure and comparing bond lengths and dihedrals in the Cp, and Bz ligand as well as Ru-C distances to the corresponding data from the crystal structure[70] the performance of different functionals in describing the electronic interactions in Ruwich was evaluated. The geometrical properties obtained from the functionals PBE[73][74], PBE0, B3LYP, and ωB97XD as well as the experimental reference values can be found in table 2.

When focussing on the distances between the Bz C atoms and Ru presented in table 2, it can be stated that all computational results lie around 2.23 Å. Therefore, the computationally obtained structures show higher Bz-Ru distances than the crystal structure with 2.17 Å. This finding might arise because all functionals underestimate the interaction between Bz and Ru, leading to an artificial increase in the respective metal-ligand distance.

Regarding the distances between Ru and the Cp C atoms, which lie at around 2.19 Å for all functionals, it can be observed that lower distances were obtained than the value of around 2.21 Å measured in the crystal structure. This behavior, opposing the observation for the Ru-Bz C atom distances, indicates that all functionals overestimate the stabilization due to an interaction between the positively charged Ru atom and the negatively charged Cp ligand. From these two observations, it can be gathered that all considered functionals overestimate the stabilization due to ionic interactions to a comparable extent while they underestimate the beneficial character of coordinative bonding. However, one should note that the crystal structure used for comparison accurately reflects the geometric properties of Ruwich in a solid bulk phase, but not of a single Ruwich molecule in gas phase. Therefore, systematic deviations in the computed structures should not be regarded as too problematic.

Considering the C-C distances encountered for Bz and Cp it can be observed that all bond lengths vary only slightly between different functionals and are always slightly higher for the crystal structure. Overall, the differences in C-C distances that are shown for the examined functionals do not justify any favor towards or decision against any of the ap-

Property	PBE	PBE0	B3LYP	ωB97XD	Exp
Dist. [Å]					
Ru-Bz	2.24	2.23	2.27	2.23	2.19
	2.24	2.23	2.27	2.23	2.17
	2.25	2.23	2.27	2.23	2.16
	2.24	2.24	2.28	2.23	2.17
	2.24	2.23	2.28	2.23	2.19
	2.24	2.23	2.27	2.23	2.17
Ru-Cp	2.21	2.19	2.23	2.19	2.22
	2.21	2.19	2.23	2.20	2.21
	2.21	2.20	2.22	2.20	2.19
	2.21	2.19	2.22	2.19	2.20
	2.21	2.19	2.23	2.19	2.22
C-C Bz	1.43	1.42	1.42	1.42	1.39
	1.43	1.42	1.42	1.42	1.39
	1.43	1.42	1.42	1.42	1.40
	1.43	1.42	1.42	1.42	1.39
	1.43	1.42	1.42	1.42	1.39
	1.43	1.42	1.42	1.42	1.39
C-C Cp	1.44	1.43	1.43	1.43	1.42
	1.44	1.43	1.43	1.43	1.42
	1.44	1.43	1.43	1.43	1.42
	1.44	1.43	1.43	1.43	1.42
	1.44	1.43	1.43	1.43	1.42
Dihed. [°]					
Bz	0.122	0.156	0.150	0.127	0.274
	0.167	0.100	0.168	0.015	0.226
	0.254	0.043	0.180	0.040	0.227
	0.296	0.042	0.174	0.078	0.274
	0.252	0.097	0.156	0.221	0.320
	0.165	0.154	0.144	0.245	0.321
Avg.	0.209	0.099	0.162	0.121	0.274
Cp	0.060	0.281	0.048	0.072	0.329
	0.012	0.225	0.065	0.108	0.225
	0.041	0.084	0.058	0.103	0.035
	0.078	0.090	0.029	0.059	0.168
	0.085	0.229	0.012	0.008	0.307
Avg.	0.055	0.182	0.042	0.070	0.213

Table 2: The key distances and angles in Ruwich obtained from different functionals compared to the crystal structure in ref. [70]. The basis set aug-cc-pVDZ was used in combination with a LANL2DZ effective core potential for Ru.

proaches. The dihedral angles for the optimized structures are in all cases lower than observed experimentally, indicating that the Bz and Cp rings are more planar in the com-

Property	PBE0			ωB97XD			Exp
	cc-pVDZ	aug-cc-pVDZ	cc-pVTZ	cc-pVDZ	aug-cc-pVDZ	cc-pVTZ	
Dist. [Å]							
Ru-Bz	2.24	2.23	2.23	2.24	2.23	2.23	2.19
	2.24	2.23	2.23	2.24	2.23	2.23	2.17
	2.23	2.23	2.23	2.24	2.23	2.23	2.16
	2.23	2.24	2.22	2.24	2.23	2.23	2.17
	2.24	2.23	2.22	2.24	2.23	2.23	2.19
	2.24	2.23	2.23	2.24	2.23	2.23	2.17
Ru-Cp	2.19	2.19	2.19	2.19	2.19	2.19	2.22
	2.19	2.19	2.19	2.19	2.19	2.19	2.21
	2.19	2.20	2.19	2.19	2.20	2.19	2.19
	2.19	2.19	2.19	2.19	2.20	2.19	2.20
	2.19	2.19	2.19	2.19	2.19	2.19	2.22
C-C Bz	1.42	1.42	1.41	1.42	1.42	1.41	1.39
	1.42	1.42	1.41	1.42	1.42	1.41	1.39
	1.42	1.42	1.41	1.42	1.42	1.41	1.39
	1.42	1.42	1.41	1.42	1.42	1.41	1.39
	1.42	1.42	1.41	1.42	1.42	1.41	1.39
	1.42	1.42	1.41	1.42	1.42	1.41	1.40
C-C Cp	1.43	1.43	1.42	1.43	1.43	1.42	1.42
	1.43	1.43	1.42	1.43	1.43	1.42	1.42
	1.43	1.43	1.42	1.43	1.43	1.42	1.42
	1.43	1.43	1.42	1.43	1.43	1.42	1.42
	1.43	1.43	1.42	1.43	1.43	1.42	1.42
Dihed. [°]							
Bz	0.239	0.156	0.039	0.056	0.127	0.076	0.274
	0.205	0.100	0.068	0.216	0.015	0.002	0.226
	0.172	0.043	0.194	0.279	0.040	0.005	0.227
	0.171	0.042	0.292	0.184	0.078	0.082	0.274
	0.204	0.097	0.263	0.024	0.221	0.156	0.320
	0.238	0.154	0.137	0.040	0.245	0.153	0.321
Avg.	0.205	0.099	0.166	0.133	0.121	0.079	0.274
Cp	0.066	0.281	0.034	0.097	0.072	0.053	0.329
	0.064	0.225	0.017	0.045	0.108	0.003	0.225
	0.037	0.084	0.007	0.024	0.103	0.058	0.035
	0.003	0.090	0.028	0.084	0.059	0.089	0.168
	0.042	0.229	0.038	0.112	0.008	0.091	0.307
Avg.	0.042	0.182	0.025	0.072	0.070	0.059	0.213

Table 3: The key distances and angles in Ruwich obtained from different basis sets when using the functionals ωB97XD and PBE0 compared to the crystal structure in ref. [70]. A LANL2DZ effective core potential was used for Ru.

puted structures than in the crystal structure. This finding might hint at the DFT methods overestimating the aromatic character of the two rings. But again, as the difference between the computational structures and the experimental structure are only minor, they can also be caused by the difference in phase environment.

As a correct description of the Ru-Bz interaction is crucial to the project at hand, it is reasonable to base the choice of functional mostly on the Ru-Bz distances rather than on the Ru-Cp distances or any other of the geometrical parameters. Based on the geometric properties presented in table 2 the choice of functional falls in favor of PBE0 and ωB97XD as both show the lowest Ru-Bz distance of 2.23 Å.

After highlighting the performance of ωB97XD and PBE0 in describing the ground state geometry of Ruwich we now turn to investigating the influence of the basis set on our calculations. Hereby, we focused on testing the impact of basis set change on the C and H atoms, while the effective core potential used for Ru was kept at the LANL2DZ basis set. The geometric parameters under examination presented in table 3 are equivalent to the benchmarking parameters used for the functionals. Three types of basis sets cc-pVDZ, cc-pVTZ[75], and aug-cc-pVDZ were tested. As can be seen when focusing on table 3, all basis sets yielded similar Ru-C distances and C-C bond lengths. The changes in average dihedral angles were also not substantial. We thus concluded that a basis set change has only minor impact on the functional's performance in describing Ruwich and decided to choose the computationally least demanding basis set. The computational cost is an especially important aspect regarding the aim to carry out dynamics simulations on Ruwich. Therefore, cc-pVDZ, being the smallest basis set among the three, was used in all following calculations.

5.2 Predicting the UV-Vis absorption spectrum of Ruwich

In figure 7, the experimentally obtained UV-Vis spectrum of Ruwich is compared to the simulated spectra obtained with ωB97XD and PBE0 using the nuclear ensemble aproach with 1000 Wigner sampled geometries. Both simulated spectra were obtained from LR-TDDFT calculations on 1000 Wigner structures including the first four excited singlet states. In this and all following calculations, no triplet states were considered to first focus on the description of singlet states an population transfer between them.

One can deduce from figure 7 that ωB97XD gives an excitation maximum of 321 nm closely matching the experimental peak at 320 nm[72] while PBE0 shifts the excitation peak towards a lower wavelength of 315 nm. Both functionals yield a similar photo-absorption cross-section σ for the excitation peak with a value of $5.49{\cdot}10^{-19}$ cm^{2}molecule^{-1} for ωB97XD and $5.47{\cdot}10^{-19}$ cm^{2}molecule^{-1} for PBE0 at their respective maximum. The experimental value for the extinction coefficient ϵ of 136 M^{-1}cm^{-1} can be transformed into a photo-absorption cross section via

$$\sigma = \frac{ln(10) \cdot 10^3}{N_A} \cdot \epsilon \, . \tag{57}$$

According to equation (57) the experimentally observed ϵ at 320 nm correspond to a σ value of $5.22{\cdot}10^{-19}$ cm^{2}molecule^{-1} which is in good agreement with the computationally obtained absorption intensity. From this satisfying agreement between the experimental

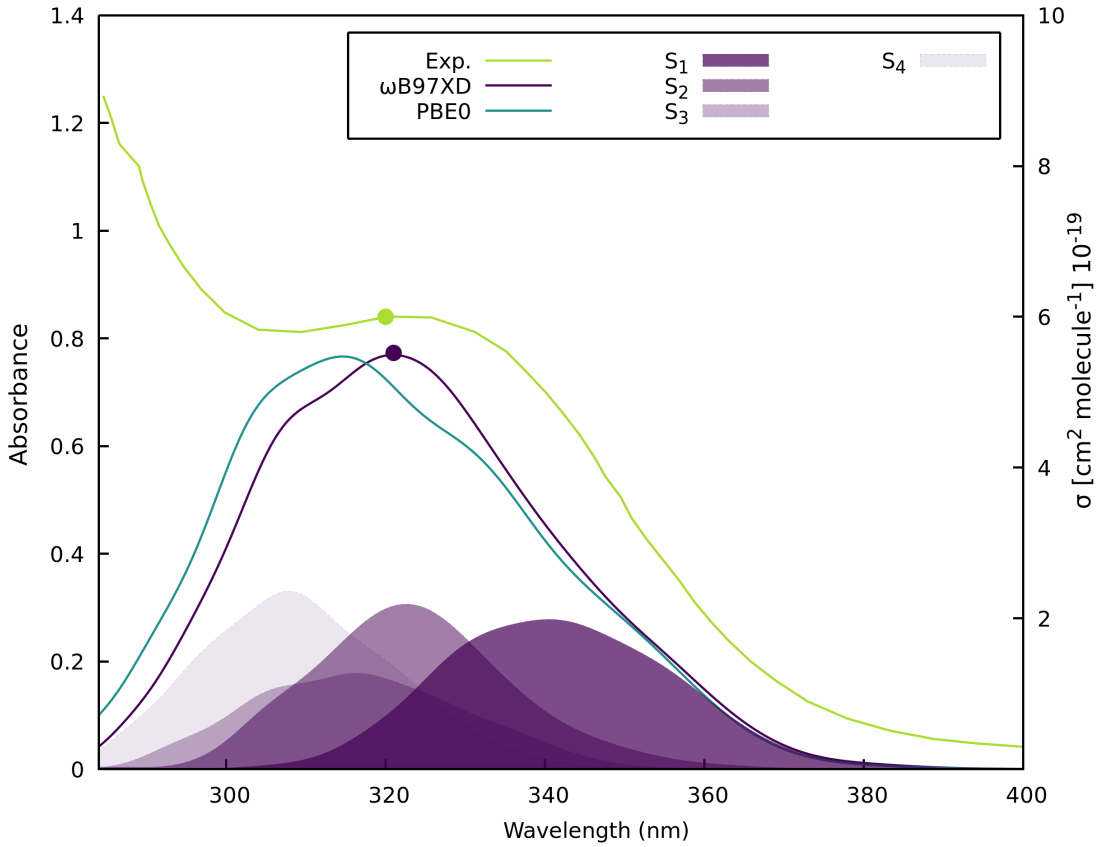

Figure 7: Theoretical and experimental UV-Vis spectrum of Ruwich. The experimental spectrum[72] is shown in lime while the dot indicates the absorption maximum of 136 mol^{-1} cm^{-1} at 320 nm reported by Mann et al. The computational spectra obtained from LR-TDDFT include four excited states on 1000 Wigner sampled structures. The ωB97XD spectrum is shown in violet and PBE0 is presented in turquoise. For ωB97XD, the S_1 to S_4 contributions are shown as violet areas of decreasing opacity. The photo-absorption cross-section for ωB97XD at the maximum of 321 nm is indicated by a violet dot. The calculated spectra were obtained using Gaussian broadening with a broadening parameter of 0.05 eV and an energy bin width of 0.005 eV.

and the computational approach, one can gather that the electronic structure method of choice describes excitation processes in Ruwich around the ground state geometry with reasonable accuracy.

When further examining the individual contributions from the four excited states to the broadened ωB97XD spectrum it can be observed that the second lowest transition has its maximum at the position matching the overall maximum of the spectrum. From figure 8, one can see that the second transition corresponds to an electron transferred from the d_{z^2} orbital, bonding towards Ru and Bz, to the two-degenerate $d_{xz,yz}$ orbital which is anti-bonding towards Ru and Bz. At this point, we want to emphasize that the strongest

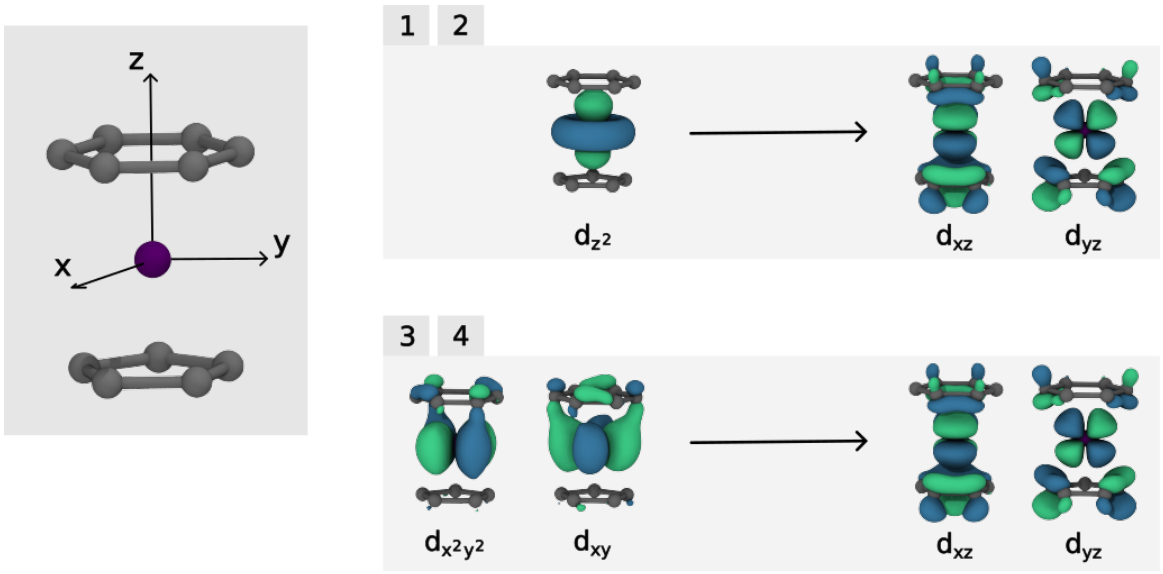

Figure 8: The molecular orbitals of Ruwich participating in the four lowest singlet excitations, obtained with ωB97XD, cc-pVDZ, and the LANL2DZ effective core potential for Ruwich. The Ruwich molecule in a cartesian coordinate frame is given as a reference for the orbital nomenclature.

contribution to the UV-Vis spectrum of Ruwich is an excitation targeting a molecular orbital hindering the Ru and Bz interaction. The peak of the first transition lies at a longer wavelength of 340 nm, while the third and fourth transitions are located at 316 nm and 308 nm, respectively. The first transition is thus responsible for the tail in the total spectrum towards longer wavelengths while the S_4 transition causes a shoulder in the total spectrum around its absorption maximum at 308 nm. In the experimental spectrum, no shoulder is observed in the respective wavelength region but rather a shallow decrease in absorption until the intensity rises significantly after 300 nm. The character of the first transition, presented in figure 8, is equivalent to the character of the brightest second transition. The third and fourth transitions both involve the two-degenerate π-back bonding molecular orbitals $d_{x^2y^2,xy}$ as a donor and again target the antibonding $d_{xz,yz}$ orbitals. From predicting the UV-Vis absorption spectrum of Ruwich we thus confirmed that the four lowest singlet transitions all destabilize the Ru-Bz coordinative bond. Furthermore, the S_1 to S_4 transitions are all centred around the Ru metal atom and do not show significant charge transfer character to any of the ligands.

To summarize, the nuclear ensemble approach combined with LR-TDDFT and the ωB97XD functional predict the Ruwich UV-Vis spectrum in good agreement with the experiment. Not only do the wavelengths of the absorption maximum, but also the respective absorption intensities agree well, showing that ωB97XD accurately describes excitation processes for the Ruwich complex in equilibrium.

5.3 Geodesic interpolation between the S_0 and S_1 minimum

In order to get a better understanding of the potential region connecting the S_0 minimum and the S_1 minimum, a geodesic interpolation[46] between the two structures was carried out using 17 interpolated geometries. The S_0 and S_1 minimum structures obtained with ωB97XD are shown as inlets in the left panel of figure 9. The energy of the first four excited states was then calculated on support of these structures. Two different geodesic interpolations were performed using the functionals ωB97XD and PBE0 as presented in figure 9. With regard to the interpolations, it can be stated that in both cases the first four excited states, S_1 to S_4, lie close in energy. The ωB97XD interpolation shows that all four states are within 1 eV throughout the entire interpolation from the FC region to the S_1 minimum. In the PBE0 interpolation, the first four excited states diverge more in energy as an energy range above 1 eV can be observed at the FC minimum geometry. Overall, the fact that the S_1 to S_4 states are energetically close matches the expectation of encountering nearly degenerate excited states in transition metal complexes. This circumstance furthermore implies that many interaction processes will take place between different singlet states as soon as Ruwich is excited.

When further focusing on the interpolations it can be observed that the states S_2, S_3, and S_4 come very close in energy around the interpolated structure 4 for both functionals. For ωB97XD, a degeneracy can be observed between these three states while PBE0 again shows larger energy gaps. After structure 4, the S_1, S_2, and S_3 states become closer in energy for ωB97XD while the S_4 state shows a continuously growing energy deviation. For PBE0 the energy gaps between all states increase such that no near-degeneracy between particular states is observable anymore after the interpolated structure 12.

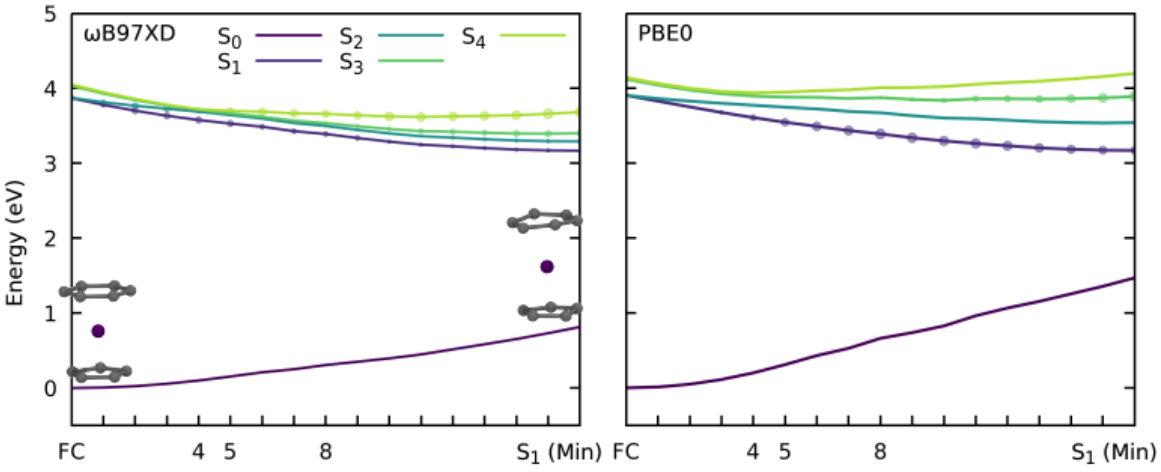

Figure 9: Geodesic interpolation[46] from the S_0 minimum structure (FC region) to the S_1 minimum using ωB97XD (left panel) and PBE0 (right panel). The interpolation was performed with 17 frames, including the start and end structures. Four excited states were included in the LR-TDDFT calculations. Spheres on the energy curves indicate the oscillator strength of transitions from S_0 with size varying proportionally.

The LR-TDDFT transitions of each frame were analyzed and compared to investigate

the character of the transitions occurring for the frames of the interpolation. Hereby, the focus lied on the analysis of the ωB97XD transitions, as this functional was shown in section 5.2 to yield a more accurate description of the excited state energies and transitions. The oscillator strength of the transitions is indicated in figure 9 by using spheres sized in proportion to this quantity. For the first four frames, ωB97XD yields similar excitation characters as around the ground state equilibrium presented in figure 8 and discussed in section 5.2. The first and second transitions occur between the bonding d_{z^2} orbital and the two-degenerate $d_{xz,yz}$ orbital, which is antibonding with respect to the Bz-Ru and Cp-Ru bonds. The third and fourth transitions correspond to excitations from the two-degenerate π back bonding $d_{x^2y^2,xy}$ orbitals lying in the plane parallel to the Bz and Cp rings again to the two-degenerate $d_{xz,yz}$ antibonding orbitals. The excitation energies start to decrease as from the beginning of the scan onwards, the excited state energies decrease while the S_0 energy increases. At the fourth interpolated structure, the first transition still occurs between the d_{z^2} bonding orbital and the two-degenerate $d_{xz,yz}$ antibonding orbital. However, the second transition changes to an excitation from the $d_{x^2y^2,xy}$ π back bonding orbital to the antibonding $d_{xz,yz}$ orbital and does thus no longer involve the binding d_{z^2} orbital. The third and fourth transitions do not change character but increase their oscillator strengths from both 0.0000 to 0.0001 and 0.0003, respectively, indicating that geometrical changes in Ruwich cause these transitions to now be allowed. At the interpolation structure 5, the fourth transition changes character to now occur between the bonding d_{z^2} orbital and the antibonding $d_{xz,yz}$ orbital. From the character changes taking place from the FC to the interpolated structure 5, one can generally gather that the d_{z^2} to $d_{xz,yz}$ transition increases in energy while the energy required for the $d_{x^2y^2,xy}$ to $d_{xz,yz}$ transition is lowered. Furthermore, the states S_3 and S_4 which are degenerate for the first four frames of the interpolation diverge in energy after the fifth interpolation structure while the states S_2 and S_3 become closer in energy as they now share the excitation character. At the interpolation structure 8, the character of the first transition also changes from the d_{z^2} orbital to the $d_{x^2y^2,xy}$ being the electron donating orbital while the third transition changes to a d_{z^2} to $d_{xz,yz}$ excitation. From structure 8 until the last interpolated structure 16, the S_1 minimum structure, the character of the states S_1 to S_4 doesn't undergo any further change while the degeneracy between states S_2 and S_3 is slightly reduced. In addition, the excitation energies show further decrease until frame 16 owed to an increase in the S_0 energy by a total amount of almost 1 eV accompanied by a lowering in energy for the excited states.

To summarize the change of excitation energies and characters observed in the geodesic interpolation between the FC region and the S_1 minimum obtained with ωB97XD it can be stated that the excitation character is opposed between the start and end of the interpolation. As this opposition occurs between the interpolated structures 0 and 8, it can be stated that the character exchange occurs closer to the FC region while the excitation characters remain more constant in the region around the S_1 minimum. Regarding the change in excitation character, one should bear in mind that only the character of the donating orbital changes. The character of the acceptor orbital remains antibonding with respect to the Ru-Bz bond throughout the entire interpolation. This finding indicates that at least in the FC and the S_1 minimum region the four lowest excitations lead to a destabilization of the Ru-Bz bond. Excitations on corresponding Ruwich structures are thus suspected to cause hapticity fluctuations comparable to the slip distortions for complexes exceeding the 18 electron rule[20].

5.4 Hapticity scans

Linear scans between structures of different hapticity are shown in figure 10 for the S_0 minimum structure and a modified S_0 structure, where the Ru-Bz and the Ru-Cp distances are increased to the values obtained for the S_1 minimum structure. Structures of different hapticity were obtained by setting the projection value $\bar{p}_1'$ (see section 4.2.4) that is defined to lie in an interval of [0.0,1.0] to values between 0.0 (η^2) and 1.0 (again η^2) while using a step size of 0.05. In this way, a total of 20 structures were generated for each hapticity scan. The structures with a $\bar{p}_1$ value of 0.25 and 0.75 were considered to be η^4 while the $\bar{p}_1$=0.5 geometry corresponds to the ground state structure of η^6 (see fig. 5). The linear hapticity scan corresponds to a translation of the Ru and Cp fragment along the $\boldsymbol{B}_1$ axis of the Bz ring.

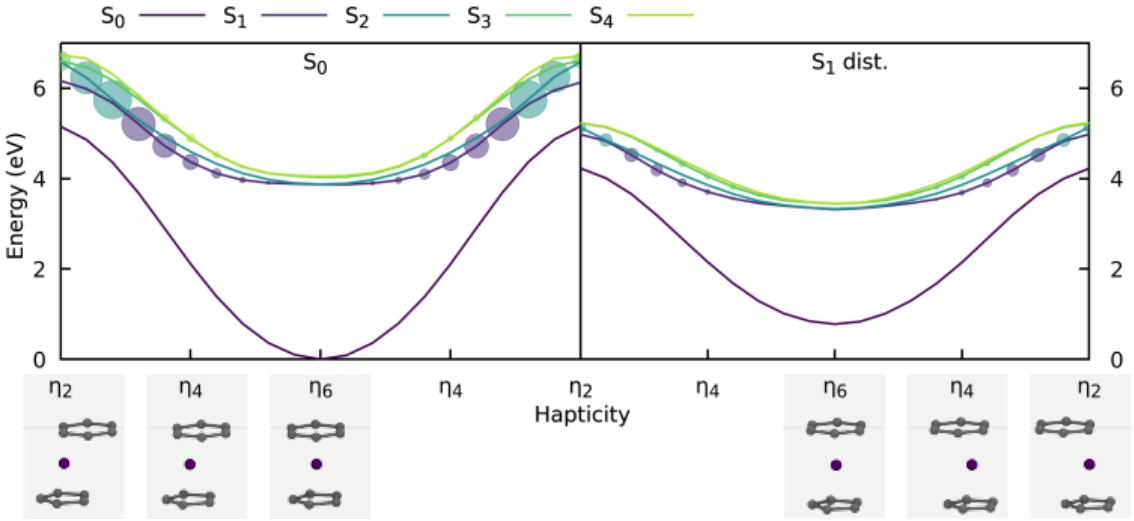

Figure 10: Hapticity scan with a projection interval of 0.0 to 1.0 with a 0.05 step size along the first bisection axis $\boldsymbol{B}_1$. η^2 corresponds to a projection factor of 0.0 and 1.0, η^4 to 0.25 and 0.75, and η^6 to 0.5. S_0 refers to the S_0 minimum geometry, S_1 *dist* to the S_0 minimum with the Cp and Bz ligand having the respective distances to the Ru atom as encountered in the S_1 minimum structure. The Bz ligand was translated along the $\boldsymbol{B}_1$ axis while Ru and the Cp ligand remained fixed. For each scan structure, the oscillator strength of the LR-TDDFT transitions is indicated by the size of the spheres. All energies are given relative to the S_0 minimum geometry.

When focusing on figure 10 it can be seen that for both structures the energy minimum lies at a scalar projection value of 0.5, which corresponds to a hapticity of η^6. This result is fully in line with the expectations. Furthermore, both energy scans presented in figure 10 are symmetric, which again represents an expected result as both Ru complexes are symmetric, and thus no side of the Bz ring should be energetically more favorable. Concerning the energy value encountered at both minima it can be said that for the structure with increased Ru-Bz and Ru-Cp distances a higher minimum energy is obtained than for the optimized ground state structure. In addition, the increase in energy encountered when

lowering the hapticity is less pronounced for the modified structure than for the optimized structure. These findings are in line with the expectation as increasing the Ru-ligand distances hinders the orbital interaction thus destabilizing the whole complex and causing the higher minimum energy. The weakened Ru-Bz interaction also explains the less pronounced energy increase when lowering the η value found for the modified structure. The optimized structure, having a more favorable interaction between the Ru and the Bz ligand, is more affected by any distortion it is submitted to.

When examining the LR-TDDFT transitions computed for the scan structures it can be observed that the character of the brightest transitions is preserved in between the S_0 and the distance modified structures as can be gathered from the spheres indicating the oscillator strengths in figure 10. For both scans the character of the brightest transition changes from an S_1 transition for hapticities not lower than η^4 to a predominant S_2 character for η values further below 4. For the optimized structure, S_3 and S_4 transitions overweigh at the very end points of the scan corresponding to η^2 coordination.

An observable difference between the two scans is that the oscillator strengths encountered for the S_0 minimum scan are higher than those for the modified S_0 structure scan. This result might indicate that orbital interactions are more pronounced for the optimized structure as an optimal distance for the ligand-Ru interaction is provided. For the excited state energies the same behavior is observed with regard to the modified structure as for the S_0 energy. The increase in excited state energies for lowered hapticities is less pronounced in the modified structure than for the optimized structure which again indicates that increasing the Ru-ligand distance lowers the interaction.

In summary it can be stated that the linear hapticity scans support the assumption discussed in section 4.2.4 that hapticity changes along the two symmetrical sides of the Bz hexagon are identical. From this observation it can be gathered that no information is lost when the projection values $\bar{p}_i'$ in the [0.0,1.0] interval are transferred into the [0.0,0.5] interval of $\bar{p}_i$. Furthermore, a comparison of the scan on the optimized and the modified structure shows that increasing the Ru-ligand distances weakens the Ru-Bz bond and lowers the energy barrier for hapticity fluctuations. This finding indicates that a further weakening of the Ru-Bz bond due to excitation into the antibonding Ru-Bz orbital will most likely further facilitate a lowering of hapticity.

6 Time-resolved hapticity - An adiabatic perspective

In the following, we propose to investigate how the geometry descriptors presented in section 4.2 behave in different adiabatic dynamics of Ruwich. To achieve this goal, dynamics in the S_0 and S_1 state were performed on Ruwich. In the ground state, a simulation period of 10 ps was chosen to get representative equilibrium data on the geometrical changes of Ruwich. The obtained data served as a test case for the four geometrical descriptors presented in section 4.2. The adiabatic S_1 dynamics simulation, carried out for 1400 fs was performed to obtain more insight into the possible deformations and hapticity changes in Ruwich. Further details on the adiabatic simulations are provided in section 3.2.

6.1 The S_0 reference

A 10 ps ground state dynamics simulation was performed to obtain a measure of equilibrium values for the four geometry descriptors in Ruwich. From this simulation, the centroid distances δ, hapticity projection factors $\bar{p}_i$, tilt angles θ, and claw angles κ presented in figure 11 were extracted. The simulation started from one initial condition taken from a Wigner sampling around the ground state minimum structure. From figure 11 it can be gathered that all four parameters show only little deviation from an initial value, as expected for a ground state dynamics simulation in proximity of the minimum. The Ru-Bz centroid distance δ (see fig. 11a) never reaches a value above 0.2 Å within the entire simulation suggesting that the Ru-Bz coordinative bond is stable in the ground state. Equivalently, the hapticity parameters $\bar{p}_i$ (see fig. 11b), calculated with respect to the three bisection axes $\boldsymbol{B}_1$, $\boldsymbol{B}_2$, and $\boldsymbol{B}_3$ do not diverge from the equilibrium value of 0.5, implying an η^6 hapticity mode for Bz. Obtaining an η^6 hapticity agrees well with the weak distance variations suggested by δ. Both findings indicate the Ru-Bz six-fold coordination to be stable in the ground state. The stability of the ground state η^6 geometry is additionally supported by the tilt angles θ_i (see fig. 11c), showing only slight oscillations around 90°. A value close to 90° for all three θ angles indicates that Bz remains parallel to its initial orientation. With further focus on the θ_i values correlated oscillations around the equilibrium value of 90° can be observed. The correlated oscillations suggest that tilt movement undergone by Bz is reflected in each of the three tilt angles. This finding suggests that the Bz ring remains planar during the ground state dynamics as all θ_i are equally affected by a tilt movement. The claw angle κ (see fig. 11d) oscillates around the equilibrium value of 180°, the angle expected for the S_0 minimum geometry where the Bz centroid, the Cp centroid, and Ru are aligned.

To summarise the findings obtained from the Ruwich ground state dynamics simulation presented in figure 11, it can be stated that all geometry parameters presented in section 4.2 yield values expected for the ground state minimum structure of Ruwich. Therefore, a first validation of the definitions used for the geometry parameters δ, $\bar{p}_i$, θ_i, and κ was achieved. The oscillations around equilibrium values observed for $\bar{p}_i$ are used in the following analysis to define a threshold for the determination of hapticity changes. Hereby, a value of 0.4324, which corresponds to the ground state standard deviation of $\bar{p}_i$ multiplied by 3, was used to define the lower bound of the hapticity threshold window.

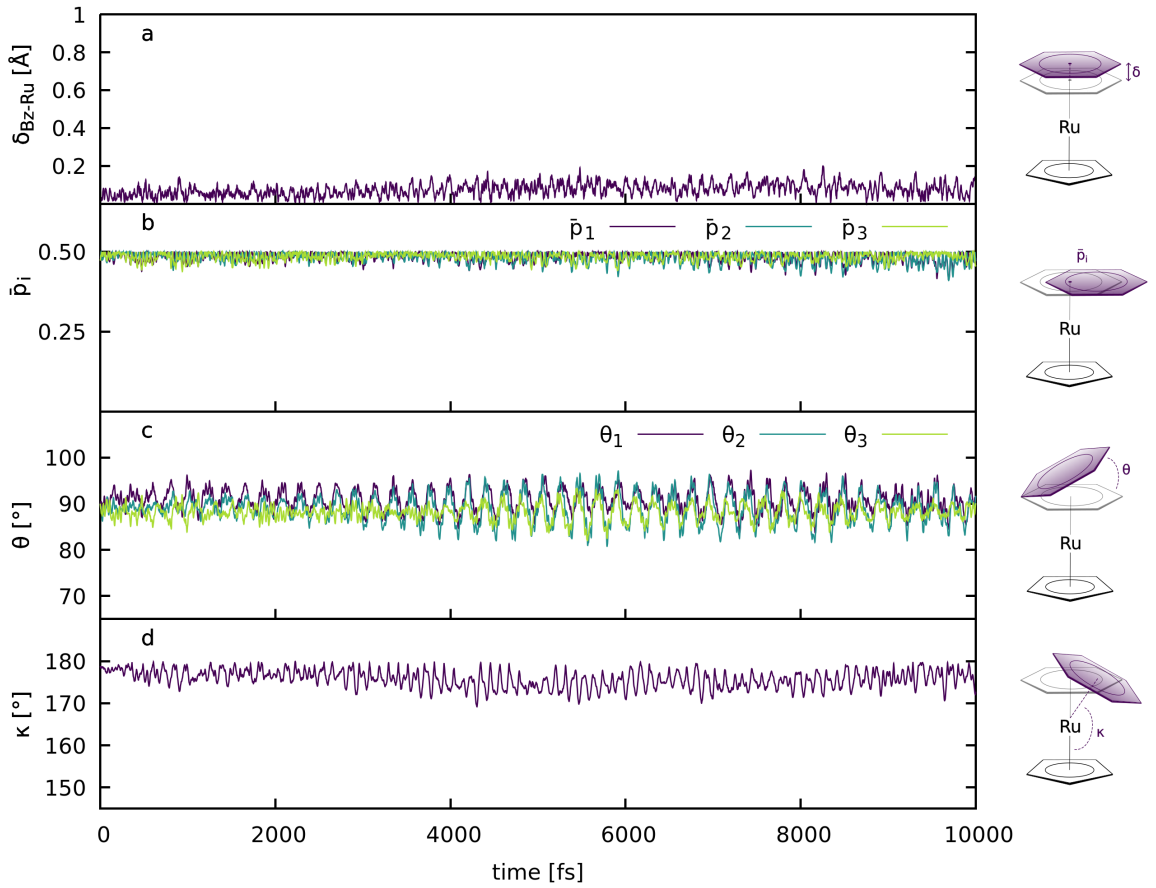

Figure 11: The four parameters δ, $\bar{p}_i$. θ, and κ for the Ruwich geometry changes during the S_0 dynamics. Panel a: the distance between the initial and the current Bz centroid, δ. Panel b: the hapticity projection factor for Ru with respect to Bz, $\bar{p}_i$. Panel c: the tilt angle θ between the current and the initial Bz ring position. Panel d: the claw angle κ between the two lines from Ru to the Bz and the Cp centroid.

6.2 Geometry changes in the adiabatic S_1 dynamics

We investigated the adiabatic molecular dynamics on S_1 presented in figure 12 to get a first insight into the excited state dynamics of Ruwich and to obtain a further validation of the four geometrical descriptors δ, $\bar{p}_i$, θ_i, and κ. The corresponding geometry-based parameters δ, $\bar{p}_i$, θ_i, and κ can be found in figure 12. The Ru-Bz centroid distance δ given in reference to the distance of 1.73 Å in the starting structure is presented in figure 12a. As a first remark, it can be stated that δ increases up to an end value of 0.80 Å. The growth tendency of δ is accompanied by an oscillation where one oscillation period has a duration slightly above 200 fs. An exemplary snapshot of the Ruwich structure for the δ peak in the first oscillation period is provided in figure 12 where a light grey rectangle indicates the peak interval around 110 fs. The displayed snapshot is a representative example of a structure with near equilibrium projection factors $\bar{p}_i$, tilt angles θ_i, and claw angle κ but a

local maximum in δ. From examining the snapshot it can be seen that the structure shows distortion in the Bz arrangement while the overall ring remains parallel to the Cp ligand.

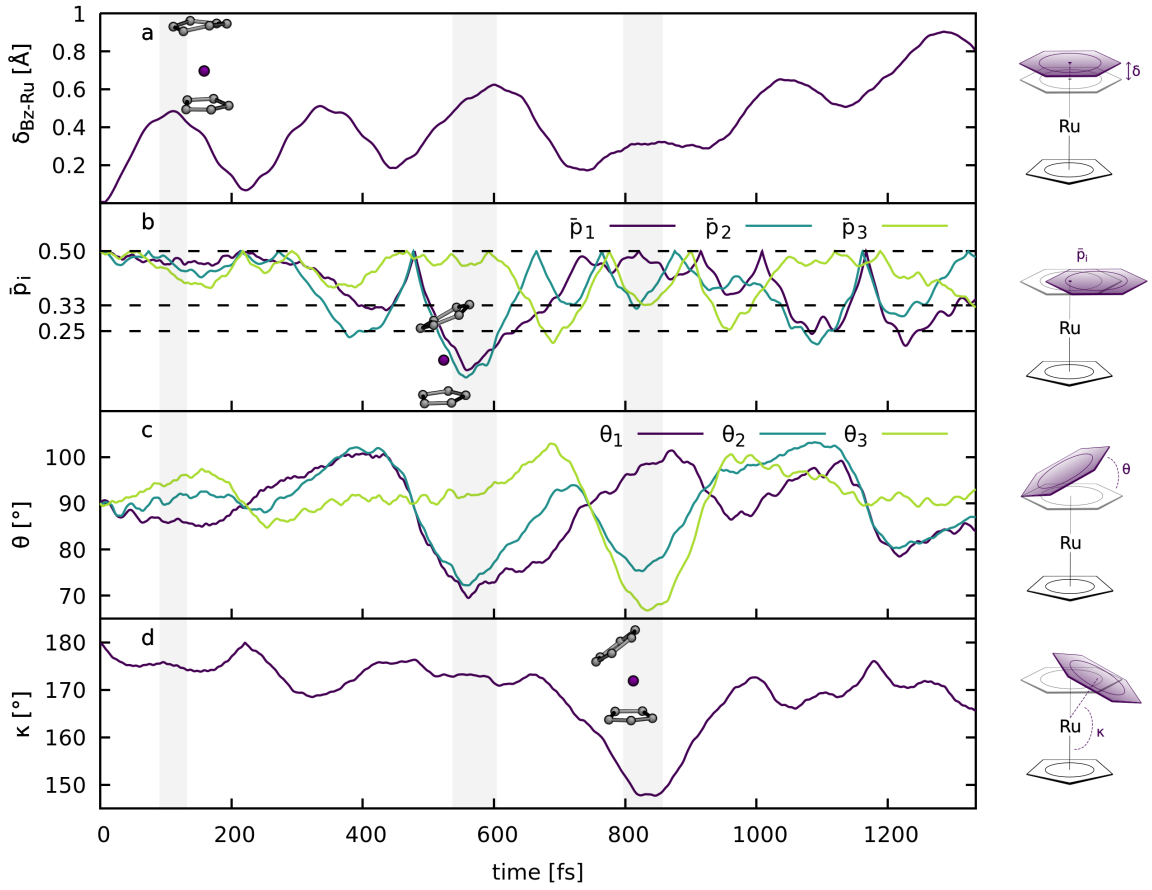

Figure 12: The four parameters δ, $\bar{p}_i$, θ_i, and κ for the Ruwich geometry changes during the S_1 dynamics. Panel a: the distance between the initial and the current Bz centroid, δ. Panel b: the hapticity projection factor for Ru with respect to Bz, $\bar{p}_i$. Panel c: the tilt angle θ between the current and the initial Bz ring position. Panel d: the claw angle κ between the two lines from Ru to the Bz and the Cp centroid. Light-grey rectangles and snapshots of representative Ruwich structures are used to indicate time intervals where the geometry parameters suggest strong changes in the Ruwich structure.

Focussing on the two parameters, $\bar{p}_i$ and θ_i, specific to the bisection axes B_i, it can be gathered from figure 12b and 12c that extreme values for these two parameters peak whenever high δ values are reached. This behavior is observable in the time interval shortly before 600 fs indicated by a light-grey rectangle in figure 12. The local maximum in δ is accompanied by a local minimum in $\bar{p}_1$, and $\bar{p}_2$ as well as local minima in θ_1 and θ_2. The corresponding Ruwich structure is shown as a snapshot in figure 12 next to the rectangle indicating the respective time interval. The Bz ligand is elevated on one side and is subjected to a slip distortion causing the lower θ_i and $\bar{p}_i$ values. However, the snapshot

shows that, despite the substantial deviation from the ground state geometry, the Bz ligand remains planar.

When δ reaches a local minimum as e.g. at 475 fs, the opposite behavior can be observed. The projection factors $\bar{p}_i$ lie closer to the equilibrium value of 0.5 while the tilt angles θ_i meet at their equilibrium value of 90°. This finding indicates that a decrease in the Ru-Bz distance favors an η^6 hapticity which is reflected by the $\bar{p}_i$ and θ_i values. An increase in δ favors a lowering of the hapticity which is mirrored by changes in the $\bar{p}_i$ and θ_i values. The observed correlation between the Ru-Bz distance δ and the B_i axes dependent parameters $\bar{p}_i$ and θ_i suggests that at higher distances the interaction between Ru and Bz is weakened. Being more loosely bound to Ru allows the Bz structure to undergo more pronounced geometrical changes.

When going back to figure 12a depicting the Ru-Bz distance δ, an interruption in the aforementioned oscillation can be observed between 800 and 900 fs. In this time interval, the Ru-Bz distance remains at a constant value of around 0.30 Å. While δ remains constant, a global minimum is encountered for κ at a value of 148°at 825 fs (see fig. 12d). The low κ value indicates that, while the Ru-Bz distance remains constant, one side of Ruwich opens up for potential coordination of a new ligand. A snapshot is provided in figure 12 next to the light-grey rectangle indicating the time interval from 800 to 900 fs to give an impression of how this opening movement reflects on the structure of Ruwich. The depicted structure shows that the Bz centroid is no longer aligned with the Ru and Cp centroid positions. One might expect the opening of a coordination site to be accompanied by a strong tilt of the Bz ligand and a significant decrease of the projection factors $\bar{p}_i$ indicating decreasing hapticity. When focusing on 12c, it can indeed be observed that the Bz ligand shows a strong tilt along the axes $\boldsymbol{B}_2$ and $\boldsymbol{B}_3$ of 76° and 67°, respectively, during the indicated time interval while the B_1 tilting angle increases towards 99°. Observing low tilt angles for $\boldsymbol{B}_2$ and $\boldsymbol{B}_3$, but an angle above 90°for B_1 implies that the ring shows a strong upwards bend at the side of C atoms 5, 6, and 1 (see fig. 3 and sec. 4.2 for more details) while the C-C bond where $\boldsymbol{B}_1$ terminates points downwards. Combining the findings of a low claw angle κ and tilt angles θ_i yields the insight that Ruwich opens up for potential new coordination partners at the side of the carbon atoms 1, 5, and 6. At the same time, the Ru atom becomes shielded towards any new coordination at the side of the C atoms 2, 3, and 4. The geometry descriptors do not only indicate that a coordination site opening occurred but also allow for determining the exact position in the Ruwich complex that is now more reachable. The κ angle serves to indicate the opening while the θ_i values serve to identify which side of Ruwich becomes more accessible. The so-acquired piece of information could be of high interest when studying complexes with non-symmetric substitution patterns.

The projection values $\bar{p}_i$ in the time interval of 800 to 900 fs are close to 0.50 for the projection along $\boldsymbol{B}_1$ and close to 0.33 for $\boldsymbol{B}_2$ and $\boldsymbol{B}_3$ (see fig. 12b). When compared to the overall encountered fluctuations these values for $\bar{p}_i$ are not particularly low. As up to this point, no approach of combining the three projection values $\bar{p}_i$ into one hapticity value has been applied, the relatively high values between 800 and 900 fs could indicate that the hapticity remains close to the equilibrium. However, focussing on the snapshot representative of the respective time interval (see fig. 12) reveals that Ru is not located at a central position below Bz. This contradiction highlights the crucial role of combining the three projection values into one hapticity value that incorporates the information from all three $\boldsymbol{B}_i$ axes.

When focusing solely on figure 12b depicting the projection values $\bar{p}_i$, the highest deviation from the value of 0.5 is encountered around 550 fs where $\bar{p}_1$ reaches a value of 0.13 and $\bar{p}_2$ takes a value of 0.11 while $\bar{p}_3$ remains close to 0.50. The snapshot provided for the respective time interval before 600 fs indicated by a light-grey rectangle (see fig. 12) has been described above in the discussion of δ. The hapticity values in this time interval suggest that ruthenium is mostly coordinated to the carbon atoms 1, 2, and 3, where the axes $\boldsymbol{B}_1$ and $\boldsymbol{B}_2$ originate, while the other four carbon atoms are located further away from Ru. This observation is also supported by the tilt angles θ_1 and θ_2 below 90° encountered for the $\boldsymbol{B}_1$ and $\boldsymbol{B}_2$ axes (70° and 72° respectively). The κ angle in the respective time interval is not differing substantially from the equilibrium value of 180°, indicating that Bz remains aligned with Ru and the Cp centroid. Taken together, the information from $\bar{p}_i$, θ_i, κ and δ can be interpreted as a shift in hapticity from η^6 to a lower value caused by an upwards tilt of three C atoms. During the upwards tilt the Bz ring remains in a position aligned with the Cp ligand. From the latter finding, it can be deduced that the hapticity change, not caused by a change in the claw angle κ, must originate from a slip-like translation of the Bz ring. This assumption is supported when focusing on the respective snapshot presented in figure 12.

After examining the time intervals between 800 and 900 fs and 525 and 600 fs more closely, two distinct patterns of movement causing hapticity change can be deduced. The first, encountered between 800 and 900 fs, consists of a rotation of the Bz centroid around Ru reflected in a strong change of the claw angle κ. The rotation around Ru is also indicated by an interruption of the otherwise oscillating Ru-Bz distance δ. The second movement pattern is indicated by a strong lowering in hapticity projection values $\bar{p}_i$ and tilt angles θ_i while κ and δ show no remarkable changes. The resulting geometry is characterized by a tilt and slipping of the Bz ring whose centroid remains aligned with Ru and the Cp centroid.

The clear distinction between the two movement patterns described above offered by the geometrical parameters δ, θ_i, κ, and $\bar{p}i$ supports the ability of these descriptors to detect geometry changes undergone by Ruwich. However, the lack of a method to combine the three projection values $\bar{p}_i$ into one hapticity value is also prominent. Without a well-defined value unambiguously determining the hapticity it remains impossible to connect observed movement patterns to an η value. We will tackle this substantial problem in the upcoming sections.

6.3 Role of the dihedral angle changes - Does the Bz ring bend?

Before tackling the question of how to combine the three projection values $\bar{p}_i$ into one hapticity parameter, we wanted to assess the influence of dihedral angle changes in Bz on geometry changes in Ruwich. To this end, the dihedral angles of the ground state dynamics and the S_1 dynamics were compared. In this way, the influence of kinks in the Bz ring on hapticity changes was investigated. This additional analysis was carried out as hapticity changes can either be associated with a ring bend[76] or the slip distortion of a planar ring as discussed in chapter 1.2. In figure 13 the six dihedral angles of the Bz ring for the S_0 and S_1 dynamics are presented. To give a notation of the dihedral angles in Bz, $d_{1,2}$ describes the torsion between C1 and C2, up to $d_{6,1}$ giving the torsion between C6 and C1. During the S_0 dynamics (see fig. 13a), the Bz dihedral angles remain at values below 30° while showing

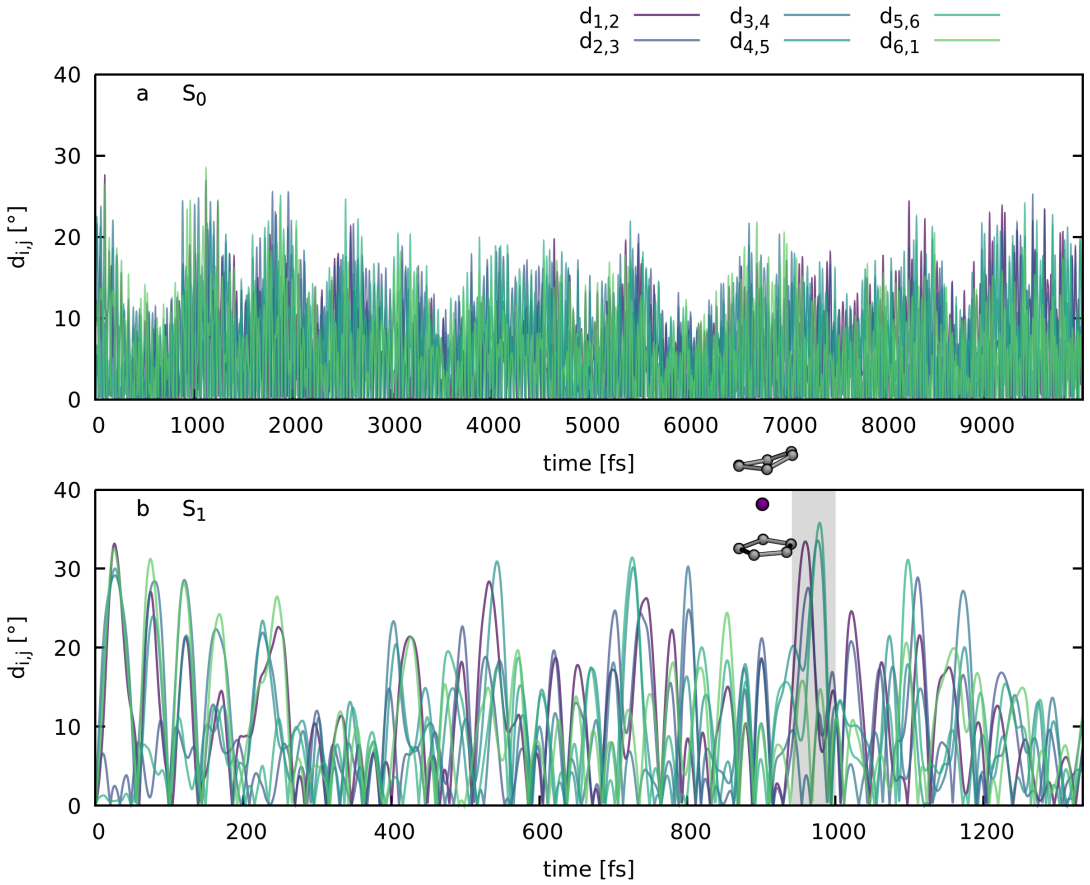

Figure 13: The dihedral angles $d_{i,j}$ for the six C atoms of the Bz ring, numbered in accordance with figure 3 of the ground state (panel a) and the S_1 dynamics (panel b).

fluctuations. When comparing the dihedral angle changes of the S_1 dynamics to the S_0 reference, it can be observed that the ground state equilibrium value of 30° is only rarely surpassed in the first excited state. However, in a few time intervals, the equilibrium value is surpassed by several C-C bonds. Structures in the time interval between 900 and 1000 fs, indicated by the light-grey rectangle in figure 13b, were analyzed to further investigate this behavior. A geometry representative for the considered time interval is presented next to the light-grey rectangle in figure 13b. The geometry parameters $\bar{p}_i$, θ_i, and κ were analyzed for this structure with local dihedral angle maxima. The hapticity projection factors $\bar{p}_i$, encountered in the 900-1000 fs interval, lie around 0.33 for $\boldsymbol{B}_1$ and $\boldsymbol{B}_2$, and at 0.25 for $\boldsymbol{B}_3$. The tilt angles θ_i and the claw angle κ stay rather close to the ground state equilibrium values of 90° and 180°, respectively. The projection values indicate a reduced coordination of Bz to Ru while the angle parameters suggest that the overall Ruwich structure does not deviate substantially from the ground state minimum geometry. This finding is well in line with the high dihedral angles encountered that suggest a bent within the Bz ring to be responsible for the reduced hapticity. The snapshot in figure 13b indeed shows an upward bent in the Bz ring as a cause for the reduced coordination. The presented analysis suggests

that, during the time interval from 900 to 1000 fs, Ruwich follows the conventional picture of a Bz ring bend being responsible for the hapticity change.

From the comparison between S_0 and S_1 dihedral angle changes it can be deduced that the excited Bz ring does only in a few cases experience any bending motion considerably stronger than in the ground state. This observation implies that the priorly discussed variations in the geometrical parameters δ, $\bar{p}_i$, θ_i, and κ shown in figure 12 are required to obtain a more broad depiction of geometry changes in Ruwich. Solely focusing on dihedral angle changes would not allow for the detection of all hapticity changes occurring in the excited state dynamics. The observation that hapticity changes do not only arise from changes in the dihedral angles is contrary to the classical picture of hapticity change in the Bz ligand. As shown above, variations in the coordination must be provoked by other structural changes, such as slip distortion of the Bz ligand, a tilt of the whole ring, or a lowering of the claw angle. These geometry changes are depicted in the $\bar{p}_i$ values, the θ_i angles, and the κ angle. The analysis of the Bz dihedral angles highlights that a Bz hapticity change must not necessarily arise from a bending within the ring, but might as well be caused by translation, bending, and rotation undergone by the entire ring.

6.4 From three projection factors to one hapticity value

As already hinted at in the previous analysis, special care should be directed to the fact that the deduction of a single hapticity value from the three $\bar{p}_i$ projection values is not straightforward. The question of how to evaluate the interplay between the three projection values arises. In a first attempt to answer this question, we focussed on the interval between 525 and 600 fs in the adiabatic S_1 dynamics (see fig. 12b) already discussed in section 6.2. Between 525 and 600 fs, two $\bar{p}_i$ values deviate substantially from the equilibrium value of 0.5 while one remains at 0.5. From discovering this clear difference between the $\bar{p}_i$ values we further observed that several similar cases are encountered throughout the dynamics. To state an example, between 1000 and 1150 fs two projection values are again noticeably below 0.5 while one $\bar{p}_i$ remains close to 0.5. The observation of this pattern suggested that the distinction between projection values close to and far from 0.5 is often easily achieved. Thus, we developed a hapticity scheme only relying on the question of whether the projection values are close to the equilibrium value of 0.5. The subsequent deliberations gave rise to the distinguishing equation (56) in section 4.2.4.

When combining the $\bar{p}_i$ projection values into one hapticity according to equation (56) one arrives at the step function for hapticity change provided in figure 14a. The hapticity obtained according to equation (56) is referred to as $\dot{\alpha}$, where a sub-script shall indicate the coordination number, to distinguish this clearly defined value of hapticity from the η value established by Cotton. $\dot{\alpha}$ is pronounced *halpha* as the ˙ accent signifies the rough breathing (*spiritus asper*) sound the latin alphabet represents with the letter *h*. In figure 14 the $\dot{\alpha}$ value is shown alongside the symmetrized $\bar{p}_i$ (14b) and the non-symmetrized $\bar{p}_i'$ ranging from 0 to 1 (14c). The presented view of increasing detail allows for comparison between the effective hapticity value $\dot{\alpha}$ and its contributions. The $\bar{p}_i'$ represents the exact position of Ru below the Bz ring as information from the two halves of the ring is not condensed. The symmetrized $\bar{p}_i$ allows for a better overview of the Ru position, as distinguishing between two sides of the hexagon does not provide new information in the symmetric Ruwich complex. One should note that, in principle, condensing the information into one triangle formed

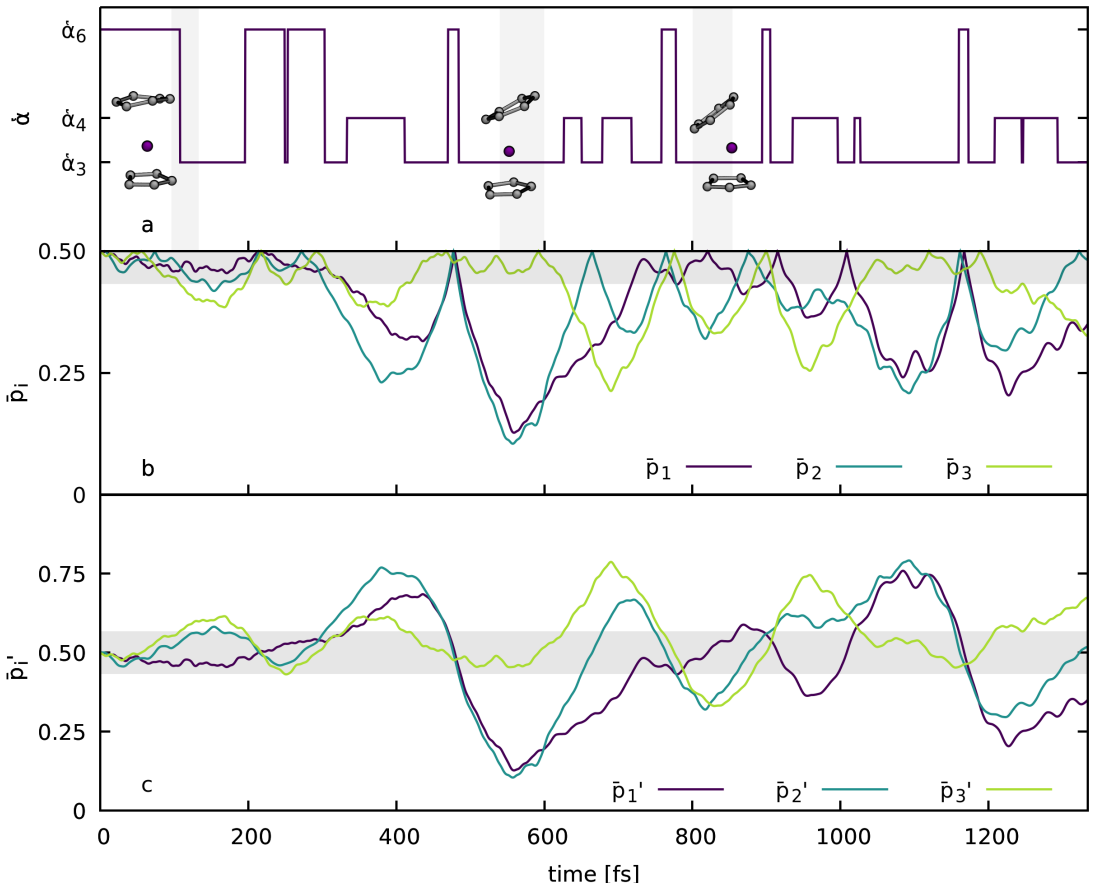

Figure 14: The time-dependent hapticity of Ruwich at different levels of detail. Panel a: the hapticity value $\dot{\alpha}$, panel b: the projection values $\bar{p}_i$, panel c: the non-symmetrized projection values $\bar{p}_i'$ from the adiabatic S_1 dynamics. The light-grey rectangle in panels b, and c indicates the threshold value used in the determination of $\dot{\alpha}$.

between two bound C atoms and the Bz centroid would be sufficient to include all information. However, as this view of the Bz ligand is rather counterintuitive, the representation was discarded. The symmetrized $\bar{p}_i$ values are then condensed into a value of $\dot{\alpha}_6$, $\dot{\alpha}_4$ or $\dot{\alpha}_3$ allowing for quick identification of structures with similar Ru coordination throughout the simulation. A way to quickly identify Ruwich structures with similar binding modes is, as highlighted before, crucial and made possible by computing the $\dot{\alpha}$ value.

To further discuss the composition of the $\dot{\alpha}$ value, the reader's attention shall be drawn to the threshold area indicated by the light grey rectangle in figure 14. In figure 14b, one can effortlessly identify whether the $\bar{p}_i$ values lie within or outside of the threshold area. When focussing on instances where Ruwich shows a $\dot{\alpha}_6$ hapticity it can be seen that the corresponding $\bar{p}_i$ values all lie within the threshold. This becomes especially clear at around 450 fs and 1150 fs where all $\bar{p}_i$ show a short dip of reaching 0.5. Throughout these instances $\dot{\alpha}$ peaks to a value of 6. It can equally be seen for periods of $\dot{\alpha}_4$, as e.g. around 700 fs, that

the corresponding $\bar{p}_i$ all lie outside the threshold window For episodes of $\mathring{\alpha}_3$, which can e.g. be encountered in the aforementioned interval between 525 and 600 fs, one $\bar{p}_i$, in this case $\bar{p}_3$, lies within the threshold. For a $\mathring{\alpha}_3$ coordination, the displacement axis of Ru can be deduced from the $\bar{p}_i$ found to remain in the threshold. To explain this behavior for the 525-600 fs interval, where $\bar{p}_3$ remains in the threshold, the orientation of the $\boldsymbol{B}_3$ axis needs to be considered. $\boldsymbol{B}_3$ connects the edge mid points e_{34} and e_{61} (see fig. 3). Therefore, Ru must be displaced along the axis connecting C2 and C5 to yield a projection value of 0.5 with respect to $\boldsymbol{B}_3$. Similarly, the Ru displacement axis can be obtained for all $\mathring{\alpha}_3$ coorinations. When further considering the non-symmetrized $\bar{p}_i'$ values in the interval from 525 to 600 fs figure 14c shows that $\bar{p}_1'$ and $\bar{p}_2'$ both lie below the threshold window. $\bar{p}_i$ values lower than 0.5 indicate that Ru must be located below the area spanned by the parallelogram of C atoms 1,2, and 3, and the Bz centroid. From considering the non-symmetrized $\bar{p}_i'$ values, one can thus obtain the full information on the Ru position with respect to the Bz ring. One can thus always reconstruct the exact Ru position from a certain $\mathring{\alpha}$ value when taking into account all non-condensed information.

However, identifying the Ru displacement axis for $\mathring{\alpha}_4$ coordinations is less straightforward as all $\bar{p}_i$ lie outside the threshold window. But, from focussing on the $\mathring{\alpha}_4$ cases in figure 14a, identifying a minimal $\bar{p}_i$, significantly lower than the other two, is possible. To state an example, the $\mathring{\alpha}_4$ interval between 300 and 400 fs shows a $\bar{p}_2$ value further below 0.5 than the $\bar{p}_1$ and $\bar{p}_3$ values (see fig. 14b). This finding indicates that Ru is displaced along the $\boldsymbol{B}_2$ axis, causing a more pronounced decrease in the respective projection value. Taking into account the more detailed information provided by the non-symmetrized $\bar{p}_i$ values (see fig. 14c), it can furthermore be seen that Ru followed the $\boldsymbol{B}_2$ axis to approach the C atoms 5 and 6, as the corresponding $\bar{p}_i$ values all lie above 0.5. $\mathring{\alpha}_4$ coordinations thus equally offer the possibility to identify a more precise location of Ru, when taking into account the full picture provided by the $\bar{p}_i$ values.

The presented discussion of figure 14 highlights the ability of the $\boldsymbol{B}_i$ axes to serve as a coordinate system in the description of the Ru position below the Bz ring. Equally, the $\mathring{\alpha}$ value is suitable for condensing the information from this coordinate system into one hapticity value. Therefore, the $\boldsymbol{B}_i$ axes yielding the $\mathring{\alpha}$ value make the identification of Ruwich structures with similar coordination more straightforward.

When exchanging the $\bar{p}_i$ values shown in figure 12b with the $\mathring{\alpha}$ value, one obtains the overview presented in figure 15. From examining figure 15b it can be gathered that the previously discussed intervals from 525 to 600 fs and from 800 to 900 fs correspond to the same coordination mode of $\mathring{\alpha}_3$. Arriving at this equal hapticity value from visual identification of structures obtained in these time intervals would have proven complicated if not impossible. Identifying the hapticity from visual inspection is rendered more complicated for the presented time intervals as the δ and κ values show very distinct behavior. The high δ and equilibrium κ before 600 fs indicate a slip distortion while the low κ after 800 fs can be attributed to the opening of a new coordination site. The $\mathring{\alpha}$ value makes it straightforward to observe that in both highly differing Ruwich geometries, Ru is located below three C atoms of the Bz ring. Furthermore, an inspection of figure 15 shows that the $\mathring{\alpha}$ value supports the aforementioned assumption that low δ values cause hapticities of 6. With the overview provided by $\mathring{\alpha}$, it can more easily be seen that around 425 fs, 775 fs, 850 fs, and 1150 fs, when δ reaches a local minimum, $\mathring{\alpha}$ takes a value of 6.

When asking the question whether the $\mathring{\alpha}$ classification is still valid when the ring starts to

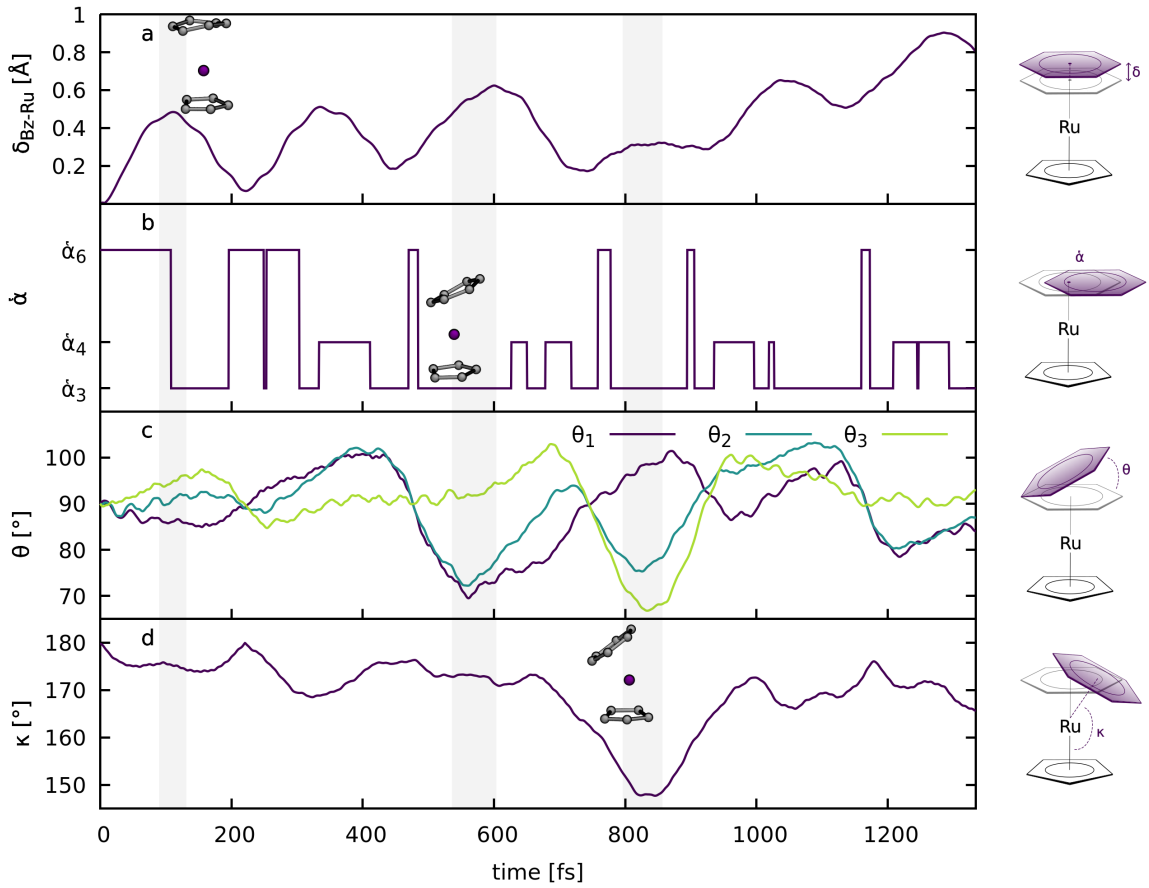

Figure 15: The four parameters δ, $\dot{\alpha}$, θ_i, and κ for the Ruwich geometry changes during the S_1 dynamics. Panel a: the distance δ between the initial and the current Bz centroid. Panel b: the hapticity value $\dot{\alpha}$ for Ru with respect to Bz. Panel c: the tilt angle θ_i for the Bz ring. Panel d: the claw angle κ between the Bz centroid, the Ru atom, and the Cp centroid is shown. Light-grey rectangles and snapshots of representative Ruwich structures are used to indicate time intervals where the geometry parameters suggest strong changes in the Ruwich structure.

deform by dihedral distortions, focus should be laid on the time interval between 900 and 1000 fs highlighted in figure 13b where high dihedral angles are encountered. In this time interval, the Bz ring shows a distortion that, by visual inspection, resembles the classical picture of a Bz ring with η^4 coordination. Mere visual inspection would thus result in the assumption that four C atoms are coordinated to Ru during the time interval. In figure 15b, $\dot{\alpha}$ shows indeed a value of 4 between 900 and 1000 fs. However, when examining the dihedral angle deviations more closely, it can be seen that $d_{4,5}$ and $d_{5,6}$ lie above 30°. $d_{4,5}$ and $d_{5,6}$ are the two adjacent dihedral angles describing the torsion between C atoms 4 and 5, and C atoms 5 and 6. However, to obtain the classic ring bend associated with η^4, the two dihedral angles with high deviation should not be adjacent but have a gap of one bond in between. A further examination of the dihedral angle distribution thus shows that the

$\mathring{\alpha}_4$ geometries between 900 and 1000 fs do not correspond to the classic ring distortion imagined for η^4. Instead, the Bz ring bend involves an out-of-plane displacement of only one C atom while the 4-fold coordination arises from a slip distortion independent of the dihedral angle change. When only relying on high deviations in non-adjacent dihedral angles for detecting η^4 structures, the $\mathring{\alpha}_4$ coordination between 900 and 1000 fs, as well as other structures with reduced hapticity in regions of low dihedral angles, would be missed. The hapticity classification achieved with $\mathring{\alpha}$ can serve to discover a more refined link between dihedral distortions and resulting coordination changes. The $\mathring{\alpha}$ parameter thus shows great potential in discovering patterns of how different ligand distortions, described by the tilt angle θ_i, the claw angle κ, and the dihedral angles $d_{i,j}$, influence the coordination of the metal atom in a sandwich complex.

7 Time-resolved hapticity - A nonadiabatic perspective

In this chapter, we wanted to estimate the importance of nonadiabatic effects for the excited state dynamics of Ruwich, in particular for a time-resolved study of light-induced hapticity changes. To this end, we performed nonadiabatic dynamics simulations on Ruwich using the spawning methods AIMS and AIMSWISS and extracted the time-dependent hapticity parameters. These simulations offered a direct point of comparison to the previously discussed adiabatic AIMD simulation that allowed us to assess the importance of nonadiabatic effects on light-induced hapticity changes in Ruwich.

Before going into discussing the nonadiabatic simulations, one should note that to obtain a representative result from the adiabatic and nonadiabatic simulations, it would have been necessary to simulate from a well-sampled set of initial conditions. Furthermore, it would have been necessary to evaluate the influence of triplet states. However, for the simulations carried out only one initial condition was used and only singlet excitations were considered. The emphasis for the first simulations carried out on Ruwich was more laid on validating the geometry parameters, especially the hapticity parameter $\dot{\alpha}$. A more accurate simulation of the excited state processes in Ruwich can follow after validation of the geometrical parameters is achieved.

7.1 Nonadiabatic dynamics of Ruwich simulated with AIMS

The nonadiabatic dynamics simulated with AIMS was used to study the excited state dynamics of Ruwich starting from the S_1 state. In this way, 214 fs of dynamics were obtained that shall in the following be analyzed using the geometry-based parameters presented in section 4.2. The parameters, already tested in the analysis of the adiabatic Ruwich dynamics in section 6, shall be put to further use and help to investigate the impact of nonadiabatic effects on the dynamics of Ruwich.

The population on S_1, S_2, and S_3 for the AIMS simulation of Ruwich as well as the hapticity parameter $\dot{\alpha}$ and contributing $\bar{p}_i$ values are provided in figure 16a and b. For comparison, the $\dot{\alpha}$ parameter and the three projection factors $\bar{p}_1$ to $\bar{p}_3$ for the adiabatic dynamics in S_1 can be found in figure 16c. The AIMS simulation suggests that the S_1 population is almost entirely transferred to S_2 after 66 fs of the simulation, while the first decrease in S_1 population is observed after only 48 fs. This dominance, only shortly interrupted around 109 fs by a short drop in population in favor of the S_1 state, persists until 149 fs. At this time step the population becomes evenly distributed between S_1 and S_2. After 180 fs, the population on S_1 again outgrows the S_2 population, while the population on S_3 increases from zero to a value of 0.12 at the end of the simulation.

When focussing on the change of the hapticity parameter $\dot{\alpha}$, presented in figure 16b, one can observe that $\dot{\alpha}$ remains at 6 for the first 142 fs. Starting from 142 fs a gradual change from $\dot{\alpha}_6$ to $\dot{\alpha}_3$ occurs over a time period of 24 fs. After this change to $\dot{\alpha}_3$ the AIMS hapticity remains at 3 until the end of the simulation is reached. In the adiabatic S_1 dynamics, presented in figure 16c, a change from $\dot{\alpha}_6$ to $\dot{\alpha}_3$ occurs already after 108 fs, 59 fs earlier than in the AIMS simulation. The adiabatic dynamics simulation thus predicts the first hapticity change to happen too early. When combining the information from the AIMS population and the $\dot{\alpha}$ values, one observes that the $\dot{\alpha}$ change in AIMS occurs when the population migrates from being mostly in S_2 to being evenly distributed between S_1 and S_2. One can thus

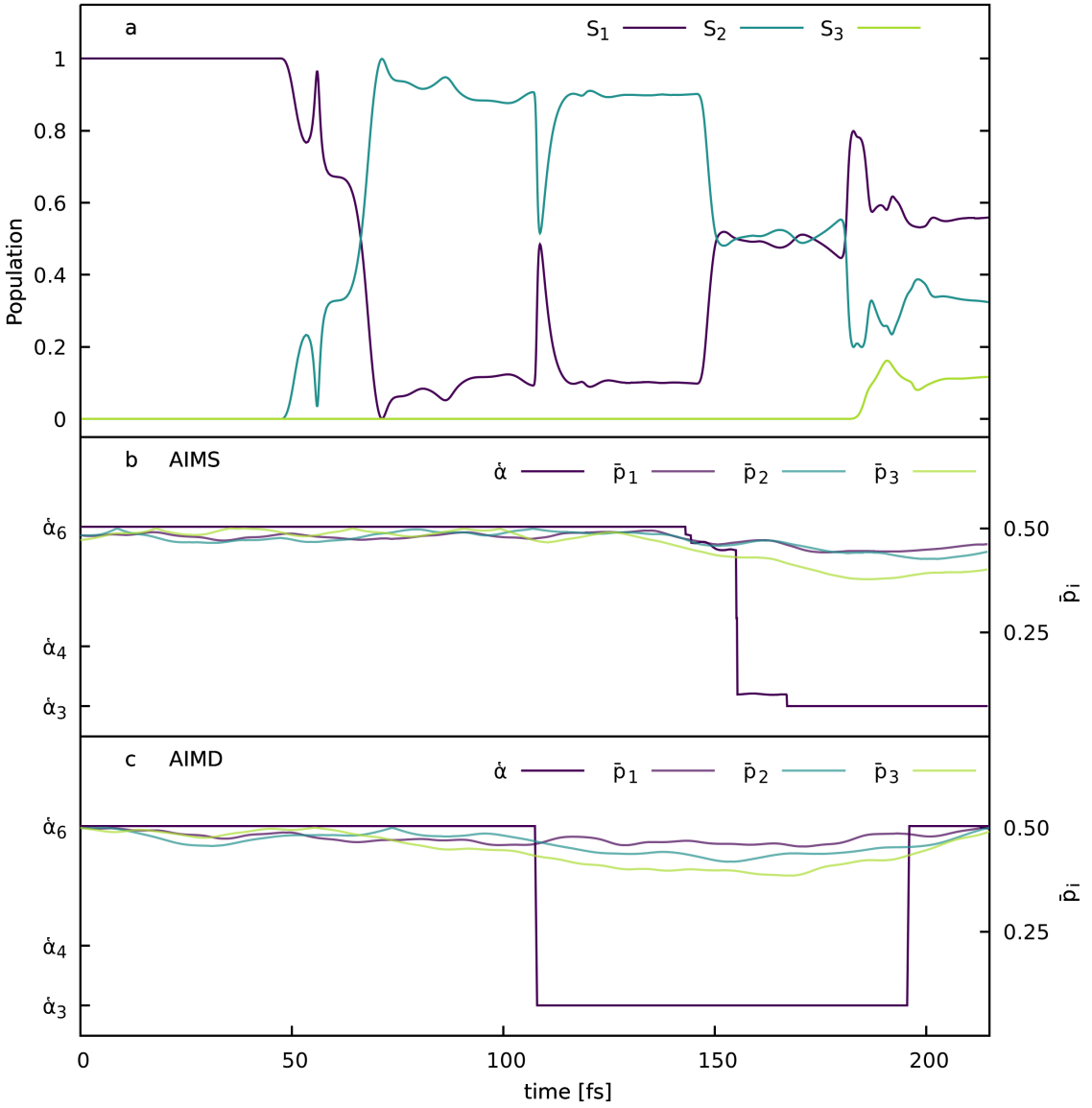

Figure 16: Populations and the hapticity parameter $\dot{\alpha}$ with its contributing projection values $\bar{p}_i$ for the AIMS and AIMD simulations. Panel a: the population in S_1, S_2, and S_3 of the AIMS dynamics. Panel b: hapticity values $\dot{\alpha}$ and projection factors $\bar{p}_i$ for AIMS. Panel c: hapticity values $\dot{\alpha}$ and projection factors $\bar{p}_i$ for AIMD.

suspect that this interplay between S_1 and S_2 population is necessary to correctly predict the first hapticity change. Therefore, the adiabatic dynamics, limiting the population to evolve on S_1, does not show the first change in $\dot{\alpha}$ at the same time as the AIMS simulation. The evolution of half of the population on S_2 obtained from AIMS cannot be captured in the AIMD simulation, due to the BO approximation applied in the latter. An adiabatic trajectory launched from S_2 might also fail to predict the time of hapticity change correctly, as this trajectory would also be unable to capture the population exchange between S_1 and S_2

necessary to reflect the interplay between electronic state characters.

When comparing the projection values $\bar{p}_1$, $\bar{p}_2$, and $\bar{p}_3$ for AIMS and AIMD presented in figure 16b and c, respectively, it can be stated that the projection values in AIMS stay rather close to their initial value of 0.5 while the hapticity remains at $\dot{\alpha}_6$. Only when $\dot{\alpha}$ gradually decreases to 3, do the projection values change significantly for the first time. In the AIMD simulation however, a change in projection values is already noticeable from the beginning, when $\dot{\alpha}$ does not change yet. At the moment of hapticity change in AIMD the change in $\dot{\alpha}$ does not become noticeably stronger but continues with the same intensity. When $\dot{\alpha}$ increases back to 6 at 196 fs in the AIMD simulation, the $\bar{p}_i$ value change is again not located around the respective time step. From this observation, one can deduce that the AIMD simulation yields projection values $\bar{p}_{B_i}$ not as instantaneously changing as in the AIMS dynamics.

When further comparing the adiabatic hapticity change to the nonadiabatic it can be seen that AIMS stays at $\dot{\alpha}_3$ until the end of the simulation at 214 fs is reached. The AIMD run however, switches back to $\dot{\alpha}_6$ at 196 fs. At this time step, the AIMS population is distributed between S_1, S_2, and S_3. Therefore, the difference in predicted hapticities might again arise because the AIMD simulations limits the dynamics to the S_1 state. This observation again highlights the importance of nonadiabatic effects for the excited state dynamics of Ruwich.

From the findings we presented one already sees that in a small time frame of 214 fs major differences in the hapticity change arise between the nonadiabatic AIMS and the adiabatic AIMD dynamics. It can thus be confirmed that the first three excited states highly influence each other in the excited state dynamics of Ruwich. This finding was already indicated by the geodesic interpolation between the S_0 and S_1 minimum presented in section 5.3, and from the fact that Ruwich, as a transition metal complex, is very prone to having close-lying electronic states. The realization that nonadiabatic effects are crucial for the depiction of excited state dynamics of Ruwich asked for nonadiabatic dynamics covering a longer time interval. To this end, AIMSWISS simulations were carried out on Ruwich.

7.2 Nonadiabatic dynamics of Ruwich simulated with AIMSWISS

Due to the aforementioned high computational cost of AIMS simulations, an additional AIMSWISS simulation consisting of 5 individual runs was carried out on Ruwich. As AIMSWISS simulations cover a longer time frame than the 214 fs feasible with AIMS, it was hoped to obtain further insight into the influence of nonadiabatic effects. The AIMSWISS simulation was performed for 1400 fs, the same time interval as covered by the adiabatic AIMD simulation. Results obtained from the AIMSWISS simulation shall be compared to the corresponding AIMS properties for the first 214 fs to validate the AIMSWISS approximation in the application of Ruwich. Secondly, the observables obtained from the AIMS and AIMSWISS dynamics simulation shall be compared to the AIMD results to get an estimate on the influence of nonadiabatic effects on the Ruwich excited state dynamics.

7.2.1 Comparing the population traces for AIMS and AIMSWISS

The populations obtained in the first 214 fs of the AIMSWISS simulation are compared to the AIMS populations as presented in figure 17. From examining the populations in figure 17, one can see that the AIMSWISS population first differs from AIMS shortly after 50 fs,

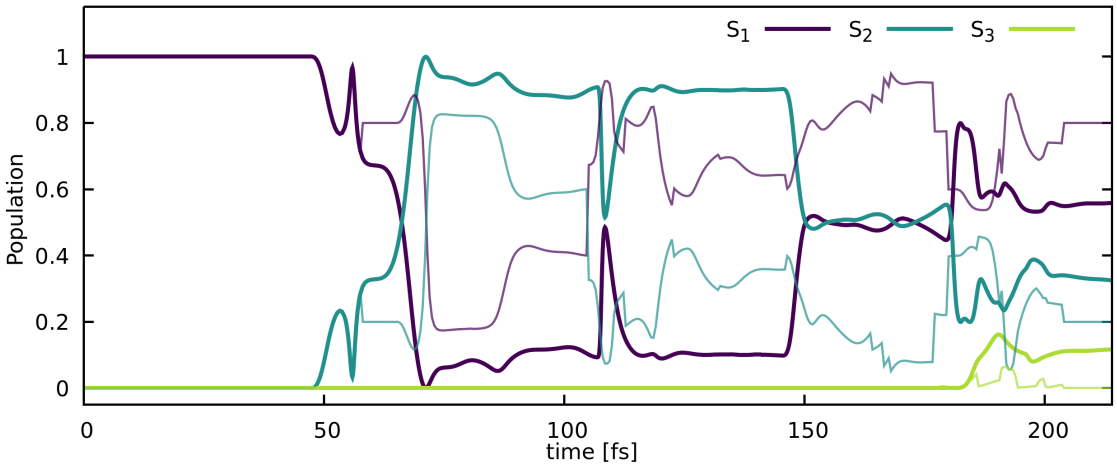

Figure 17: The S_1, S_2, and S_3 populations obtained from the AIMS (heavy lines) and AIMSWISS simulation (thin lines) with 5 individual runs. For the AIMSWISS simulation, only the population in the time frame covered by AIMS is shown.

when the first selection happens in all of the AIMSWISS runs. For the dynamics following these first 50 fs, the differences between AIMS and AIMSWISS populations are substantial. One can observe that, after 105 fs, the S_1 population obtained from the AIMSWISS simulation is always higher than in AIMS. The AIMSWISS simulation maintains the qualitative character of population transfer features in AIMS but does not give the same quantitative populations. This observation can be highlighted when focusing on the time interval between around 70 and 110 fs. In this time frame, the AIMSWISS and AIMS simulations both show a population distribution distinct from other time intervals of the simulation. However, while AIMS yields almost all population on S_2, the AIMSWISS simulation underestimates the amount of population in S_2. When examining further features in population change, as the dip in S_2 population observed in AIMS around 115 fs, it can be stated that AIMSWISS only agrees in the characteristic that a change in population takes place. After 115 fs, the AIMSWISS simulation does not return to a high occupation of the S_2 state but predicts most of the population to be in S_1. From the disagreement between the AIMS and AIMSWISS simulations one can suspect that the 5 AIMSWISS runs carried out were not enough to allow the simulation to statistically converge. As was shown in reference [56], a stochastic modification of AIMS can be brought closer to the AIMS result by carrying out more runs on the respective initial condition. However, as emphasis was more laid on testing the developed hapticity definition, bringing the AIMSWISS simulation to statistical convergence will be a future target. Despite the difficulty of AIMSWISS to be in quantitative agreement with the AIMS simulation, the method captures the increase in S_3 population after 170 fs. Although AIMSWISS underestimates the amount of S_3 population, the fact that this population feature is captured favors the application of AIMSWISS on the Ruwich complex.

While AIMSWISS maintains a few features of population transfer, the almost even population split between S_1 and S_2 from 149 fs to 180 fs that occurs simultaneously to the hapticity change from $\dot{\alpha}_6$ to $\dot{\alpha}_3$ (see fig. 16) is not preserved. Based on this observation, one might assume that AIMSWISS predicts a different time scale for the first hapticity

change than AIMS. To better understand the discrepancies between the AIMSWISS and AIMS population traces the decoherence times and number of successful selections in the AIMSWISS simulation were examined. In AIMSWISS, a warning is issued during the dynamics whenever a mismatch between the predicted decay time and the actual decay at the selection event is observed. Selection processes for which such a warning is issued are termed failed selections, while all other selections can be considered as successful. When examining the ratio between successful and failed selections produced by all 5 AIMSWISS runs, one finds that only 36 % of the performed selections are successful. A low value of successful selections can be caused by an underestimation of the decoherence time τ_D (see eq. (45) in sec. 2.5.3) compared to the actual decoherence one would observe in AIMS.[77] Because of the underestimation, the selection process between two trajectories happens too early, at a time step where the trajectories are not decoupled yet. As the transition metal complex Ruwich has PESs very close in energy, the difference in nuclear forces for two trajectories on different states is low. From this low force difference a long decoherence time τ_D is obtained, as can be seen from equation (45). The long decoherence times expected for Ruwich indicate that although the τ_D values obtained (from 10 fs to up to 30 fs) are unusually long for efficient stochastic selections[77], they could still suffer through an underestimation. The selection between the TBFs might thus still be too rapid to properly account for their interaction. Apart from a potential underestimation, there might also be another reason for the high number of failed selections encountered for Ruwich. As the predicted decoherence times are so long, it might happen that during the long time intervals between the spawning and the selection event the potential landscape changes. Such a change in the potential landscape might lead to new nuclear force differences that were not predictable at the spawning time when τ_D was computed. So, with the almost parallel near-degenerate PESs in Ruwich, AIMSWISS is more likely to suffer from difficulties when applying short and efficient decoherence times as was observed for a different molecule in reference [77]. One would have to investigate whether failed selections are more prone to occur at high or low decoherence times τ_D to rule out the reason for the high number of failed selections. A closer examination of the connection between coherence times and TBF overlaps at the selection event will be of high interest in the future, but went beyond the scope of this project.

7.2.2 The time-dependence of the geometry-based parameters in AIMD, AIMS, and AIMSWISS

Despite the aforementioned difficulties for AIMSWISS to reproduce the AIMS population traces, both nonadiabatic dynamics methods showed more correlation for the time-dependence of the four geometry-based parameters and contrasted with the AIMD simulation. The δ, $\dot{\alpha}$, and κ values for AIMS, AIMSWISS, and AIMD are presented in figure 18 to compare the geometry-based parameters obtained with the three methods. The tilt angles θ_i were no longer included in the analysis as the computation includes a Kabsch alignment for each step of the simulation, a very time-consuming process. Furthermore, it was thought that the θ_i angles do not yield information supplementary to the other three geometry parameters. For three geometry parameters δ, κ, and $\dot{\alpha}$ the nonadiabatic AIMSWISS results are closer to the AIMS result in the first 214 fs than the adiabatic AIMD simulation. The centroid distance δ, shown in figure 18a, for AIMSWISS is noticeably closer to

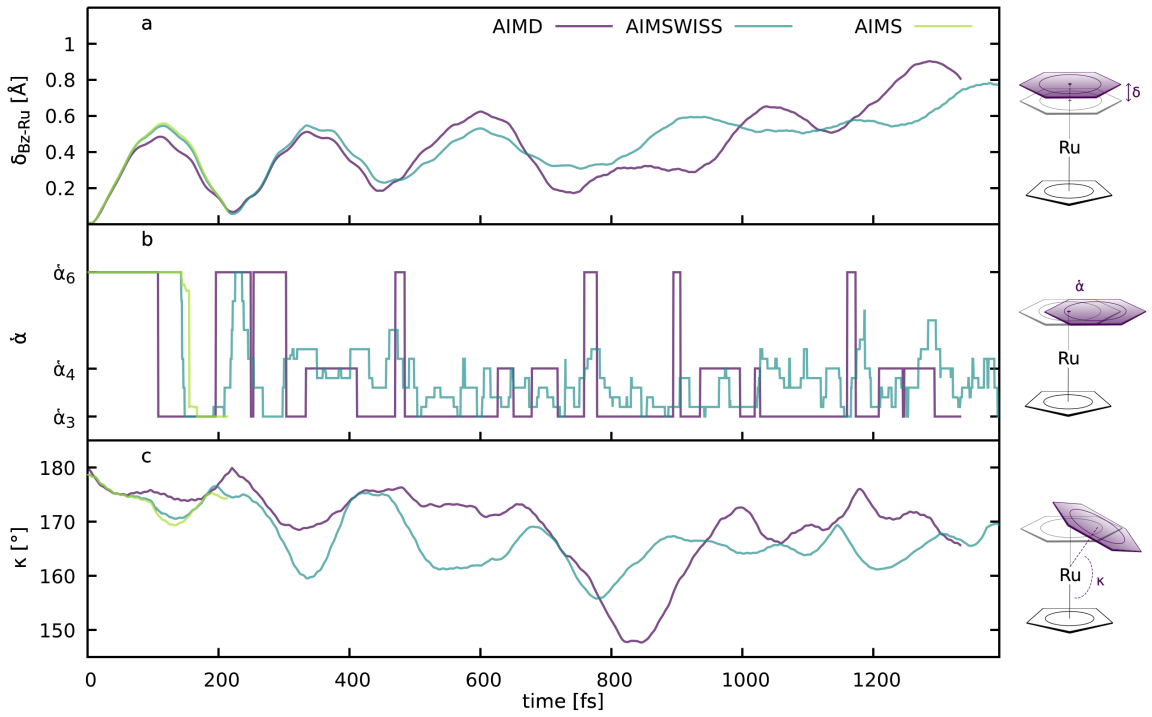

Figure 18: The three parameters δ, $\dot{\alpha}$, and κ for the Ruwich geometry changes in the AIMD, AIMSWISS, and AIMS simulation. Panel a: the distance δ between the initial and the current Bz centroid. Panel b: the hapticity value $\dot{\alpha}$ for Ru with respect to Bz. Panel c: the claw angle κ between the Bz centroid, the Ru atom, and the Cp centroid.

the AIMS result than AIMD. In these first 214 fs, AIMSWISS yields a maximum in centroid distance of 0.54 Å that is much closer to the peak value of 0.56 Å in AIMS than the AIMD centroid distance of 0.49 Å. However, qualitative agreement in δ is fulfilled for AIMSWISS and AIMD as both show an increase followed by a decrease of the Ru-Bz centroid distance. Furthermore, it should be noted that the final lowering of δ in the AIMS simulation is accompanied by the increase in S_3 population, which is also captured by the AIMSWISS dynamics. But, as the local δ minimum is also reproduced by the AIMD simulation, it is unlikely that the increase in S_3 population has a high influence on this aspect of the Ruwich dynamics.

Following the dynamics after 214 fs, it can be seen in figure 18a that until 600 fs AIMD and AIMSWISS show a similar quantitative behavior for δ. In both cases, δ shows an oscillation around a general increase. After 600 fs, the oscillatory increase continues for the AIMD dynamics, only interrupted by δ remaining constant between 800 and 900 fs. This behavior is not reflected by AIMSWISS where δ first shows further increase until remaining constant at a value of around 0.6 Å for 900 to 1300 fs. After 1300 fs, δ further increases for AIMSWISS to reach a final value of 0.8 Å. The constant δ value in the AIMSWISS dynamics is not accompanied by a decrease in the claw angle κ, as is the case in the AIMD dynamics. When examining figure 18c, κ is not significantly decreased for AIMSWISS between 900

and 1300 fs. The constant Ru-Bz centroid distance is thus not attributable to the opening of a new coordination side. A major difference between the reason for a constant δ values can thus be observed for the adiabatic AIMD and the nonadiabatic AIMSWISS dynamics.

For the claw angle parameter κ depicted in figure 18c, another noticeable difference is found for the AIMSWISS and AIMD dynamics. The AIMS simulation yields a minimum of 169.9° while AIMSWISS reaches a local minimum of 170.6° compared to a value of 174.2° for AIMD. AIMSWISS is thus again quantitatively closer to AIMS while also reproducing the qualitative line shape of AIMS more accurately than the AIMD simulation. After the minimum in κ is reached an increase is obtained from all three dynamics methods. Close to 200 fs, the increase of κ is weakened for the AIMS and AIMSWISS simulations, while continuing at its former pace for the AIMD simulation. Soon after, at 190 fs, the κ value of AIMS reaches a maximum of 175.3°, that is closely matched by the AIMSWISS local maximum of 176.5°in κ at 196 fs. In the AIMD simulation, the κ value continues to increase until 221 fs where a local maximum of 179.9° equal to the initial claw angle value is reached. A reasonable explanation for AIMSWISS being qualitatively and quantitatively closer to the claw angles obtained from AIMS than AIMD could be the increasing S_3 population observed after 170 fs, which cannot be captured by the AIMD simulation.

After the first 214 fs that are covered by the AIMS simulation, the κ values from AIMSWISS and AIMD continue to evolve differently. In the AIMD simulation, the κ value mostly varies between 180 and 170° and only shows higher deviations between 800 and 900 fs, as discussed above. The κ values obtained with AIMSWISS are generally lower and vary within an interval between 175 and 165°. The AIMSWISS dynamics thus predicts only small openings of coordination sites equally distributed throughout the simulation, while AIMD suggests only one opening of the Ruwich complex that is more pronounced.

When focussing on the hapticity $\dot{\alpha}$ presented in figure 18b, it can be noticed that AIMSWISS is also closer to the hapticity change as predicted in AIMS than the adiabatic AIMD simulation. As discussed above, the hapticity change in AIMD occurs 59 fs earlier than in the AIMS dynamics. In AIMSWISS, the first change from $\dot{\alpha}_6$ to $\dot{\alpha}_3$ starts at 143 fs where the hapticity gradually changes for 5 fs to then remain at $\dot{\alpha}_3$ after 148 fs. AIMSWISS is not only closer to the time of first hapticity change yielded by AIMS (166 fs) but also gives a time window for the change from $\dot{\alpha}_6$ to $\dot{\alpha}_3$. However, the time window predicted by AIMSWISS only covers 4 fs while AIMS predicts an interval of 24 fs. AIMSWISS almost exactly matches the time of first hapticity change encountered with the AIMS dynamics, although the populations of the first three excited states do not show satisfying agreement between AIMSWISS and AIMS (see fig. 17). Including nonadiabatic effects in the AIMSWISS simulation does thus improve the resulting observables, in comparison to the adiabatic AIMD simulation. This finding is reassuring, especially if one bears in mind that the populations obtained from AIMSWISS and AIMS are not in good agreement. From the examination of the geometry-based parameters for Ruwich one can thus learn that including nonadiabative effects, even if in a more approximation manner than in AIMS, does lead to an improvement, although the obtained populations are not guaranteed to agree.

7.2.3 Influence of nonadiabatic effects on the hapticity

To further compare the observables yielded from the AIMSWISS and the AIMD simulation after the time feasible with AIMS, the hapticities $\dot{\alpha}$ for both methods were compared and

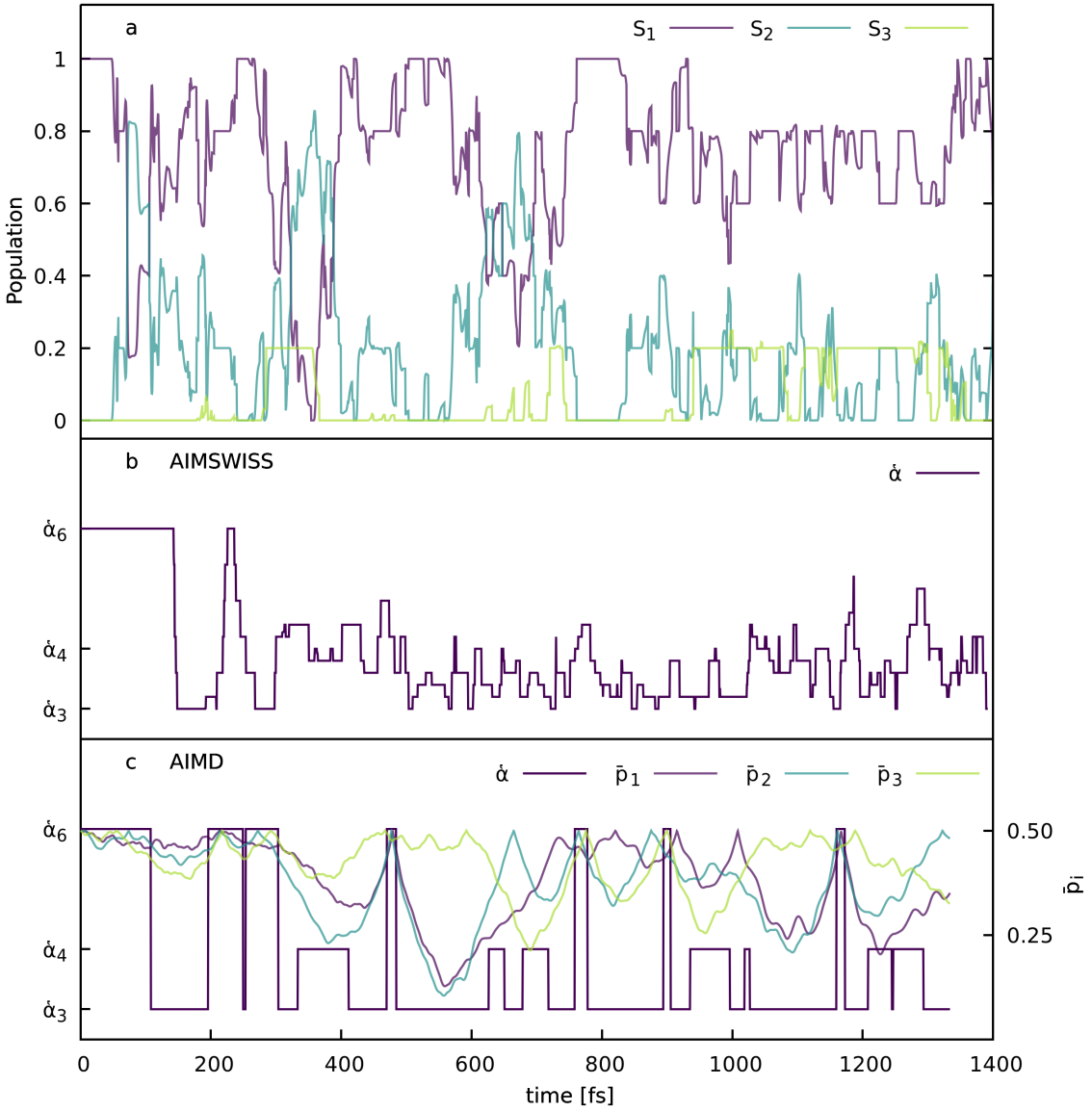

Figure 19: The populations and the hapticity parameter $\dot{\alpha}$ with its contributing projection values $\bar{p}_i$ are presented for the AIMSWISS and AIMD simulation. The top panel shows the population in S_1, S_2, and S_3 of the AIMSWISS dynamics. The central panel, labelled AIMSWISS, depicts the $\dot{\alpha}$ value for this simulation. In the bottom panel, labelled AIMD, the hapticity value and projection factors for AIMD are shown.

connected to the populations obtained with AIMSWISS.

Figure 19 shows the AIMSWISS population for the 1400 fs of simulated time (panel a) and the $\dot{\alpha}$ parameter for the AIMSWISS (panel b) and AIMD (panel c) simulations. From figure 19a, one can see that, although S_1 remains the most populated state for most of the simulated time, population transfers between S_1 and the other two states occur. From

around 320 fs to 390 fs, the S_2 population outweighs the S_1 population, and between 600 and 800 fs a strong interplay in S_1 and S_2 population can be observed. Over the prolonged time period from 950 fs to around 1300 fs the S_3 population increases to remain at a value of 0.2. A frequent population transfer, as observed in the AIMSWISS simulation, is in line with the expectation for Ruwich as this complex shows energetically close electronic eigenstates. Moving on to the hapticity values for the AIMSWISS simulation presented in figure 19b one observes that, after the initial 143 fs of $\dot{\alpha}_6$, the hapticity value never again remains constant for a prolonged period. For the AIMD simulation, however, periods of constant hapticity are also observed at later times in the simulation, mostly for $\dot{\alpha}_3$ and $\dot{\alpha}_4$ (see fig. 19c). Hapticity fluctuations occur more frequently in the AIMSWISS simulation than in the AIMD simulation. It can thus be stated that the nonadiabatic AIMSWISS simulation gives a far more flexible picture of the hapticity in Ruwich, as far more changes in the $\dot{\alpha}$ value are encountered during the simulation than in the AIMD simulation. Furthermore, it can be seen in figure 19b and c that $\dot{\alpha}_6$ configurations are encountered far less frequently in the AIMSWISS simulation than with AIMD. From this observation, one can gather that the Bz ring in the AIMSWISS simulation undergoes more distortions than in the AIMD simulation. The claw angle κ for the AIMSWISS and AIMD simulations were compared (see fig. 18c) to further investigate the character of these distortions. From this comparison, one can conclude that no remarkable drop in the claw angle as for the AIMD simulation can be observed in the AIMSWISS simulation. In the latter simulation, κ shows oscillations combined with an overall decrease until around 900 fs when the claw angle stays almost constant around 167°until the end of the simulation. As κ does not show a significant drop in the AIMSWISS simulation, the decrease in $\dot{\alpha}$ to values between 3 and 4 is more likely caused by slip distortions as depicted in the central inlet on the right-hand side of figure 19. Furthermore, the neglect of nonadiabatic effects in the AIMD simulation might be a reason for the overestimation of the opening of a new coordination side in Ruwich.

When connecting the populations in figure 19a to the $\dot{\alpha}$ values for AIMSWISS in figure 19b a trend of influence between the two properties can be identified. In the time interval between 900 and 1300 fs, 20 % of the population is in the S_3 state. The $\dot{\alpha}$ value in this time interval becomes higher than between 500 and 900 fs. Before 1200 fs and at around 1300 fs, $\dot{\alpha}$ shows values significantly above 4. Thus, a connection between an increase in S_3 population and higher hapticities can be assumed.

In summary, the comparison of geometry-based parameters for Ruwich from an adiabatic AIMD simulation to the nonadiabatic AIMS and AIMSWISS simulations showed that nonadiabatic effects have an impact on geometry changes in Ruwich. In an AIMD simulation, the evolution is always restricted to a single state which makes it impossible to account for situations where the population is evenly split between two or more excited states. Furthermore, in cases where the character of the adiabatic state changes, an AIMD trajectory launched on that state cannot transfer to a different state and must thus continue to evolve under this new character. As including population transfer between the singlet states is crucial, even several AIMD runs launched from different excited states would not be able to give an accurate picture of the Ruwich excited state dynamics. In the nonadiabatic simulations, the hapticity parameter $\dot{\alpha}$ showed more fluctuations between $\dot{\alpha}_3$ and $\dot{\alpha}_4$ while $\dot{\alpha}_6$ was shown to play a minor role. The AIMD simulation, however, suggested for the $\dot{\alpha}_6$ coordination to play a more prominent role. Including nonadiabatic effects also allowed us to visualize that the hapticity change occurs in a time interval rather than instant-

aneously. Using a nonadiabatic picture for the geometry change in Ruwich more smoothly includes any population transfer induced by changes in electronic character. Opposingly, in an adiabatic description, the population is forced to endure an instantaneous change in electronic character as a consequence of evolving on only one state. Therefore, the nonadiabatic AIMS and AIMSWISS simulations are more capable of depicting the hapticity change over time, which is likely to be accompanied by a change in electronic state character. We will have to perform more AIMSWISS runs and include different initial conditions to be able to accurately depict the gradual hapticity change and to draw further conclusions on underlying movement patterns. In this way, a more representative picture of electronically exciting the Ruwich population from a ground state minimum will be obtained. However, the performed analysis allowed us to further confirm the ability of the geometry parameters δ, κ, and $\dot{\alpha}$ to describe geometry changes in the Ruwich complex. With a more representative sampling of Ruwich structures the parameters will hopefully reveal the mechanisms underlying hapticity change in transition metal sandwich complexes such as Ruwich. With this more accurate depiction, it will be possible to distinguish between movement patterns, as the distortion-induced and the coordination side opening-induced hapticity change observed in the AIMD simulation.

8 Conclusion

In this work, we addressed the goals set in section 1.4 of finding an unambiguous hapticity definition based on atom distances that is applicable in static and time-dependent settings. To do so, we proposed a more rigorous definition for the concept of hapticity and tested it on the Ruwich complex in time-independent and time-dependent quantum mechanical calculations including singlet excited states. The versatile hapticity definition is contained in the parameter $\mathring{\alpha}$ and based on a straight-forward formula (see eq. (56)). When decomposed into its contributing projection values $\bar{p}_i$, the $\mathring{\alpha}$ parameter can also give side-specific information for the Ruwich complex, which can be of interest in applications targeting non-symmetric complexes. We successfully applied this definition in static calculations that included linear interpolation scans and time-dependent settings that consisted of adiabatic and nonadiabatic simulations. By combining the information from $\mathring{\alpha}$ and the distance and angle-based parameters δ and κ, interesting patterns on the movement underlying hapticity change in Ruwich were revealed. These patterns consist of a hapticity lowering caused by a slip distortion of Bz and due to a significant change of the claw angle κ. The $\mathring{\alpha}$ parameter, that was initially established for the Bz ligand, can be extended to other cyclic ligands of different geometry by determining a basis of bisection vectors suitable for the ligand of interest. In this way, our hapticity definition can easily be transferred to a broader range of transition metal complexes with cyclic π ligands.

In future work on Ruwich, we will improve the statistical convergence of the AIMSWISS simulations by performing more runs and including a more representative set of initial conditions. Another interest will lie in analyzing how well justified the application of AIMSWISS on an organometallic system such as Ruwich is, which can be achieved by investigating the AIMSWISS specific decoherence times more closely.

On top of this more technical follow-up work, it will be interesting for us to further investigate the excited state potential landscape of Ruwich by examining the influence of the so far not-considered triplet states. From an analysis of the triplet states in Ruwich, we will be able to gather to what extent excited states with different multiplicities are coupled to each other. Furthermore, it will be of interest to us to clarify how the electronic character of the singlet excited states is altered for different configurations of Ruwich. This insight will give additional refinement on the picture of the PESs relevant for hapticity changes.

To diverge into an even more open field of possibilities, it will be of interest for us to view Ruwich in a more general light by not only focussing on the Bz ligand. As a first step in this direction, we will focus on changes in the geometry and coordination mode of the Cp ligand. Furthermore, investigating hapticity changes in other ligands, such as substituted Bz rings or heterocycles, will allow us to examine an entire family of Ruwiches. In this way, the influence of asymmetry and different steric and electronic environments on light-induced hapticity changes and the underlying mechanism can be studied.

To summarize the work carried out in this thesis, we gave a rigorous definition of hapticity easily transferable to different cyclic ligands. This definition can be applied to different scenarios of quantum chemical calculations and is linked to experimental observables as it only relies on atomic distances. With this definition and further work on the carried-out dynamics simulations, it will be possible to examine the mechanisms underlying light-induced hapticity changes in Ruwich, and potentially verify them with the help of an experimental study using for example time-resolved X-ray or electron diffraction techniques.

9 Acknowledgements

"'Are you sitting comfortably? Then we'll begin'"[78]

How does one write acknowledgements? Certainly, when you are all set with the right music, mood, and have made enough time it should come to you like nothing. Effortlessly, like the warm and bright spring sun penetrating your hopefully double-glazed window. And well if it doesn't, you just start by jotting down on the paper whatever thoughts float through your mind. And slowly, if you show enough patience, it shall come to you just like the first drops of refreshing spring rain, that start falling slowly, but with unparalleled certainty.

Yes, seasonal metaphors, and probably more of these overused literary images to come - but bear with me, at some point in this writing the over-complicated structures filled with subjectivity had to leave my head.

I would like to thank Prof. Leticia Gonzalez as she was the first person who gave me the impression that I am actually capable of doing things - in an academic setting that is. Also, without her, it would not have been possible for me to carry out the work that led to this Master's thesis. Then, I would like to express my gratitude to Prof. Basile Curchod who supervised me during my Master's project. I think it is fair to say that I might have quit at certain points if it had not been for his understanding and acceptance of my struggles. Furthermore, in his style of supervising, he never failed to direct me while still giving me the feeling that I can change directions if I wish to do so, and explaining to me all the different components that should be taken into account when making a decision. He also never failed to show honest enthusiasm for the results I presented to him, and managed to suffer through my lengthy, complicated, and non-linear sentences.

Going on, I would like to thank Moritz Heindl for the never-ending support he has provided me with. He was the very first person to spark my interest in the field of theoretical chemistry and always answered the questions I had as an undergraduate with great enthusiasm and endurance. During my Master's, he always helped me deal with the bureaucracy one is confronted with when studying at the University of Vienna (Here, I would like to give the SSC an honorable mention). And further than that, he has always been the person I could turn to when I felt like my life had been shattered in pieces, for he would recollect the pieces to try and make something new, more bearable, and sometimes even beautiful out of them. Next, I want to express my gratitude to Ludwig Schwiedrzik who supervised me during my Bachelor's thesis and still makes a regular appearance when I try to share some life advice. Among the most important things, I learned from him that, if I am unhappy with something, feel like I am not treated correctly, or am confronted with injustice, I am allowed to and also should express that opinion. If it had not been for him, I would have dealt differently with certain events in my life, and would not have managed to achieve an outcome that is compatible with my values. In addition to that, he exemplified to me that making mistakes is a normal and also necessary part of living - this life rule that everyone talks about but only very few people ever live up to.

The next person I want to express my deepest gratitude to is Johannes Karka. Studying for the theoretical chemistry exam with me until 5 a.m. has brought him into his first police check, and also other than that, we shared many extraordinary moments that really made us stick together. He has always been a person to constantly express their belief in me, and grounding me back in the real world whenever it was necessary. It feels very good

to have you in my life and to know that you are a person I can always turn to no matter what problem I have! I hope you finish soon such that we can finally get that tattoo of equation (1) in section 2.5 in the most dust-collectingly unexciting font that there is. Among Johannes Karka, there are many other people in Vienna whom I want to thank deeply for their support and the never-ending fun they have provided me with. First of all, there is the legendary β-group, whose beer brewing sessions and other fun activities Johnny introduced me to, and who were always up for spontaneously helping me whenever I needed them. Then, there are Isabelle Eder, Katharina Himmler, Robin Pfister, and Rebecca Schmidt whom I had the pleasure of hosting the DCCC Erstitut with, and whom I am always glad to meet with again, whenever I return to Vienna.

Moving over to Bristol, geographically and figuratively, I want to thank all the amazing people of the CCC for welcoming me and integrating me into their group in such a short amount of time. It has made my decision to leave Vienna and move to Bristol so much easier to know that I am surrounded by people who value me for who I am and not for how much work I get done. I would like to thank Dasha Shchepanovska and Alex Binnie for providing me with the most wholesome British experience of eating pie as well as inviting me to a spontaneous Thursday night session of serious karaoke. Furthermore, I would like to thank Abbie Lear for being a very supportive person having nice conversations with me, and for inviting me to her music concerts. I also want to express my gratitude towards the members of Basile's research group, Daniel Hollas, Jiří Janoš, Harry Stroud, and Jack Taylor who were always happy to help me, and really took their time to answer my questions even if it happened to be on a Saturday afternoon. Thanks to all of you, I am very glad to now feel at home at a place where Tabasco is readily available at every pub, despite them still having to improve on their milk offerings.

Finally, to bring this armada of complicated sentences to a stopping point, I would like to express my deepest gratitude to Yorick Lassmann. Alongside always believing in my abilities, my strength, and endurance, he gave me the feeling that I am, regardless of how weird I might be at certain times, an actual human being. He provided me with a level of support unparalleled by anything I could have imagined up until that point and threw himself into the breach of suffering through my follies and terrible moods that otherwise would have had to remain unexpressed. He is among the most caring and honest people that I have met throughout my life and I am truly grateful for having shared the moments with him that now fill me with the deepest sense of joy when reviving the memory.

And now very finally, let me finish by saying that during my Master's studies, I encountered moments where I thought nothing could bring me to continue doing this, and if it had not been for the people I mentioned above this might well have been the reality. I therefore thank each and every one of you for giving me enough evidence such that I can finally start to base the belief in myself on a power coming from inside of me. And to the reader, who did actually bear with me through this journey of sometimes clumsy English grammar that constructed a literary road very bumpy to follow, I am sorry for being so melodramatic and for including such unoriginal metaphors. But, as I once thought when first considering doing a PhD, academia might, at least in my case, be a relatively easy access to becoming a published writer. And, because I soon discovered that this comes with the downside of having to follow the guidelines of scientific writing, you had to witness this take on producing a part that is more, let's say, original.

References

[1] F. A. Cotton, "A half-century of nonclassical organometallic chemistry: A personal perspective," *Inorganic chemistry*, vol. 41, no. 4, pp. 643–658, 2002.

[2] S. Goodman, "The return of the ring." Gossip Girl, season 5, episode 24, dir. by J. Miller Tobin, prod. by S. Savage, J. Schwartz, publ. by CBS Television Studios, Fake Empire, 2012.

[3] H.-U. Blaser, A. Indolese, and A. Schnyder, "Applied homogeneous catalysis by organometallic complexes," *Current Science*, pp. 1336–1344, 2000.

[4] D. A. Valyaev, G. Lavigne, and N. Lugan, "Manganese organometallic compounds in homogeneous catalysis: Past, present, and prospects," *Coordination Chemistry Reviews*, vol. 308, pp. 191–235, 2016.

[5] S. Kumar, B. Z. Dholakiya, and R. Jangir, "Role of organometallic complexes in olefin polymerization: a review report," *Journal of Organometallic Chemistry*, vol. 953, p. 122066, 2021.

[6] M. N. Hopkinson, C. Richter, M. Schedler, and F. Glorius, "An overview of N-heterocyclic carbenes," *Nature*, vol. 510, pp. 485–496, 2014.

[7] C. Chen, F.-S. Liu, and M. Szostak, "BIAN-NHC ligands in transition-metal-catalysis: A perfect union of sterically encumbered, electronically tunable N-heterocyclic carbenes?," *Chemistry – A European Journal*, vol. 27, no. 14, pp. 4478–4499, 2021.

[8] E. Peris and R. H. Crabtree, "Key factors in pincer ligand design," *Chem. Soc. Rev.*, vol. 47, pp. 1959–1968, 2018.

[9] P. Kl'an and J. Wirz, *Chemistry of Excited Molecules*, ch. 6, pp. 227–453. John Wiley Sons, Ltd, 2009.

[10] P. E. Eaton, "Photochemical reactions of simple alicyclic enones," *Accounts of Chemical Research*, vol. 1, no. 2, pp. 50–57, 1968.

[11] L. Buzzetti, G. E. Crisenza, and P. Melchiorre, "Mechanistic studies in photocatalysis," *Angewandte Chemie International Edition*, vol. 58, no. 12, pp. 3730–3747, 2019.

[12] B. Maity, S. Dutta, and L. Cavallo, "The mechanism of visible light-induced C–C cross-coupling by C sp3–H bond activation," *Chemical Society Reviews*, 2023.

[13] D. S. Lee, V. K. Soni, and E. J. Cho, "N–O bond activation by energy transfer photocatalysis," *Accounts of Chemical Research*, vol. 55, no. 17, pp. 2526–2541, 2022.

[14] C. Sousa, M. Alías, A. Domingo, and C. deGraaf, "Deactivation of excited states in transition-metal complexes: Insight from computational chemistry," *Chemistry – A European Journal*, vol. 25, no. 5, pp. 1152–1164, 2019.

[15] G. O. Spessard and G. L. Miessler, *Organometallic chemistry*. Prentice-Hall, 1997.

[16] F. A. Cotton, "Proposed nomenclature for olefin-metal and other organometallic complexes," *Journal of the American Chemical Society*, vol. 90, no. 22, pp. 6230–6232, 1968.

[17] N. V. Shvydkiy and D. S. Perekalin, "Reactions of arene replacement in transition metal complexes," *Coordination Chemistry Reviews*, vol. 411, p. 213238, 2020.

[18] F. A. Cotton, "Fluxional organometallic molecules," *Accounts of Chemical Research*, vol. 1, no. 9, pp. 257–265, 1968.

[19] M. A. Bennett, R. Bramley, and R. Watt, "Variable-temperature proton resonance spectra of trihaptocycloheptatrienylmetal complexes," *Journal of the American Chemical Society*, vol. 91, no. 11, pp. 3089–3091, 1969.

[20] D. Mingos, "19 - bonding of unsaturated organic molecules to transition metals," in *Comprehensive Organometallic Chemistry* (G. Wilkinson, F. A. Stone, and E. W. Abel, eds.), pp. 1–88, Oxford: Pergamon, 1982.

[21] I. D. Gridnev, "Sigmatropic and haptotropic rearrangements in organometallic chemistry," *Coordination Chemistry Reviews*, vol. 252, no. 15-17, pp. 1798–1818, 2008.

[22] B. E. Mann, "Fluxionality of polyene and polyenyl metal complexes," *Chemical Society Reviews*, vol. 15, no. 2, pp. 167–187, 1986.

[23] S. Niibayashi, K. Matsubara, M.-a. Haga, and H. Nagashima, "Thermally reversible photochemical haptotropic rearrangement of diiron carbonyl complexes bearing a bridging acenaphthylene or aceanthrylene ligand," *Organometallics*, vol. 23, no. 4, pp. 635–646, 2004.

[24] F. A. Cotton, G. Wilkinson, C. A. Murillo, and M. Bochmann, *Advanced inorganic chemistry*. John Wiley & Sons, 1999.

[25] C. Campbell and M. Green, "Evidence for a 1, 2-shift mechanism for the rearrangement of σ-cyclopentadienyl compounds of iron, ruthenium, and copper," *Journal of the Chemical Society A: Inorganic, Physical, Theoretical*, pp. 1318–1323, 1970.

[26] K. R. Mann, A. M. Blough, J. L. Schrenk, R. S. Koefod, D. A. Freedman, and J. R. Matachek, "Mechanistic aspects of the photochemistry of [CpM(6-arene)]+ complexes of Fe, Ru and Os," *Pure and Applied Chemistry*, vol. 67, no. 1, pp. 95–101, 1995.

[27] L. J. Williams, Y. Bhonoah, L. A. Wilkinson, and J. W. Walton, "As nice as π: aromatic reactions activated by π-coordination to transition metals," *Chemistry–A European Journal*, vol. 27, no. 11, pp. 3650–3660, 2021.

[28] J. W. Walton and L. A. Wilkinson, "π-coordinated arene metal complexes and catalysis," *Organometallic Chemistry*, vol. 42, pp. 125–171, 2018.

[29] K. H. Dötz, J. Stendel Jr, S. Müller, M. Nieger, S. Ketrat, and M. Dolg, "Haptotropic metal migration in densely substituted hydroquinoid phenanthrene $Cr(CO)_3$ complexes," *Organometallics*, vol. 24, no. 13, pp. 3219–3228, 2005.

[30] S. Ketrat, S. Müller, and M. Dolg, "A quantum chemical study of the haptotropic rearrangements of $Cr(CO)_3$ on naphthalene and phenanthrene systems," *The Journal of Physical Chemistry A*, vol. 111, no. 27, pp. 6094–6102, 2007.

[31] I. D. Gridnev, N. U. Zhanpeisov, and M. K. C. Del Rosario, "Experimental and theoretical study of the metallotropic migrations in cyclooctatetraeneosmiumtricarbonyl," *The Journal of Physical Chemistry B*, vol. 109, no. 25, pp. 12498–12502, 2005.

[32] C. A. Bradley, I. Keresztes, E. Lobkovsky, V. G. Young, and P. J. Chirik, "Zirconium sandwich complexes with η^9 indenyl ligands: well-defined precursors for zirconocene-mediated coupling reactions," *Journal of the American Chemical Society*, vol. 126, no. 51, pp. 16937–16950, 2004.

[33] L. F. Veiros, "Substituent effects on haptotropic rearrangements of bis (indenyl) zirconium sandwich complexes," *Organometallics*, vol. 25, no. 9, pp. 2266–2273, 2006.

[34] Y. F. Oprunenko and I. Gloriozov, "A density functional study of intra-and interring haptotropic η^2, η^2 rearrangements in rhodium, ruthenium, and osmium naphthalene complexes," *Russian Journal of Physical Chemistry A*, vol. 86, pp. 979–986, 2012.

[35] C. J. Czerwinski, E. O. Fetisov, I. P. Gloriozov, and Y. F. Oprunenko, "DFT study of intramolecular interring η^6, η^6-haptotropic rearrangements in tricarbonylchromium complexes of 2-aminobiphenyl and 4-aminobiphenyl," *Dalton Transactions*, vol. 42, no. 29, pp. 10487–10494, 2013.

[36] I. P. Gloriozov, M. S. Nechaev, K. V. Zaitsev, Y. F. Oprunenko, F. Gam, and J.-Y. Saillard, "DFT study of inter-ring haptotropic rearrangement in $[CpRu]^+$ complexes of polycyclic aromatic ligands," *Journal of Organometallic Chemistry*, vol. 889, pp. 9–14, 2019.

[37] W. Koch and M. C. Holthausen, *A chemist's guide to density functional theory*. John Wiley & Sons, 2001.

[38] P. Hohenberg and W. Kohn, "Inhomogeneous electron gas," *Phys. Rev.*, vol. 136, pp. B864–B871, Nov 1964.

[39] W. Kohn and L. J. Sham, "Self-consistent equations including exchange and correlation effects," *Phys. Rev.*, vol. 140, pp. A1133–A1138, Nov 1965.

[40] E. Runge and E. K. Gross, "Density-functional theory for time-dependent systems," *Physical review letters*, vol. 52, no. 12, p. 997, 1984.

[41] A. Dreuw and M. Head-Gordon, "Single-reference ab initio methods for the calculation of excited states of large molecules," *Chemical reviews*, vol. 105, no. 11, pp. 4009–4037, 2005.

[42] R. Van Leeuwen, "Mapping from densities to potentials in time-dependent density-functional theory," *Physical review letters*, vol. 82, no. 19, p. 3863, 1999.

[43] C. A. Ullrich and Z.-h. Yang, "A brief compendium of time-dependent density functional theory," *Brazilian Journal of Physics*, vol. 44, pp. 154–188, 2014.

[44] M. E. Casida, "Time-dependent density functional response theory for molecules," in *Recent Advances In Density Functional Methods: (Part I)*, pp. 155–192, World Scientific, 1995.

[45] S. Hirata and M. Head-Gordon, "Time-dependent density functional theory within the Tamm–Dancoff approximation," *Chemical Physics Letters*, vol. 314, no. 3-4, pp. 291–299, 1999.

[46] X. Zhu, K. C. Thompson, and T. J. Martínez, "Geodesic interpolation for reaction pathways," *The Journal of Chemical Physics*, vol. 150, 04 2019.

[47] A. Tachibana and K. Fukui, "Differential geometry of chemically reacting systems," *Theoretica chimica acta*, vol. 49, pp. 321–347, 1978.

[48] A. Tachibana and K. Fukui, "Intrinsic field theory of chemical reactions," *Theoretica chimica acta*, vol. 51, pp. 275–296, 1979.

[49] M. Born and K. Huang, "Dynamic theory of crystal lattice, clarendon," 1954.

[50] M. Born and R. Oppenheimer, "Zur quantentheorie der molekeln," *Annalen der Physik*, vol. 84, 1927.

[51] E. J. Heller, "Frozen gaussians: A very simple semiclassical approximation," *The Journal of Chemical Physics*, vol. 75, no. 6, pp. 2923–2931, 1981.

[52] B. Lasorne, M. J. Bearpark, M. A. Robb, and G. A. Worth, "Direct quantum dynamics using variational multi-configuration Gaussian wavepackets," *Chemical physics letters*, vol. 432, no. 4-6, pp. 604–609, 2006.

[53] M. Ben-Nun and T. J. Martınez, "Nonadiabatic molecular dynamics: Validation of the multiple spawning method for a multidimensional problem," *The Journal of chemical physics*, vol. 108, no. 17, pp. 7244–7257, 1998.

[54] T. J. Martinez, M. Ben-Nun, and R. D. Levine, "Multi-electronic-state molecular dynamics: A wave function approach with applications," *The Journal of Physical Chemistry*, vol. 100, no. 19, pp. 7884–7895, 1996.

[55] M. Ben-Nun, J. Quenneville, and T. J. Martínez, "Ab initio multiple spawning: Photochemistry from first principles quantum molecular dynamics," *The Journal of Physical Chemistry A*, vol. 104, no. 22, pp. 5161–5175, 2000.

[56] B. F. Curchod, W. J. Glover, and T. J. Martínez, "SSAIMS—stochastic-selection ab initio multiple spawning for efficient nonadiabatic molecular dynamics," *The Journal of Physical Chemistry A*, vol. 124, no. 30, pp. 6133–6143, 2020.

[57] Y. Lassmann and B. F. Curchod, "AIMSWISS—ab initio multiple spawning with informed stochastic selections," *The Journal of Chemical Physics*, vol. 154, no. 21, 2021.

[58] J.-D. Chai and M. Head-Gordon, "Long-range corrected hybrid density functionals with damped atom–atom dispersion corrections," *Physical Chemistry Chemical Physics*, vol. 10, no. 44, pp. 6615–6620, 2008.

[59] S. Grimme, J. Antony, S. Ehrlich, and H. Krieg, "A consistent and accurate ab initio parametrization of density functional dispersion correction (DFT-D) for the 94 elements H-Pu," *The Journal of chemical physics*, vol. 132, no. 15, 2010.

[60] T. H. Dunning Jr, "Gaussian basis sets for use in correlated molecular calculations. I. the atoms boron through neon and hydrogen," *The Journal of chemical physics*, vol. 90, no. 2, pp. 1007–1023, 1989.

[61] P. J. Hay and W. R. Wadt, "Ab initio effective core potentials for molecular calculations. potentials for the transition metal atoms Sc to Hg," *The Journal of chemical physics*, vol. 82, no. 1, pp. 270–283, 1985.

[62] C. Song, L.-P. Wang, and T. J. Martínez, "Automated code engine for graphical processing units: Application to the effective core potential integrals and gradients," *Journal of chemical theory and computation*, vol. 12, no. 1, pp. 92–106, 2016.

[63] I. Ufimtsev and T. Martínez, "Quantum chemistry on graphical processing units. III. analytical energy gradients and first principles molecular dynamics," *J. Chem. Theory Comput*, vol. 5, p. 2619, 2009.

[64] A. V. Titov, I. S. Ufimtsev, N. Luehr, and T. J. Martinez, "Generating efficient quantum chemistry codes for novel architectures," *Journal of chemical theory and computation*, vol. 9, no. 1, pp. 213–221, 2013.

[65] C. M. Isborn, N. Luehr, I. S. Ufimtsev, and T. J. Martínez, "Excited-state electronic structure with configuration interaction singles and Tamm–Dancoff time-dependent density functional theory on graphical processing units," *Journal of Chemical Theory and Computation*, vol. 7, no. 6, pp. 1814–1823, 2011.

[66] W. Humphrey, A. Dalke, and K. Schulten, "VMD: visual molecular dynamics," *Journal of molecular graphics*, vol. 14, no. 1, pp. 33–38, 1996.

[67] B. F. Curchod, A. Sisto, and T. J. Martínez, "Ab initio multiple spawning photochemical dynamics of DMABN using GPUs," *The Journal of Physical Chemistry A*, vol. 121, no. 1, pp. 265–276, 2017.

[68] M. P. Esch, Y. Shu, and B. G. Levine, "A conical intersection perspective on the low nonradiative recombination rate in lead halide perovskites," *The Journal of Physical Chemistry A*, vol. 123, no. 13, pp. 2661–2673, 2019.

[69] W. Kabsch, "A solution for the best rotation to relate two sets of vectors," *Acta Crystallographica Section A: Crystal Physics, Diffraction, Theoretical and General Crystallography*, vol. 32, no. 5, pp. 922–923, 1976.

[70] F. Grepioni, G. Cojazzi, D. Braga, E. Marseglia, L. Scaccianoce, and B. F. Johnson, "Crystal architecture of the cocrystalline salt [Ru(η5−C5H5) (η6−trans−PhCH=CHPh)][PF6]·0.5trans−*P*hCH=CHPh and the reversible order–disorder phase transition in [Ru(η5−C5H5) (η6−C6H6)][PF6]," *Journal of the Chemical Society, Dalton Transactions*, no. 4, pp. 553–558, 1999.

[71] A. Prlj, E. Marsili, L. Hutton, D. Hollas, D. Shchepanovska, D. R. Glowacki, P. Slavícek, and B. F. Curchod, "Calculating photoabsorption cross-sections for atmospheric volatile organic compounds," *ACS Earth and Space Chemistry*, vol. 6, no. 1, pp. 207–217, 2021.

[72] T. Gill and K. Mann, "Photochemical properties of the cyclopentadienyl(6-benzene)ruthenium(II) cation. the synthesis and reactions of a synthetically useful intermediate: The cyclopentadienyltris(acetonitrile)ruthenium(ii) cation," *Organometallics*, vol. 1, pp. 485–488, Jan. 1982.

[73] J. P. Perdew, K. Burke, and M. Ernzerhof, "Generalized gradient approximation made simple," *Physical review letters*, vol. 77, no. 18, p. 3865, 1996.

[74] J. Perdew, K. Burke, and M. Ernzerhof, "Errata: generalized gradient approximation made simple," *Phys. Rev. Lett*, vol. 78, p. 1396, 1997.

[75] R. A. Kendall, T. H. Dunning Jr, and R. J. Harrison, "Electron affinities of the first-row atoms revisited. systematic basis sets and wave functions," *The Journal of chemical physics*, vol. 96, no. 9, pp. 6796–6806, 1992.

[76] W. J. Bowyer, J. W. Merkert, W. E. Geiger, and A. L. Rheingold, "Structural consequences of electron-transfer reactions. part 18. redox-induced hapticity changes: effect of substituents on arene bending in a series of rhodium complexes," *Organometallics*, vol. 8, no. 1, pp. 191–198, 1989.

[77] Y. Lassmann, D. Hollas, and B. F. Curchod, "Extending the applicability of the multiple-spawning framework for nonadiabatic molecular dynamics," *The Journal of Physical Chemistry Letters*, vol. 13, no. 51, pp. 12011–12018, 2022.

[78] G. Unger-Hamilton, G. Sainsbury, J. Newman, and T. Green, "Hand-made." from the album "An Awesome Wave" by artist alt-J, publ. by Infectious Music Ltd., a BMG Company, 2012.